

Imperial College London
Department of Mechanical Engineering

Nanoparticle-modified epoxies - Effect of test rate

Wing Lam (Jasmine) Tsang

January 17, 2017

Supervised by Dr Ambrose Taylor

Submitted in fulfilment of the requirements for the degree of
Doctor of Philosophy in Mechanical Engineering of Imperial College London
and the Diploma of Imperial College London

Chapter 1

Declaration

Abstract

This study compares the effect on the fracture energy of an epoxy polymer from the addition of different weight % of nanoparticles, at both quasi-static and high test rates. Silica and core-shell rubber (CSR) particles, and the hybrid of both (from 0.5 weight % to the maximum concentration of 25.4 weight %) are used. Initial work concentrated on quasi-static test rates, and now the fracture energy at high test rates has been measured. Tapered double cantilever beam (TDCB) and single-edge notch bending (SENB) specimens were used for measurement of the fracture energy, G_c . As there was interfacial failure found with some TDCB specimens, the fracture energy found from the SENB specimens would provide additional information to clarify the results found from the TDCB tests. Higher fracture energy values were found from the SENB specimens. The lower values from the TDCBs could be due to the interfacial failure. An increase in fracture energy was found in the CSR and hybrid specimens, but clustering of particles caused a reduction in the mechanical properties when the concentration of particles was high. There were higher fracture energy values when the test rate was higher. Therefore, higher fracture energies are expected when the test rate increases further. The fracture energies measured with TDCB specimens will also be compared with simulation results using the finite element analysis software Abaqus. The toughening mechanisms involved will be confirmed by fracture surface images obtained from field emission gun scanning electron microscopy (FEG-SEM).

Contents

1 Declaration	i
Abstract	ii
2 Introduction	1
2.1 Introduction	1
3 Literature review	3
3.1 Introduction	3
3.1.1 Rubber-toughened epoxy	4
3.1.2 Silica-toughened epoxy	5
3.1.3 Other materials used	6
3.1.4 Fracture mechanics	8
3.1.5 Fracture toughness	8
3.1.6 Tapered double cantilever beam (TDCB)	10
3.1.7 Types of crack growth	12
3.1.8 Single-edge notch bending (SENB)	12
3.2 Toughening mechanisms	15
3.2.1 Introduction	15
3.2.2 Shear bands and shear yielding	15
3.2.3 Crack pinning	15
3.2.4 Crack deflection	16
3.2.5 Cavitation	17
3.2.6 Debonding	17
3.2.7 Rubber bridging	17
3.2.8 Plastic void growth	19
3.2.9 Modelling toughening mechanisms	19
3.2.10 High rate testing	20
3.2.11 Uncertainties	20
3.2.12 Geometry factor	22
3.2.13 Toughening mechanisms	22

3.3	Conclusions	22
4	Experimental work	23
4.1	Introduction	23
4.2	Materials and methods	23
4.2.1	Materials	23
4.2.2	TDCB specimen preparation	24
4.2.3	Differential scanning calorimetry (DSC) tests	25
4.2.4	Quasi-static rate tests	26
4.2.5	Initial loading and re-loading	27
4.2.6	Initiation and propagation values	27
4.2.7	Determination of G_c in TDCB	28
4.2.8	Field emission gun scanning electron microscopy (FEG-SEM) . .	29
4.2.9	Scanning electron microscopy	29
4.2.10	Fracture energies	29
4.2.11	Fracture surfaces	33
4.3	High rate testing	34
4.3.1	Introduction	34
4.3.2	TDCB high test rate set up	35
4.4	High rate data reduction strategy	37
4.4.1	Fracture types	37
4.4.2	Data analysis	37
4.4.3	High rate TDCB results	42
4.5	Tensile testing	44
4.5.1	Introduction	44
4.5.2	Results	44
4.6	Single-edge notch bending (SENB) tests	46
4.6.1	Introduction	46
4.6.2	Testing	48
4.6.3	Results	51
4.6.4	Quasi-static fracture energy (from TDCB and SENB)	58
4.7	Analytical models	60
4.7.1	Halpin-Tsai model	60
4.7.2	Huang & Kinloch fracture model	61
4.7.3	Shear band yielding	62
4.7.4	Plastic zone size consideration	63

4.7.5	Predicted results	64
4.8	Scanning electron microscopy	74
4.8.1	Introduction	74
4.8.2	SEM results	74
4.9	Finite element analysis (FEA)	83
4.9.1	Finite element analysis introduction	83
4.9.2	Finite element analysis results	85
4.9.3	Progress	87
4.10	W210 and PES materials	88
4.10.1	Materials information	88
4.10.2	Tensile results of PES and W210	89
4.11	Low temperature SENB	90
4.11.1	Low temperature SENB results (Silica, CSR and Hybrid of both)	92
4.11.2	Fracture energy predictions	102
4.11.3	Analytical model modulus predictions	107
4.12	Conclusions	112
	References	112
A	Appendices	118
A.1	Input file-TDCB model	118

List of Tables

4.1	Fracture energy versus crack length for the control epoxy from TDCB specimen	30
4.2	Summary of fracture energies calculated using the CBT method from TDCB specimens, mean standard deviation	31
4.3	Summary of fracture energies of CSR modified epoxy calculated using the CBT method from TDCB specimens, mean standard deviation.	33
4.4	Tensile test results of nanoparticle-modified epoxy	46
4.5	Particle content used in SENB specimens	47
4.6	Fracture energy of modified epoxy under quasi static test rate	53
4.7	Fracture energy of silica-modified epoxy at different rate	54
4.8	Fracture energy of CSR-modified epoxy at different rate	56
4.9	Fracture energy of Hybrid-modified epoxy at different rate	57
4.10	Modulus used for CSR and hybrid modified epoxy	61
4.11	Values of parameters used for toughening predictions.	64
4.12	Predicted modulus from Halpin-Tsai model of silica-modified epoxy	65
4.13	Predicted modulus from Halpin-Tsai model of CSR-modified epoxy	66
4.14	Predicted modulus from Halpin-Tsai model of Hybrid-modified epoxy	67
4.15	Table showing fracture energy predictions from assuming 100% void growth	68
4.16	Table showing fracture energy predictions from assuming 14.3% void growth	69
4.17	Table showing fracture energy predictions from assuming there was only shear	69
4.18	Table showing fracture energy predictions of silica-modified epoxy	70
4.19	Table showing fracture energy predictions of CSR-modified epoxy	71
4.20	Fracture energy predictions of hybrid-modified epoxy	73
4.21	Properties of aluminium alloy (EN AW 2014-A) [69] and epoxy [38] for the FE model	84
4.22	Tensile modulus results of W210 ceramics modified epoxy	90
4.23	Fracture energy of Silica modified epoxy under low temperature	92

4.24	Fracture energy of CSR modified epoxy under low temperature	94
4.25	Fracture energy of Hybrid modified epoxy under low temperature	96
4.26	Fracture energy of PES modified epoxy under low temperature	98
4.27	Fracture energy of Hybrid PES modified epoxy under low temperature .	100
4.28	Table showing fracture energy predictions of W210 and PES from assuming 100% void growth	102
4.29	Table showing fracture energy predictions from assuming 14.3% void growth	103
4.30	Table showing fracture energy predictions from assuming there was only shear	103
4.31	Table showing fracture energy predictions of ceramics W210-modified epoxy	104
4.32	Table showing fracture energy predictions of Hybrid ceramics W210-modified epoxy	105
4.33	Table showing fracture energy predictions of PES-modified epoxy	106
4.34	Table showing fracture energy predictions of Hybrid PES-modified epoxy	107
4.35	Predicted modulus of W210-modified epoxy	108
4.36	Predicted modulus of W210 hybrid-modified epoxy	109
4.37	Predicted modulus of PES-modified epoxy	110
4.38	Predicted modulus of PES hybrid-modified epoxy	112

List of Figures

3.1	Co-continuous phase [11]	7
3.2	Different phases of PES: a) Particulate b) Transition between particulate and co-continuous c) Co-continuous and d)Phase-inverted microstructure[28]	7
3.3	The different modes of loading [27]	9
3.4	Plastic zone model	10
3.5	Failure modes diagram a) cohesive, and b) interfacial failure [16]	11
3.6	Graphic representation of different fracture types under different testing conditions [16]	13
3.7	Single edge notch bending (SENB) specimen [39]	13
3.8	Single edge notch bending (SENB) test, loaded in three point bending [40]	14
3.9	The process of crack pinning [29]	16
3.10	Crack deflection by a particle, after [32]	16
3.11	SEM image of cavitation of rubber particles [5]	17
3.12	SEM image of debonding of glass particles [46]	18
3.13	Rubber bridging model [47]	18
3.14	Figure showing plastic void growth of epoxy (tested at 40°C) [48]	19
3.15	Flow chart for data reduction strategy of TDCB test [52]	21
4.1	TDCB bonding jig	25
4.2	TDCB specimens	25
4.3	Heating and cooling cycle in DSC [29]	26
4.4	TDCB test set up	27
4.5	Fracture energy versus crack length for the control epoxy from TDCB specimen	30
4.6	Fracture energy against percentage of silica from TDCB specimens (CBT) and model predictions from Hsieh et al. [46] [51]	32
4.7	Fracture energy against percentage of particles for CSR-modified epoxy from TDCB specimens	33

4.8	Fracture surfaces of TDCB specimens (crack propagation from right to left)	34
4.9	TDCB mode I high rate test setup [38]	36
4.10	TDCB mode I high rate test setup [38]	36
4.11	Example of high rate TDCB image. Crack propagation was from left to right	37
4.12	Distance between centres of pins against time graph for TDCB specimen	38
4.13	Distance between centres of pins against time graph for TDCB specimen	39
4.14	Average fracture energy figure when rate is 1ms^{-1}	42
4.15	Average fracture energy figure when rate is 2ms^{-1}	43
4.16	Average fracture energy figure when rate is 3ms^{-1}	43
4.17	Tensile test geometry (dimensions in millimetres) [59]	44
4.18	Tensile modulus results of nanoparticle-modified epoxy	45
4.19	SENB specimen geometry according to standard [39], where w is width, l is overall length, h is thickness and a is crack length.	48
4.20	SENB specimen geometry according to standard [39], where w is width, l is overall length, h is thickness and a is crack length.	49
4.21	Force fluctuations in fracture tests [63]	50
4.22	High rate SENB test setup	51
4.23	Fracture energy of modified epoxy under quasi static test rate	52
4.24	Fracture energy of silica-modified epoxy at different rate	54
4.25	Fracture energy of CSR-modified epoxy at different rate * Dynamic effects are significant and hence the data are unreliable	55
4.26	Fracture energy of Hybrid-modified epoxy at different rate * Dynamic effects are significant and hence the data are unreliable	57
4.27	Fracture energy of silica-modified epoxy (SENB, TDCB)	58
4.28	Fracture energy of quasi-static CSR (SENB, TDCB) and CSR-MX-156 .	59
4.29	Predicted modulus from Halpin-Tsai model of silica-modified epoxy .	65
4.30	Predicted modulus from Halpin-Tsai model of CSR-modified epoxy .	66
4.31	Predicted modulus from Halpin-Tsai model of hybrid-modified epoxy .	67
4.32	Fracture energy prediction of silica-modified epoxy	70
4.33	Fracture energy prediction of CSR-modified epoxy	72
4.34	Fracture energy prediction of hybrid-modified epoxy	74
4.35	CSR-modified epoxy specimen tested under quasi-static rate	75
4.36	CSR-modified epoxy specimen tested under quasi-static rate	75
4.37	Estimation of void diameters	76

4.38 Area with voids in CSR-modified epoxy SENB specimen	76
4.39 Area with voids in CSR-modified epoxy SENB specimen	77
4.40 Original CSR particles	77
4.41 Cut CSR particles	78
4.42 Example of damaged CSR particles	78
4.43 CSR 0.5% specimen	79
4.44 CSR 3% specimen	79
4.45 CSR 5% specimen	80
4.46 CSR 10% specimen	80
4.47 Deformed CSR particles for high % of CSR specimen	81
4.48 Deformed CSR particles for low % of CSR specimen	81
4.49 Small voids inside a particle	81
4.50 Example of CSR particle deformation at high magnification	82
4.51 CSR-modified epoxy specimen tested at room temperature	82
4.52 CSR-modified epoxy specimen tested at $40^{\circ}C$	83
4.53 CSR-modified epoxy specimen tested at $80^{\circ}C$	83
4.54 Forces in TDCB (modified from [69])	84
4.55 Traction-separation curve [69]	85
4.56 FEA predictions and experimental data of silica-modified epoxy	86
4.57 FEA predictions and experimental data of CSR-modified epoxy	87
4.58 Tensile modulus results of W210 ceramics modified epoxy	90
4.59 Low temperature SENB setup 1	91
4.60 Low temperature SENB setup 2	91
4.61 Fracture energy of Silica modified epoxy under low temperature	93
4.62 Fracture energy of CSR modified epoxy under low temperature	95
4.63 Fracture energy of Hybrid modified epoxy under low temperature	97
4.64 Fracture energy of PES modified epoxy under low temperature	99
4.65 Fracture energy of Hybrid PES modified epoxy under low temperature .	101
4.66 Figure showing fracture energy predictions of ceramics W210-modified epoxy	104
4.67 Figure showing fracture energy predictions of Hybrid ceramics W210- modified epoxy	105
4.68 Figure showing fracture energy predictions of PES-modified epoxy . . .	106
4.69 Figure showing fracture energy predictions of Hybrid PES-modified epoxy	107
4.70 Predicted modulus of W210-modified epoxy	108
4.71 Predicted modulus of W210 hybrid-modified epoxy	109

4.72 Predicted modulus of PES-modified epoxy	110
4.73 Predicted modulus of PES hybrid-modified epoxy	111

Chapter 2

Introduction

[2cm]

[ax]CSRCore Shell Rubber

2.1 Introduction

Epoxy is a thermoset polymer, which is highly crosslinked and brittle; hence there is a need to toughen epoxy for use in engineering applications. This project uses silica nanoparticles, core-shell rubber (CSR) particles and hybrids of both particle types, to investigate the toughening effect of epoxy with different weight % of nanoparticles at both quasi-static and high test rates. In addition, the work will investigate the synergistic toughening effects of combining silica nanoparticles with micron-sized rubber particles. There are two aspects in the effect of test rate study: the effect of different weight % of nanoparticles added, and the effect of different test rate (i.e. quasi-static and high rate). Silica particles will be added in at concentrations of 0.5, 1, 2, 3, 5, 10, 15 and 20 weight %, and at the maximum possible concentration (25.4 weight %). CSR particles will be added in at the same weight percentages, but up to a maximum of 10 weight %. In previous work[1-3], the effects of different weight % of silica have been investigated with relatively large weight percentages of nanoparticles (of 10 weight % and above, e.g. from Hsieh et al. [2] and Mohammed et al. [4]) but not with small weight percentages. It has been suggested that small percentages of silica nanoparticles are more effective at toughening epoxy than large weight percentages, but this has not yet been investigated. Hence this study will provide more information about the effect of small percentages of silica. This effect can be shown and explained by comparing the fracture energy, G_c , against the weight % of silica nanoparticles. The toughening mechanisms have been identified as shear yielding in the epoxy plus debonding of the particles followed by void growth of the epoxy. The results would be expected to show a

positive increase in toughness as the percentage of nanoparticles increases, and a plateau at the maximum point. However, only about 15% of the silica nanoparticles have been observed to debond[2]. The small weight % of SiO_2 particles added in could have a greater effect on the overall curve, as a higher % of the silica particles may be able to undergo debonding and void growth than at high % of silica particles, and hence a steeper increase in G_c vs wt% than observed in the literature, such as from Hsieh et al. [2], at small weight% may be expected. For the effect of test rate, this study will start with a quasi-static rate, and then investigate the high rate effect. The higher test rate is expected to produce an increase in brittleness, and hence a reduction in the fracture energy. The hard silica particles are expected to show less of a reduction of toughness with increasing test rate when compared to the soft rubber particles. A fracture mechanics approach will be used to characterise the toughness of the epoxy.

Chapter 3

Literature review

3.1 Introduction

There is a long history in the use of adhesives in industry. There are many advantages in using adhesives in industry; one big advantage is the reduction of cost. There is also an improvement in product appearance, and an improvement in stress distribution and corrosion resistance, these factors enhance the design possibilities [5]. However, there are also drawbacks, for example adhesive bonding requires surface pretreatment of the substrates, it cannot join thick metallic components effectively, non-destructive testing methods are not applicable and it lowers the upper-service temperature [5]. In order to minimize these drawbacks, investigations into adhesive properties have been ongoing. To help the understanding and assessment of adhesive joints, finite element analysis (FEA) and fracture mechanics approaches are often used. These approaches can be used to predict service life and improve joint properties under different environments [5]. Due to the brittleness of adhesives, they are often modified by particles to improve their fracture toughness without changing their glass transition temperature, T_g [6]. However, some of the toughening mechanisms particle bridging, crack pinning and deflection are not applicable for nanoscale particles, as the particles are smaller than the crack opening displacement [6, 7]. Therefore the size of the particles used is one of the most important parameters in toughening epoxy. There is a higher critical stress for debonding for smaller particles, hence a reduced the amount of debonding would be expected. These toughening mechanisms can be investigated by scanning electron microscopy (SEM). Transmission electron microscopy (TEM) and transmission optical microscopy (TOM) [6] can be used to assess the dispersion of the particles. Agglomeration of the particles can reduce the toughness of the polymer, and will increase the viscosity of the uncured resin which may lead to processing difficulties. There can be a large increase in toughness of the modified epoxy due to the toughening mechanisms described below, and the

increased toughness is also maintained when the epoxy is used in fibre composites [3]. The toughness of the modified epoxy depends on the amount of crosslinking of the epoxy, the type of particles used, the particles size and their concentration [3].

3.1.1 Rubber-toughened epoxy

There has been a long history in the use of rubber particles in the toughening of epoxy. It is established that the larger the rubber particles, the higher the stress concentrations [8] and hence a higher amount of localised deformation. There are two principal types of rubber-toughened epoxy: carboxyl-terminated butadiene-acrylonitrile (CTBN) rubber and core-shell rubber (CSR) particles are commonly used. Carboxyl-terminated butadiene-acrylonitrile (CTBN) rubbers are rubbers containing butadiene and acrylonitrile as copolymers [9, 10]. They are added as a liquid rubber which dissolves in the epoxy resin and phase-separates to form particles during curing of the epoxy. Examples of different extents are amino-terminated-acrylonitrile (ATBN) and vinyl-terminated butadiene-acrylonitrile (VTBN). The use of block copolymers can also provide a different microstructure of phases (for example spherical micelles, vesicles and worm-like micelles) and hence can enhance toughening [11, 12]. There are two requirements for the CTBN rubber to be added to the epoxy: 1. the rubber must be able to dissolve in the epoxy first and then able to precipitate out during curing, and 2. the rubber must be able to react with the epoxide group to ensure good interfacial bonding between the particle and the epoxy. The particle size or diameter, d , of the CTBN rubber particles depends on the curing cycle, volume fraction, V_p , and concentration of the butadiene and acrylonitrile in the rubber. Larger rubber particles would be formed when a slow curing process is used. When the amount of rubber added increases, their diameter and volume fraction would increase too [13-15]. At high concentrations phase inversion can occur, where the rubber can become the matrix with epoxy particles inside [16]. The rubber would stay in a dispersed phase when its concentration is less than 20 wt% [17]. As a consequence, the addition of 10-20% of rubber particles provides the optimum toughening effect [17]. Other than that, phase separation can be reduced with the addition of silica nanoparticles [17]. Lee et al. [16] found that silica nanoparticles enhanced the toughness of the rubber-modified epoxy though the silica nanoparticles agglomerated [16]. Core-shell rubber (CSR) particles are pre-formed rubber particles with a soft core and a hard outer shell. The glassy polymeric shell can prevent the rubber particle aggregating and deforming during processing [11]. The CSR structure can be designed according to different factors (such as the chemical components of the

matrix). Multilayer structures are very commonly used [10]. The particles are pre-formed, so the diameter is not dependent on the curing process, unlike CTBN. The major toughening mechanisms for rubber particles are localized plastic shear yielding and particle cavitation [11], followed by plastic void growth, these are discussed in Section 2.5. The toughening mechanism in rubber toughening is due to the change in yield shear stress at the crack tip, which reduces the stress concentration of the region and enhances optimal shear banding. In order for this mechanism to occur, the stress fields near particles need to be overlapped and the spaces between them are critical [18].

3.1.2 Silica-toughened epoxy

It has been established that the addition of silica (SiO_2) nanoparticles can increase the toughness of epoxy [1, 7]. A sol-gel process is used to produce these silica nanoparticles (SiO_2), as liquid sol is transformed into a solid gel phase. The increase in the % of silica particles has shown a positive increase in toughness of the epoxy. By investigating different particle diameters (240 nm to 1.56 m) and volume fractions (0 to 0.35), Adachi et al. [19] found that the increase in volume fraction and the decrease in particle size of silica can greatly increase the fracture toughness of silica-modified epoxy [19]. There were also studies about the effect of bimodal silica particle sizes, where significant improvements in toughness were also found with the use of a mixture of particle sizes [20]. However the different sizes of silica particles used have not shown a significant effect in their modulus [6], which depends principally on the volume fraction. When adhesion is low at the interfaces between the silica particles and the epoxy, there would be more debonding of particles, and leads to more plastic void growth [7, 19, 21]. Shear banding and void growth are the major toughening mechanisms in silica nanoparticle-modified epoxy [6]. The toughening mechanisms in silica-modified epoxy is similar to other particles, but there is no crack pinning [1, 19], discussed in Section 2.5, because the particle diameter is less than the crack-opening displacement. Work on silica nanoparticle-modified epoxy performed by Hsieh et al. [19] has shown that some of the common fracture mechanisms (crack pinning, crack deflection and immobilised polymer around particles) can be discounted for silica nanoparticles. The major mechanism there was plastic deformation of epoxy. This means that the particles debonded from matrix, there were highly localised stress concentrated regions, which caused plastic deformation of the epoxy. There have also been studies of addition of both rubber and silica particles and they show good toughening effect [22]. It is because these two types of particles provide a good balance of modulus and toughness [23]. A synergy

effect was found, giving a significant increase in toughness, from studies by Hsieh et al. [24] and Manjunatha et al. [23], with the use of a combination of silica and CTBN particles. With the use of block copolymers or CSR with silica particles, synergy effect in terms of toughness was also found to increase in the study from Chen et al. [25, 26].

3.1.3 Other materials used

PES

As toughening using thermoplastic did not affect its Tg, there have been many investigations into thermoplastic toughening of epoxy resins performed with thermoplastics, such as commercial polyethersulphone (PES).

There are a few criteria in order for thermoplastic to achieve high toughness, including [27]:

- 1 Thermoplastic backbone: which provide good thermal stability, soluble in epoxy and phase separate when cure.
- 2 morphology: co-continuous/ phase inverted morphology provides the optimum toughness
- 3 reactive endgroups: might not be necessary, but can be an advantage
- 4 crosslink density: the high crosslinking in epoxy would increase toughness, which is contrast to rubbers.
- 5 molecular weight: increased in molecular weight can increase toughness of the system but can also depends on the practical use requirements.

To sum up, high toughness is achievable given that co-continuous phase is present with good thermal stability from the thermoplastic backbone and the epoxy used has a high crosslink density [27]. However, a high crosslink density and molecular weight are not necessary, as these factors would varies for different applications. The morphology has an important factor in the toughness of the PES modified epoxy, there are three phases found when different % of particles were added:

At low %: particles of PES

At medium %: Co-continuous (CC) structure

Co-continuous phase: One phase inside the other, usually formed when the viscosities are equal, 50:50.

When % of particles is large: Phase inversion

Co-continuous is found to have the optimum toughness [12, 27] due to the lack of adhesion in a single phase structure. When phase separation occurs, rubber would aggregate into micron-sized spherical particles and the addition of silica particles would

reduce phase separation, and it is found by J.H. Lee et al [16] that the silica particles added in can enhanced the toughness of the rubber modified epoxy as the nano-silica particles agglomerated. It is due to the small particle size of nanosilica would reduce void size as a higher energy is needed for void to grow, hence enhance toughening.

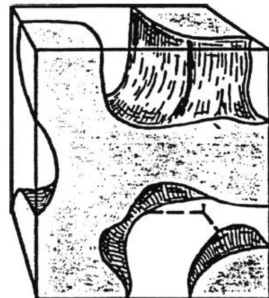


Figure 3.1: Co-continuous phase [11]

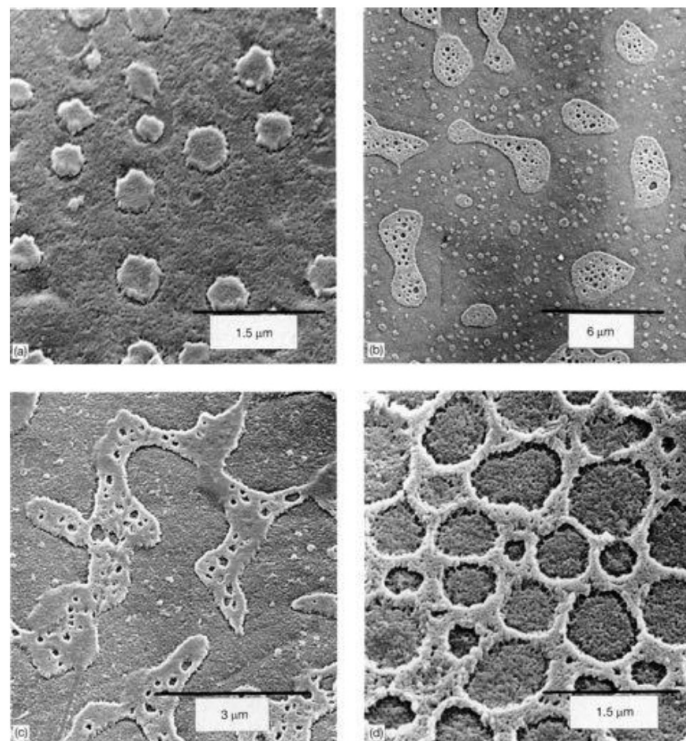


Figure 3.2: Different phases of PES: a) Particulate b) Transition between particulate and co-continuous c) Co-continuous and d)Phase-inverted microstructure[28]

The amount of phase separation can be calculated by the Fox equation, where it

calculated amount of rubber that did not phase separated. Phase separation equation-Fox equation:

$$\frac{1}{T_g} = \frac{W_{ep}}{T_{g,e}} + \frac{W_r}{T_{g,r}} \quad (3.1)$$

Where W=weight fraction, Subscripts: ep=epoxy, r=rubber particles And Tg=glass transition temperature

PES particles are suitable in many other applications, for example as a coating in solvents, use in films and hollow-fiber membranes. The use of PES is well established, but not under brittle failure (such as low temperature testing and high rate effect using DMA). Therefore, this study would concentrate on comparing the established results with tests under low temperature conditions. More brittle failure and small increase in fracture energy would be expected, but failure mechanisms were expected to be similar to the other particles used.

3M ceramic microspheres W210

Ceramic microspheres are highly used as an additive in applications such as paint, however, the use of it in epoxy as a toughening agent is not common. This might be due to the complexity in the different phases formed. Hence, more studies about the use of ceramic microspheres in epoxy is desired in the future.

3.1.4 Fracture mechanics

There are different theories in the study of fracture mechanics, the two main approaches to quantify toughness are by the consideration of the energy approach and stress intensity approach [17]. Linear elastic fracture mechanics (LEFM) is used in considering the fracture circumstances in epoxy polymers indicate a linear elastic response with plasticity confined to only a small zone at the crack tip. At the crack tip, there are different directions of stresses; therefore, there would be different modes of loading. All the three modes of loading (mode I, mode II and mode III) would occur at the crack tip, see Figure 1, all of them are considered [17], but mode I is the most critical one as it has the lowest energy and hence the most likely to cause fracture.

3.1.5 Fracture toughness

There are two approaches to calculate fracture toughness, one is based on energy while the other considers the stress intensity of the crack. 1) Energy approach: fracture

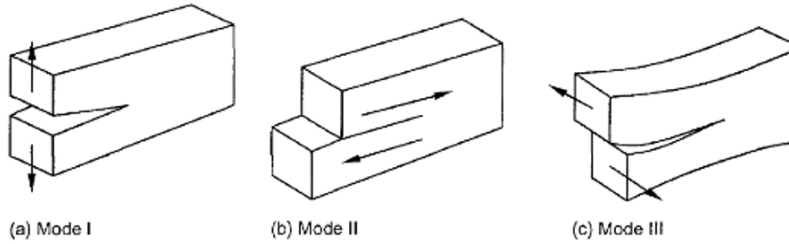


Figure 3.3: The different modes of loading [27]

occurs when sufficient energy is released from the stress field by growth of the crack. The energy criterion [28] is:

$$\frac{1}{B} \frac{dU}{da} \geq G_c \quad (3.2)$$

where B = width of crack front, U = potential energy of the loaded specimen, a = crack length and G_c = fracture energy (critical strain energy release rate). For bulk linear elastic behaviour away from the crack tip, G_c is given by:

$$G_c = \frac{P_c^2}{2B} \frac{dC}{da} \quad (3.3)$$

where P_c = load required for fracture (crack propagation), and C = compliance (displacement/load) of the specimen. 2) Stress intensity factor approach: The critical stress parameter is the critical stress intensity factor, K_C , which is expressed in a slightly different way under plane stress and plane strain [17]. To be conservative, the minimum value is desired, so plane strain conditions are considered in tests. For plane stress (i.e. a thin sheet):

$$K_c^2 = EG_c \quad (3.4)$$

$$K_c^2 = \frac{E}{1 - v^2} G_c \quad (3.5)$$

where E = Youngs modulus and v = Poissons ratio [17]. The correlation between G_c and K_c in plane strain is [29, 30]:

$$G_c = \frac{(1 - v^2) K_c^2}{E} \quad (3.6)$$

The plane stress and plane strain conditions also have an effect on the plastic zone

at the crack tip; the radius of the plastic zone at the crack tip, r_y , see Figure 2, can be expressed as [29]: For plane stress (i.e. a thin sheet):

$$r_y = \frac{1}{2\pi} (K_c/\sigma_y) \frac{dC}{da} \quad (3.7)$$

For plane strain (i.e. a thick sheet):

$$r_y = \frac{1}{6\pi} (K_c/\sigma_y) \quad (3.8)$$

The crack opening displacement or d_{crack} [17] (which is in the y direction) is given by:

$$d_{crack} = \left(\frac{K_c}{\sigma_{yt}} \right)^2 e^y \quad (3.9)$$

where K_c is measured stress intensity factor at the onset of crack growth, σ_{yt} is tensile yield stress and e_y = yield strain [31]. All of these concepts are used in considering the right thickness of adhesive in a joint [32], which must be greater than $2r_y$ for the full toughness to be developed.

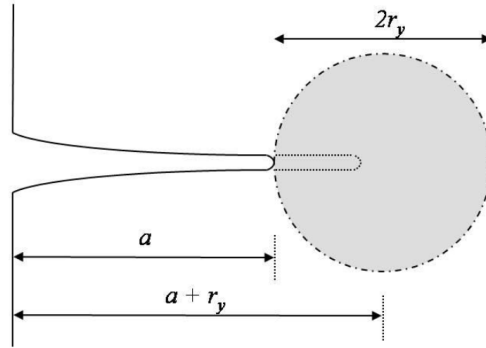


Figure 3.4: Plastic zone model

3.1.6 Tapered double cantilever beam (TDCB)

The tapered double cantilever beam (TDCB) test and the double cantilever beam (DCB) test are LEFM methods that are commonly used in determining the fracture energy, G_C , of epoxy adhesive joints, because these methods can determine the fracture resistance of crack to initiation, propagation and arrest. Moreover, the R-curve (resistance-curve) of the adhesive fracture energy against crack length can also be found from the data obtained in the test, as the toughness may increase with crack length due to additional

toughening mechanisms. Therefore, they are very useful in providing information about the fracture performance of the adhesive [33, 34]. The TDCB specimen is designed such that the fracture energy, calculated using Equation 2.2, is not dependent on the value of crack length, so the rate of change of compliance with crack length is constant [35]. The value of G_C can be calculated using Equation 2.9. The relationship between compliance and crack length is kept constant by varying the height of the specimen with the equation [33, 34]:

$$\frac{dC}{da} = \frac{3a^2}{h^2} + \frac{1}{h} = m \quad (3.10)$$

where a = crack length, h = height of substrate beam at a crack length a , and m = specimen geometry factor (constant). Both TDCB and DCB specimens use the same principles in the test method (mode I, in-plane tensile), but TDCB is more stable as its shape reduces the stress concentration at the start of the crack, hence improving the accuracy of the results [34]. The TDCB is more suited to high rate tests as the failure load does not depend on the crack length, and hence the crack length does not need to be measured. There are two main categories of failure types, (i) cohesive and (ii) adhesive/interfacial failure. Cohesive failure is when failure happens within the adhesive layer, see Figure 3a. This occurs when the interface strength is high [36]. Adnan et al. [36] showed that cohesive failure can occur under tensile loading or shear loading, where adhesive deformed through cavitation and bulk shear [36]. Adhesive or interfacial failure is when failure is in-between the adhesive and substrate [37], due to the presence of low interfacial strength [36], see Figure 3b. Therefore the fracture energy measured would be that of the adhesive/substrate interface, but not of the adhesive itself. Aluminium alloy has a relatively high yield stress, so a plastic zone cannot be formed there and the measured fracture energy will be much lower than the cohesive value.

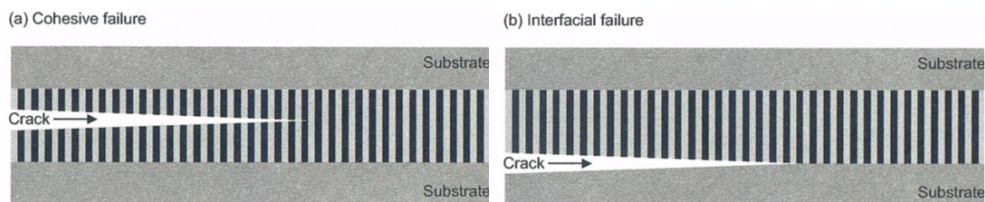


Figure 3.5: Failure modes diagram a) cohesive, and b) interfacial failure [16]

3.1.7 Types of crack growth

Crack growth in the TDCB test is not always under a stable manner. There are three types of crack growth (see Figure 4). The brittle and stable type was termed Type C, where the brittle adhesive would usually have high yield stress, little plasticity and the crack would be sharp. This is a typical of epoxy adhesives. Type B is stick-slip, which is unstable crack growth, it produces a significant pattern (where initiation and arrest points can be seen) on the load against displacement curve, it is brittle but has not got as high yield stress as type C. Type A is stable ductile crack growth, where the adhesive has high ductility and a rough or torn fracture surface, the fracture behaviour links to the testing temperature, and usually has a lower yield stress. This high crack-tip plasticity and blunting causes the ductile failure and stable crack growth. Smooth, featureless surfaces can be observed with continuous crack propagation [17]. When the test rate is increased, there is less crack tip blunting [32]. Less load is required to propagate the crack than to initiate it and hence stick-slip failure occurs. When the temperature is low and the loading rate is high, crack initiation only needs a minimum yielding at the crack tip; therefore the crack is sharp and results in a low stress intensity factor. It is the same when there is a very high crack tip strain rate with very short deceleration times at arrest points [31]. When the temperature is high, the yield stress reduces and plastic flow could be increased resulting in more crack tip yielding. This results in a larger stress intensity factor [31] and hence Type A crack growth occurs. The transition between the types of crack growth depends on the temperature and usually a clear state of transition occurs, where the changes in characteristics of the points are very significant [31, 32]. Figure 4 shows the three different fracture types, which are extended to four types of crack growth under high rate testing (see Section 2.7) [38].

3.1.8 Single-edge notch bending (SENB)

Single-edge notch bending (SENB) tests are used with bulk materials rather than adhesive joints, and are designed to focus on the fracture energy, G_c , and fracture toughness, K_c , of the material. SENB testing can be performed under both quasi-static and high rates. However, there are dynamic effects under high rate that can cause large oscillations in the results graphs. The use of damping and a displacement method can ensure that this is usually not a problem. According to ISO 13586 standard [39], SENB specimens (see Figures 5 and 6) should be 6 mm thick, 12 mm in width and 60 mm in length, with at least 6 replicate tests for each formulation.

Due to the conditions of high rate tests in this study, linear elastic fracture mechanics

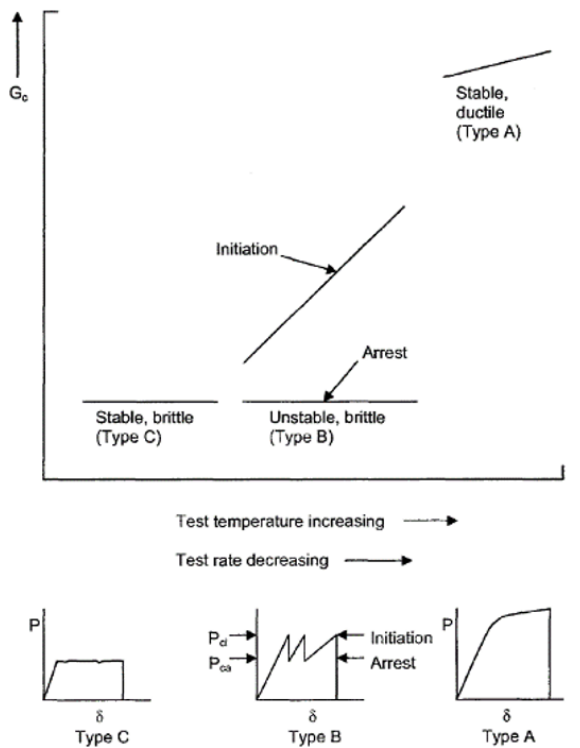


Figure 3.6: Graphic representation of different fracture types under different testing conditions [16]

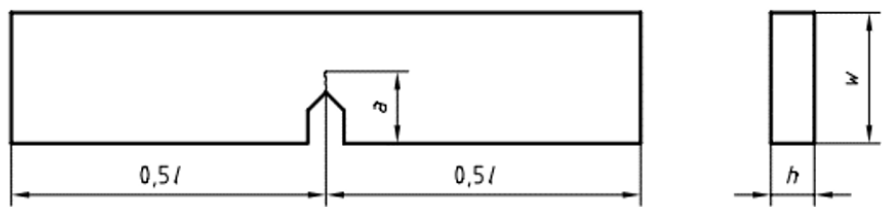


Figure 3.7: Single edge notch bending (SENB) specimen [39]

(LEFM) method was used in determining the peak load from SENB testing (where energy method would not be as accurate under high rate conditions of this material). The peak load values were then used to calculate fracture toughness or critical stress intensity, K_c , and fracture energy, G_c . Fracture toughness, K_c , can be found by using:

$$K_c = \frac{4P}{B} \frac{\sqrt{\pi}}{W} \left[1.6 \left(\frac{a}{w} \right)^1 / 2 - 2.6 \left(\frac{a}{w} \right)^3 / 2 + 12.3 \left(\frac{a}{w} \right)^7 / 2 + 21.8 \left(\frac{a}{w} \right)^1 / 2 \right] \quad (3.11)$$

where P = critical applied load (Pmax), B = thickness of specimen, a = crack length and W = width of specimen, see Figure 5. The fracture energy can be calculated for the LEFM method [40] using:

$$G_c = \frac{((1 - v^2) K_c^2)}{E} \quad (3.12)$$

where the Poissons ratio $v = 0.35$ [40], and E is the tensile Youngs modulus. To make the results valid, there are two criteria which must be met [39]:

1. Size calibration:

$$B, a, (W - a) > 2.5 \frac{K_c}{y t} \quad (3.13)$$

2. Maximum fracture load, Pmax:

$$\frac{P_{max}}{P_Q} < 1.1 \quad (3.14)$$

where P_{max} = maximum load or 5

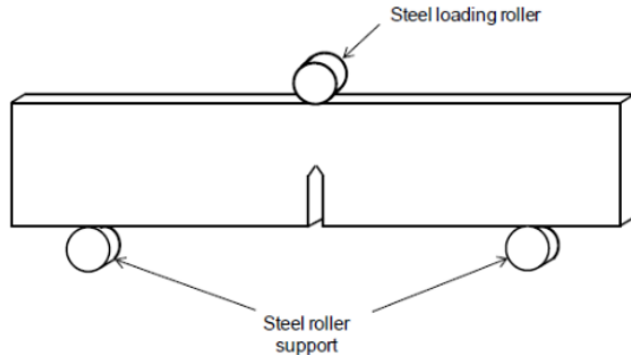


Figure 3.8: Single edge notch bending (SENB) test, loaded in three point bending [40]

3.2 Toughening mechanisms

3.2.1 Introduction

The addition of particles normally increases the fracture energy of epoxy polymers. The common mechanisms of toughening according to Kinloch et al. [32] are: 1. Stretching and tearing or debonding of rubber particles: Stretching would increase the toughness, and followed by debonding or tearing, 2. Brittle fracture of a rigid particle, 3. Crack deflection, 4. Crack pinning, and 5. Yielding near the crack tip (the crack tip becomes blunt, plastic zone size increases and yield occurs) [32]. While the major toughening mechanisms in rigid silica particles are debonding, plastic void growth and shear yielding. Mechanisms discussed below including shear bands and shear yielding, crack pinning, crack deflection, cavitation, debonding and rubber bridging.

3.2.2 Shear bands and shear yielding

Shear banding is produced when there is a tensile stress applied to the polymer chains, and is caused by the orientation of polymer chains. It is plastic deformation due to shear force [29], which absorbs energy and hence increases toughness. It is a mechanism that involves localized inhomogeneous plastic deformation [32]. It occurs when there is a brittle fracture; it involves only little energy dissipation. But when there is a higher shear deformation around the crack tip, propagation of crack would become ductile. Therefore it would blunt the crack tip, and this leads to an increase in toughness of the material. When there is bulk yielding and fully ductile failure behaviour, shear yielding can be limited [32].

3.2.3 Crack pinning

The crack can be pinned when approaching particles, and so bows out between them. As the energy is proportional to the length of the crack front then extra energy is required, increasing the toughness. The crack then breaks away and moves forward from the particles, producing tails at the particles. This is due to presence of rigid particles. Secondary cracks could be formed between particles if bow out is followed by crack pinning [41]. This would produce a new fracture surface and an increase in the length of crack front. The consequence of formation of new surfaces is the increase in crack resistance, as energy needed would be higher [41], see Figure 7. Crack pinning can only happen when the diameter of a particle, $d_{particle}$, is larger than the crack opening displacement, d_{crack} , so will only occur with large particles (i.e.micron sized) [32]. For

large particles, the main toughening mechanisms are pinning, deflection, debonding with void growth and shear yielding (i.e. shear bands). Pinning and deflection would not occur in small particles (nanometre-sized particles), as nanoparticles would be too small for these mechanisms to occur (as the diameter of the particle, $d_{particle}$, is a lot smaller than d_{crack}). Instead, the mechanisms for nanoparticles are debonding followed by void growth and shear yielding.

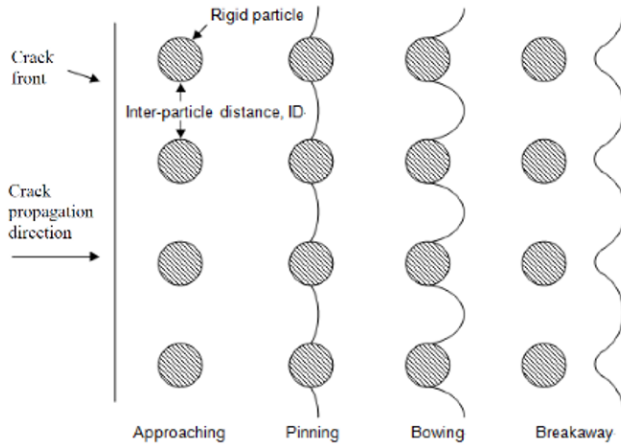


Figure 3.9: The process of crack pinning [29]

3.2.4 Crack deflection

When the crack is approaching a rigid particle, it is deflected around the particle, see Figure 8, as it cannot propagate through the particle which is tougher than the epoxy. This tilts the crack, so the local crack propagation is a mixed mode (I/II) not pure mode I. Thus more energy is required, as mode II requires more energy than mode I, increasing the measured toughness. There is usually an angle of where the crack tilts, and this would depend on the stress and the particles there. Crack deflection also causes a tail to be formed behind a particle. As for crack pinning, crack deflection requires that $d_{particle} > d_{crack}$ [32].

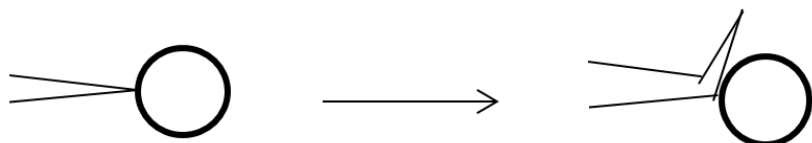


Figure 3.10: Crack deflection by a particle, after [32]

3.2.5 Cavitation

Cavitation is when the triaxial stresses in the plastic zone at the crack tip cause a soft particle to fail internally. This causes a void within the particle, see Figure 9. It causes blunting of crack under the riaxial stress state [42]. It happens before the shear yielding or plastic void growth, it doesnt give a significant toughening effect on its own, but plastic deformation involving enlarged voids, which require a higher surface and strain energy hence increase energy dissipation [43] increase the toughness. It was found that there would be more initiation of cavitation if particles had a higher Poissons ratio [44] or a larger diameter [45].

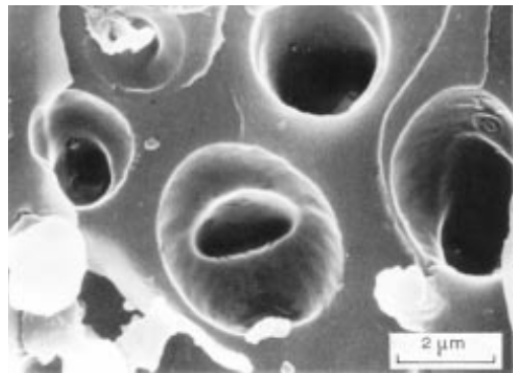


Figure 3.11: SEM image of cavitation of rubber particles [5]

3.2.6 Debonding

This is when the interfacial adhesion between the particle and the epoxy is poor, so the particle becomes detached from the epoxy. Surface debonding involves only a small amount of energy being absorbed. However plastic deformation and void growth follow debonding, and these processes can absorb a significant amount of energy [29], see Figure 10.

3.2.7 Rubber bridging

Bridging occurs when rubber particles are stretched and forms a bridge in-between the two fracture surfaces of a crack. It is only for large (micron sized) particles. Stretching of the rubber will require energy, but it is not a major mechanism and does not show any significant effect in rubber particle toughening [29], see Figure 11.

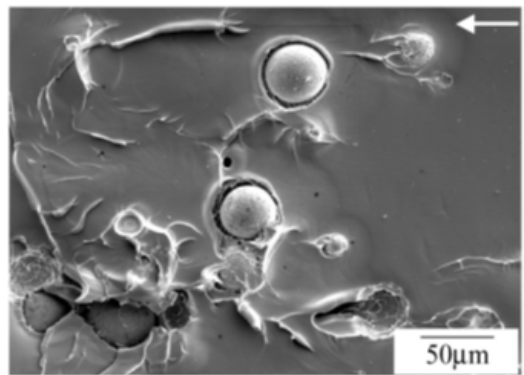


Figure 3.12: SEM image of debonding of glass particles [46]

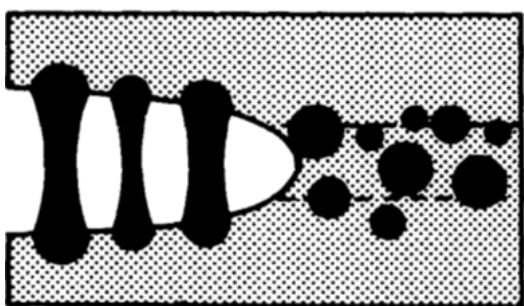


Figure 3.13: Rubber bridging model [47]

3.2.8 Plastic void growth

Figure 12 below shows plastic void growth of rubber modified epoxy. Debonding of hard particles or cavitation of soft particles relieves the constraint on the epoxy. The triaxial stress in the plastic zone at the crack tip causes the voids to grow and hence dissipated energy [48]. Plastic void growth has a great effect on the fracture energy measured. More regarding plastic void growth of rubber modified epoxy are discussed in SEM images in the experimental results section.

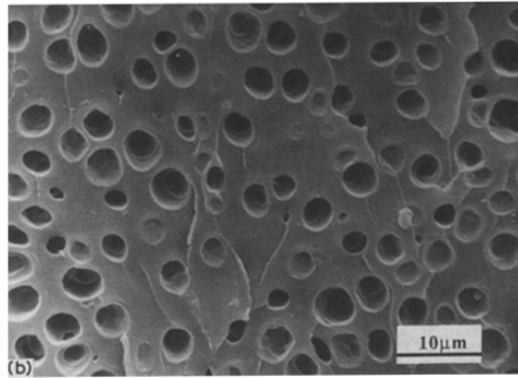


Figure 3.14: Figure showing plastic void growth of epoxy (tested at 40°C) [48]

3.2.9 Modelling toughening mechanisms

The toughness of the epoxy can be predicted using analytical models, e.g. [2, 3]. In theory, there would be 100% cavitation and void growth for soft particles, or debonding and void growth for rigid particles. However, all of the mechanisms are affected by the particle distribution, particle size, volume fraction and stress field due to the neighbouring particles [49]. Therefore, not all of the particles can undergo the toughening mechanisms. The percentage of voids is low when particles are too close, as the energy required for voiding would be too high [2]. However voids can be formed further away from a voided particle. According to this theory, when there is a large % of silica, there would only be 14.3

$$G_c = G_{\text{shear}} + G_{\text{DB+VG}} + G_{\text{unmodified}} \quad (3.15)$$

where G_c = fracture energy, G_{shear} = fracture energy from shear-banding, $G_{\text{DB+VG}}$ = fracture energy from debonding and void growth and $G_{\text{unmodified}}$ = fracture energy from unmodified epoxy. Expressions for these terms have been derived by Huang and

Kinloch [50] and Hsieh et al [29]. More about toughening mechanisms is discussed in later sections, such as Sections 2.7.4 and 2.7.9.

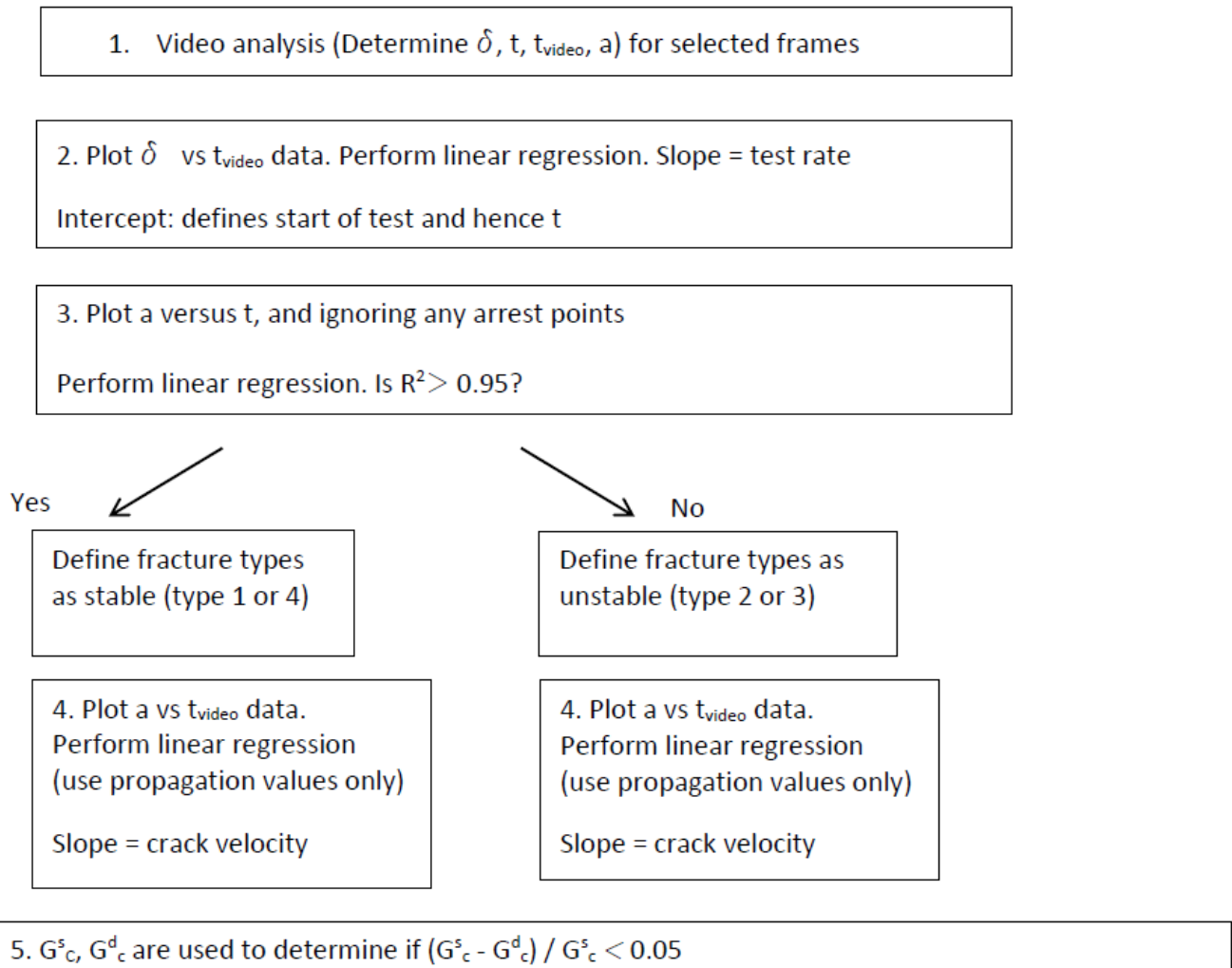
3.2.10 High rate testing

There are very limited studies on high rate testing of toughened epoxies due to the challenges involved, such as: 1. The more complicated failure mechanisms and dynamic effects in high rate can cause problems with accuracy of the analysis and the results; 2. The analysis needs to be according to the type of fracture (stable propagation and stick-slip failure are analysed with different approaches), and 3. Due to the increase in the kinetic energy in the high rate test, this energy must be accounted for in the results [51]. Therefore a data reduction strategy was developed by Blackman et al. [52] for accurate high rate data analysis. The data reduction strategy is summarised in the flow chart shown in Figure 13 [52]. This protocol was first used in DCB specimens using a frame-by-frame analysis approach. Four groups of fracture types were developed in the protocol, more details are discussed in high rate test experimental Section 5. This protocol enables the analysis of high rate results with the account of dynamic effects, hence the reliability of the data is assessed.

There are many factors that can affect the high test rate results, and the main considerations are stated below:

3.2.11 Uncertainties

When measured load values were reliable means that there was no significant dynamic effect that altered the values, so type 1 and 2 were considered to be reliable. Other uncertainties were also taken into account of the reliability of the results, such as uncertainties from the instruments used and the analysis types. For example, it was reported that there was a 6% uncertainty when analysing type 1 and 2, while there was a 4% of uncertainty in analysing type 3 and 4 [53]. Thus the uncertainties vary slightly when the different types of analysis were used, but are small. 2.7.2 Expected effects It is expected that there would be more unstable crack growth when the rate of test increases. This was found by Blackman et al. [54] that at test rates higher than $8.3 \times 10^{-5} ms^{-1}$, unstable crack propagation occurs. It is found that the initiation and arrest points are difficult to distinguish when rate is at $1 ms^{-1}$, this could be due to the decreased in crack-length distance between initiation and arrest points [55]. Identifying crack initiation and arrest points at rates higher than $10 ms^{-1}$ is impossible [56].



where δ = beam opening displacement, a = crack length, t = time, t_{video} = time from video, G_c^s = static value of adhesive fracture energy and G_c^d = dynamically-corrected value of G_c^s

Figure 3.15: Flow chart for data reduction strategy of TDCB test [52]

3.2.12 Geometry factor

Flexural rigidity of the specimen is highly related to test geometry. TDCB has a high flexural rigidity when compared to DCB, hence could provide more reliable results at both low and high rates. The larger size in specimens also reduces the thermal shrinkage between substrate and adhesive layer, as the data reduction strategy does not consider residual stresses, TDCB specimens have their advantage. However, this larger geometry can also bring more significant inertial effects that could lead to unstable crack growth [57]. The geometry factor is also affected by the toughness of the adhesive, the tougher the adhesive is, the less that it is affected by the inertial effects. Therefore, it is expected that TDCB specimens would provide more reliable results when compared to DCB specimens.

3.2.13 Toughening mechanisms

It is expected that when rate is high, the toughening mechanisms would become less effective, which means there would be less plastic deformation due to the lower energy dissipation at crack tip as the yield stress will increase with test rate [53]. More about the data reduction method is described in the experimental part of this report.

3.3 Conclusions

Many aspects of the use of particles in modifying epoxy have been reviewed. Significant improvement in toughness has been found in most of the studies available. The level of improvement can be highly affected by the dispersion of the particles and the individual toughening mechanisms. Other factors that contribute to the properties of joints are such as surface treatment and adhesive thickness, because they would affect the failure type and crack growth type. Epoxy toughness can be quantified using a fracture mechanics approach, such as the energy approach using TDCB specimens. At quasi-static test rates the analysis is relatively straight forward. However, at high test rates the analysis depends on the specimen behaviour (e.g. type of crack growth) and may be affected by dynamic effects. Therefore, fewer studies have been conducted using high rate, and more investigations and understanding of their toughening mechanisms are required for further improvement of the material, especially at high rate.

Chapter 4

Experimental work

4.1 Introduction

Nanoparticles were added in at 0.5, 1, 2, 3, 5, 10, 15, 20 weight % and the maximum concentration of 25.4 weight %. The results were expected to show a positive increase in toughness with increasing weight % of silica particles, followed by a plateau at the maximum point. However, the low weight % of the silica particles may show a steeper increase, as hinted in other work [14]. This outcome will be particularly linked to the mechanisms of fracture, especially variations in the percentage of silica particles which undergo debonding and void growth. The properties of silica-modified epoxy would be compared with CSR-modified and hybrid (silica and CSR) ones, where they have the same % of particles as the silica-modified specimens up to 10% (more about CSR in Section 3.2.1 below). This is due to the larger particle size of CSR that cannot be mixed properly when the % of particle is higher than 10 weight %. TDCB specimens were prepared using a range of different concentrations of nanoparticles. As high rate tests involve more analysis and with the limited storage of data from the camera, approximately four different concentrations of nanoparticles would be used at each high rate test, unlike the bulk specimens (where all formulae were tested in the bulk specimens). The experimental results will be compared to those from finite element modelling currently underway.

4.2 Materials and methods

4.2.1 Materials

There were three materials used in mixing of the adhesive (epoxy, nanoparticles and hardener): Epoxy resin: Araldite LY 556 (Huntsman Advanced Materials, Belgium), which is a diglycidyl ether of bisphenol A (DGEBA) with an epoxy equivalent weight

(EEW) of 185 g/mol and density of 1.175 g/ml. As some of the 16 nanoparticles are supplied in epoxy resin, the stoichiometric amount of the epoxy for the silica, CSR, epoxy and hardener were found by using their equivalent weight. Hardener: Albidur HE-600 (Nanoresins, Germany), which is an accelerated methylhexahydrophthalic acid anhydride with a density of 1.08 g/ml. This was used at a stoichiometric ratio of 1:1.09 to the resin. Nanoparticles: 1. Silica: Nanopox F400 (Nanoresins, Germany). It is a DGEBA master batch with 40 weight % of silica particles in DGEBA and a density of 1.4 g/ml. These silica particles have a mean diameter of 20 nm, they are in the form of a colloidal silica sol. The silica has been surface-treated by the manufacturer to prevent agglomeration. 2. CSR: Paraloid EXL-2300G (Rohm and Haas, UK). They are powder form core-shell rubber particles sieved into three sizes: \leq 106 μm , in-between 106 μm and 38 μm and \geq 38 μm . Size of in-between 106 μm and 38 μm were used in this work. 3. Hybrid: The same % of silica nanoparticles and CSR were mixed into the epoxy, e.g. 5 weight % of silica plus 5 weight % of CSR.

4.2.2 TDCB specimen preparation

Aluminium alloy substrates (grade EN AW 2014A) were used in preparing the TDCB specimens. The substrates were first cleaned with acetone, and grit-blasted with 180/220 mesh alumina grit. The surface was then cleaned with acetone again before chromic acid etch treatment. The substrates were placed in a 70°C chromic-sulphuric acid bath for 10 minutes (composition of bath is 0.1 kg of copper sulphate, 3.87 kg of sodium dichromate, 0.06 kg of powdered aluminium, 7.2 litres of sulphuric acid (s.g. 1.84) and 40 litres of distilled water) [58]. They were then rinsed with tap water and placed in a tap water bath for 15 minutes. They were rinsed with distilled water and then dried in an oven for 5 minutes. The epoxy and hardener were mixed and degassed in a vacuum oven. The mixture was spread on the substrate using a spatula, ensuring that it covers the whole surface. A piece of polytetrafluoroethylene (PTFE) film (Aerovac, UK) of 60 mm long was placed at one end for creating a pre-crack, and a stainless steel wire of 0.4 mm diameter was placed at each end of the substrate to provide a constant thickness of adhesive layer of 0.4 mm. A bonding jig was used to clamp the substrates together, see Figure 14. Three specimens are prepared each time; this can provide a higher consistency of the specimens conditions (as they would be prepared with the same jig). The jig was coated with release-agent Frekote 700-NC (Loctite, UK) to prevent the adhesive sticking to the jig and allowing removal of the specimens. The jig was placed in a fan oven, and the adhesive was cured. After curing, the excess

adhesive was removed using sandpaper. The joint was coloured by white correction fluid and a paper ruler marked in millimetres was secured under the bonding line to allow the crack length to be measured, see Figure 14.



Figure 4.1: TDCB bonding jig



Figure 4.2: TDCB specimens

4.2.3 Differential scanning calorimetry (DSC) tests

The completeness of curing was confirmed by measuring glass transition temperature, T_g , of the specimens using differential scanning calorimetry (DSC) [59]. There were two different curing cycles used in the 1st and 2nd sets of control specimens to compare the T_g of the specimens. The two curing cycles used were: Control 1st three specimens: Preheat at 60°C , ramp at $1^\circ\text{C}/\text{min}$ to 95°C , dwell for 1 hour, ramp at $1^\circ\text{C}/\text{min}$ to 165°C , and dwell for 2 hours, ramp at $2^\circ\text{C}/\text{min}$ to room temperature (20°C). 400°C Control 2nd three specimens: Ramp at $1^\circ\text{C}/\text{min}$ to 95°C , dwell for 3 hours, ramp at $1^\circ\text{C}/\text{min}$ to 155°C and dwell for 5 hours, ramp at $2^\circ\text{C}/\text{min}$ to room temperature (20°C). DSC works by measuring the amount of heat energy needed for increasing temperature of the sample. There were two heating and cooling cycles in a DSC curve, shown in Figure 16.

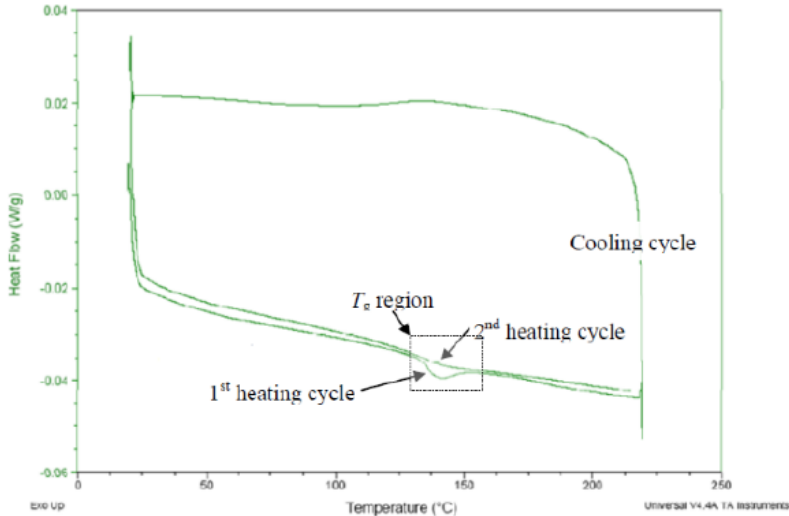


Figure 4.3: Heating and cooling cycle in DSC [29]

For the DSC measurements, 10 mg samples were used. Samples were taken from the TDCB joints and weighed. The samples were heated from 30 °C to 180 °C, at a rate of 10 °C/min. The T_g was obtained from the second heating cycle. The glass transition temperature, T_g, measured was 133.2 °C for both curing cycles, which was in the expected range (expected value is 148.0 °C measured from DMA). It is found by Mohammed et al. [1] that T_g of the same unmodified epoxy was 153 °C, the value was not affected by the addition of silica particles. The T_g value can be slightly different when there is a different curing cycle used, as well as different specimen size. Therefore no adjustment is needed for the curing cycle use in all the other specimens. The curing cycle for all the rest of specimens was the first one: Preheat at 60 °C, ramp at 1 °C/min to 95 °C, dwell for 1 hour, ramp at 1 °C/min to 165 °C, and dwell for 2 hours, ramp at 2 °C/min to room temperature (20 °C)

4.2.4 Quasi-static rate tests

The TDCB tests were performed using a tensile testing machine with a cross-head displacement rate of 0.1 mm/min, see Figure 17. The specimen is fixed with a load-cell of 5 kN, and the load and displacement were recorded by the testing machine. The experiment was set up with a travelling microscope for measuring the crack length. The crack length was measured to a precision of 0.5 mm.

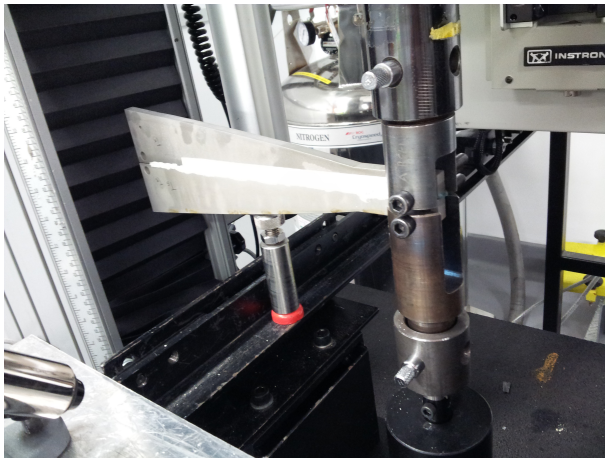


Figure 4.4: TDCB test set up

4.2.5 Initial loading and re-loading

There were two loadings preformed in each quasi-static TDCB test: 1. Initial loading (precracking) and 2. Re-loading (actual loading) [34]. 1. During the initial loading, the test was stopped when the crack travelled to the end of the starter film and started to propagate into the adhesive, which would be the insert length (a_0). The specimen was then unloaded and crack would be closed up, specimen was unloaded slowly at a constant cross-head rate of 1 mm/min, and readings were taken at about every 0.1 mm of change of extension. The unloading curves should be able to go back to original, a slightly negative force when the extension was zero was acceptable, as there might be slight inaccuracy from reading, but a large negative load value would be an indication of permanent deformation of the substrate and test would not be valid. 2. Re-loading rate was the same as the initial loading (0.1 mm/min). The first crack propagation would be the precrack value (NL, Visual and Max/5%). The crack length readings were taken until specimen was opened up completely or until there were enough data points. At least 15 readings are recommended by the protocol from Blackman et al. [57].

4.2.6 Initiation and propagation values

There were three types of initiation values, and visual observation was used in this study [28]: Non-linear (NL): There is a linear region at the beginning of the graph where material can go back to original shape with linear elastic deformation. NL is the point at which the elastic behaviour ends. Visual observation (Vis): It is the first visible crack propagation. 5% or Max: It is the maximum point from the curve, or where a

line of initial compliance +5% cuts the graph. The value which occurs at the smaller displacement should be used. The thickness of the substrate was measured at 3 points (near both ends and at the middle) of the beam before and after bonding, in order to monitor the thickness of the adhesive layer. The height of specimen is tapered such that a constant specimen geometry factor, m, is used

$$\frac{3a^2}{h^2} + \frac{1}{h} = m \quad (4.1)$$

where a = crack length, m = 2 mm⁻¹, h = thickness of substrate beam at a crack length of a [28].

4.2.7 Determination of G_c in TDCB

There are three methods in determining the value of G_c : experimental compliance method (ECM), simple beam theory (SBT) and corrected beam theory (CBT) [60]. Their equations are shown below. The use of ECM and CBT can provide more accurate results [34] than SBT.

Experimental compliance method (ECM):

$$G_C = \frac{nP}{2Ba} \frac{F}{N} \quad (4.2)$$

where P = critical load, = displacement, a = crack length, B = width of specimen, F = displacement correction and N = load-block correction.

Simple Beam Theory (SBT):

$$G_C = \frac{P^2}{2B} m \quad (4.3)$$

Corrected Beam Theory (CBT):

$$G_C = \frac{4P^2m}{E_s B^2} \left(1 + 0.43 \left(\frac{3}{ma} \right)^{1/3} \right) \quad (4.4)$$

The results would include: 1. G_c against weight % of particles at slow test rate. 2. G_c against weight % of particles at different higher test rates for certain weight % of particles. 3. A section of the TDCB specimen would be cut and the fracture surface examined using FEG-SEM, to measure the % of voids.

4.2.8 Field emission gun scanning electron microscopy (FEG-SEM)

Field emission gun scanning electron microscopy (FEG-SEM) was used to investigate the fracture surface of epoxy. FEG-SEM provides higher resolution of images which reveal more information from the fracture surface. Evidence of failure mechanisms such as river lines would provide supporting evidence to the results found. Gold coating was applied to increase conductivity of specimens. It was performed by using EMI TECH K575X coater at 120 mA for 1 min. Electrical conductivity of specimens is to make certain by applying some silver paint at the side of the specimens. The amount of coating applied on the specimen needed to be optimum, because thin coating can charge the specimen up, resulting in difficulties with beam focusing and aperture or stigmation correction. When coating is too thick, fine details could be masked.

4.2.9 Scanning electron microscopy

SEM imaging was performed with Hitachi S-3400N VPSEM, with an accelerating voltage of 15 kV and 10 kV for low magnification imaging. This was used to investigate the fracture surface of epoxy with larger particles.

4.2.10 Fracture energies

The three methods used to calculate the fracture energy values were expected to give similar values, and they did. Table 1 compares the G_c values for the control (unmodified) epoxy for the three methods. Simple beam theory (SBT) usually gives a slightly lower value according to previous experience [34], and these data fit this observation. There are two types of crack propagation - stable propagation and stick-slip, see Figure 4. These values cannot be averaged, and need to be considered separately, such as comparing averaged initiation values etc. [34]. This is expected to show increase in the amount of stick-slip when test rate is increased [52]. Similar fracture energies values of the control specimens were found when compared to studies from Hsieh et al. [24], more comparison of results are shown in the next Section.

Control

Table 1 and Figure 18 show the control TDCB fracture energies from the SBT, CBT and ECM methods. The fracture energies from the control specimens were at the lowest end of results when compared to studies in the past, but these results were realistic [61]. The lower fracture energy values might be due to the thin layer of adhesive applied on the

joint, and with relatively small standard deviations, the control results were considered to be reliable.

Point [J/m ²]	G _c (SBT)	G _c (CBT)	G _c (ECM)
Mean propagation	73	80	111
SD of propagation	7	7	9
Mean initiation	81	89	123
SD of initiation	5	6	10
Mean arrest	56	62	83
SD of arrest	3	3	4

Table 4.1: Fracture energy versus crack length for the control epoxy from TDCB specimen

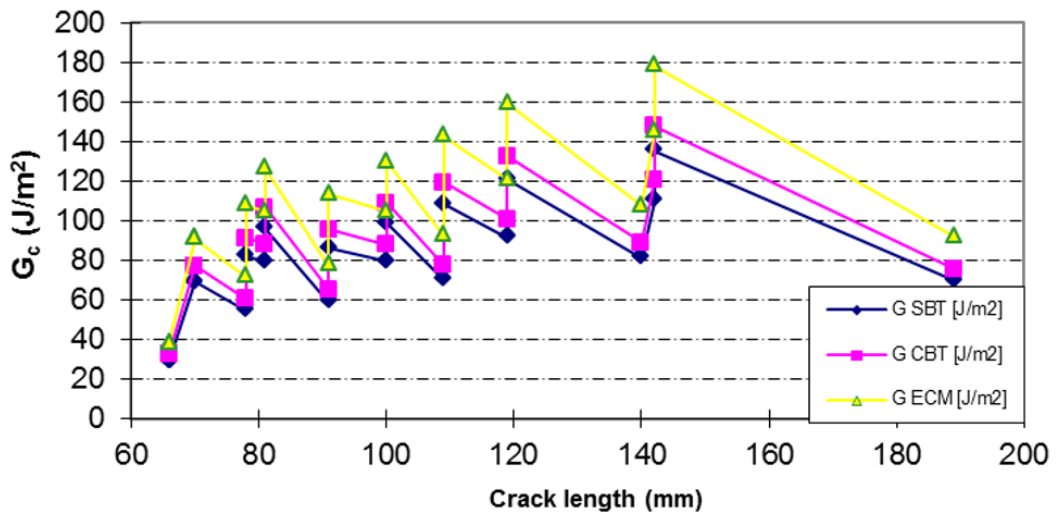


Figure 4.5: Fracture energy versus crack length for the control epoxy from TDCB specimen

Silica-modified epoxy

The addition of silica generally increased the toughness, see Table 2. There was an increasing trend in mean G_c from control to the addition of 2 weight % of silica, but when there was a higher amount of silica added, no pattern was formed and values were a lot lower than expected. There was interfacial failure, and no stick slips, in specimens with 10 and 15 weight % of silica. All the results found were lower than the values from

Hsieh et al. [24]. More about the interfacial fracture surfaces is discussed in the next Section. According to the propagation curve, see Figure 19, there is a peak shown in G_c value with the addition of 2 weight % of silica, the G_c value dropped after this point. This could be due to the presence of greater than 15 % of debonding when a lower % of silica is added. The % of debonding reduces when there is a higher % of silica added, because when particles are more concentrated, they would become too close to each other, so the energy needed for voiding would be higher [4], therefore these results are according to predictions. It is also found by Johnsen et al. [4] that there was a high increase in fracture energy when 13% of silica nanoparticles were added in [4]. However, there were two lower values when 3 % and 15 % of silica particles were used, these drops were not expected, they would be errors and graph is expected to show a clear trend. A plateau is expected after the peak, the relatively high weight % of silica particles would not show significant effects in toughening. At very high weight % of silica particles the toughness will decrease due to there being too little epoxy between the particles to absorb the maximum energy, this occurred to some of the specimens.

Point[J/m ²] / % of SiO ₂	Control	0.5	1	2	3	5	10	15*	20*	25.4
Mean propagation	80	76	129	123	56	113	163	106	91.3	146.5
SD of propagation	7	3	5	9	6	54	2	7	8	13
Mean initiation	89	95	142	158	71	70	N/A	N/A	N/A	N/A
SD of initiation	6	3	5	N/A	9	N/A	N/A	N/A	N/A	N/A
Mean arrest	62	67	87	73	58	64	N/A	N/A	N/A	N/A
SD of arrest	3	5	4	N/A	8	N/A	N/A	N/A	N/A	N/A

* Formulations with interfacial failure

Table 4.2: Summary of fracture energies calculated using the CBT method from TDCB specimens, mean standard deviation

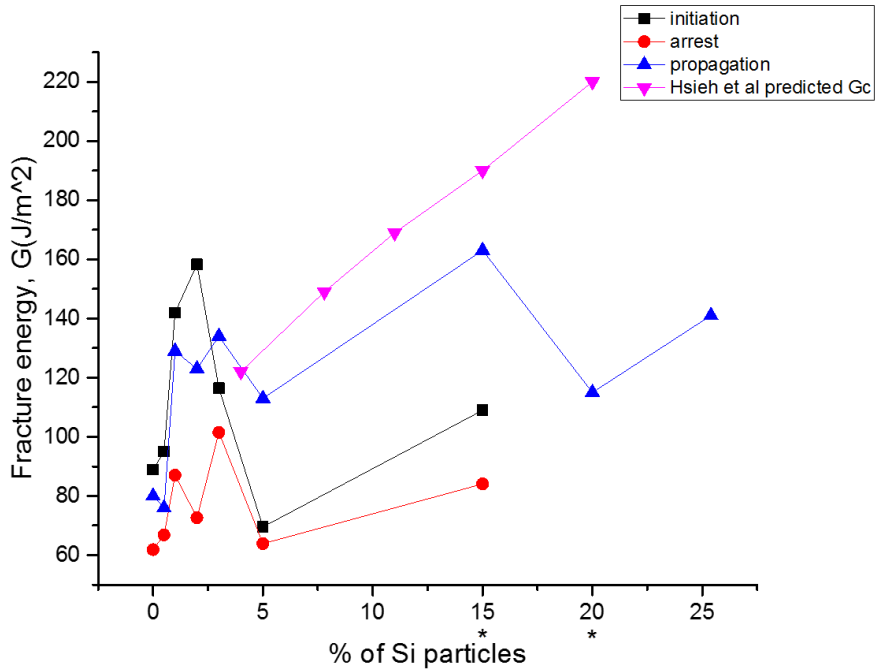


Figure 4.6: Fracture energy against percentage of silica from TDCB specimens (CBT) and model predictions from Hsieh et al. [46] [51]

CSR

It is shown that the fracture energy of the CSR-modified epoxy was about one time higher than the silica-modified epoxy for all weight %. There is a general increase in toughness when the % of particles increases, the small drop in fracture toughness at 2% of CSR might be caused by clustering of particles that couldnt be mixed properly. Most regions of the CSR-modified TDCB beams showed cohesive failure, while some of the silica-modified beams had interfacial failure, which explains why there were remarkably larger G_c values for the CSR specimens. This indicated that the fracture energies of the silica-modified joints were not measured accurately due to the effect of interfacial failure; see Tables 1, 2 and 3 and Figures 17, 18 and 19. The cause of inaccuracy in the silica-modified TDCB specimens can also be due to the viscosity of the resin. Silica-modified epoxy had a low viscosity and some of the resin dropped down from the beams during making of the joints. It caused uneven thickness of the bondline. Hybrid mixture would have a higher viscosity and would be expected to improve accuracy of the measurements.

Point[J/m ²] / % of CSR	0	0.5	1	2	10
Mean propagation	80	121	178.8	218	300
SD of propagation	7	12.6	9	0	126
Mean initiation	88	149	210.6	165	599
SD of initiation	6	15	14	5	284
Mean arrest	62	90.3	155.5	11	182
SD of arrest	3	11	14	13	15

Table 4.3: Summary of fracture energies of CSR modified epoxy calculated using the CBT method from TDCB specimens, mean standard deviation.

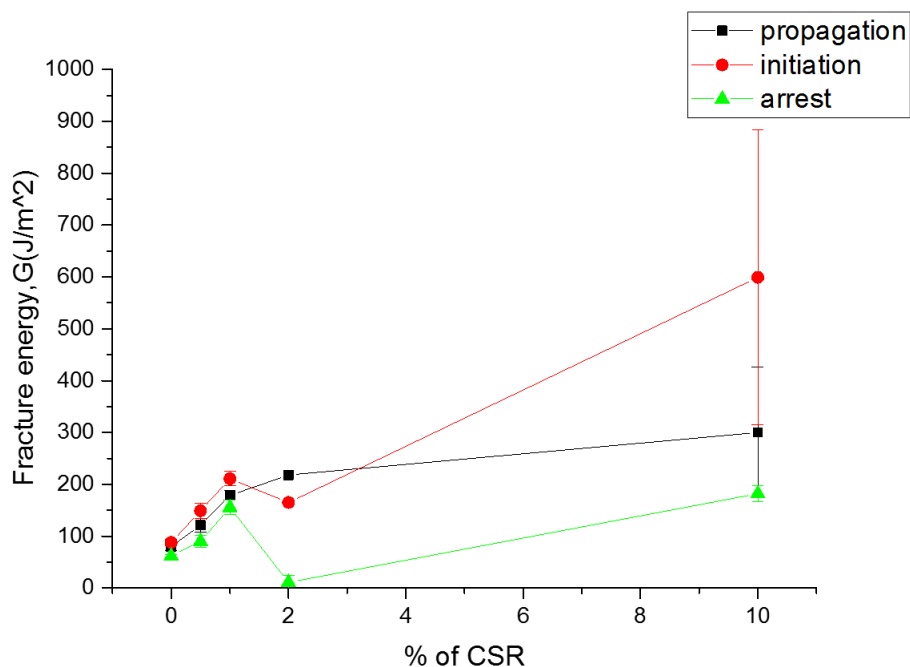


Figure 4.7: Fracture energy against percentage of particles for CSR-modified epoxy from TDCB specimens

4.2.11 Fracture surfaces

There was an increasing amount of interfacial failure found when there is 1 and 2 weight % of silica added in. The amount of interfacial failure was reduced by changing the acid tank for refining the quality of the acid etch treatment. This showed that the surface

treatment of the aluminium alloy highly affects the adhesive bonding and its failure. However, specimens with higher weight % of silica (from 3 weight % onwards) showed mainly interfacial failure with propagation only. It could be due to the differences on the surface of beams used (new and recycled beams), this could cause variations in bonding of joints. Most of the regions in CSR specimens were cohesive failure, so the toughness values were reliable. Figure 21 shows the two failure types (interfacial and cohesive) and indicates the stick-slip region in the specimens.

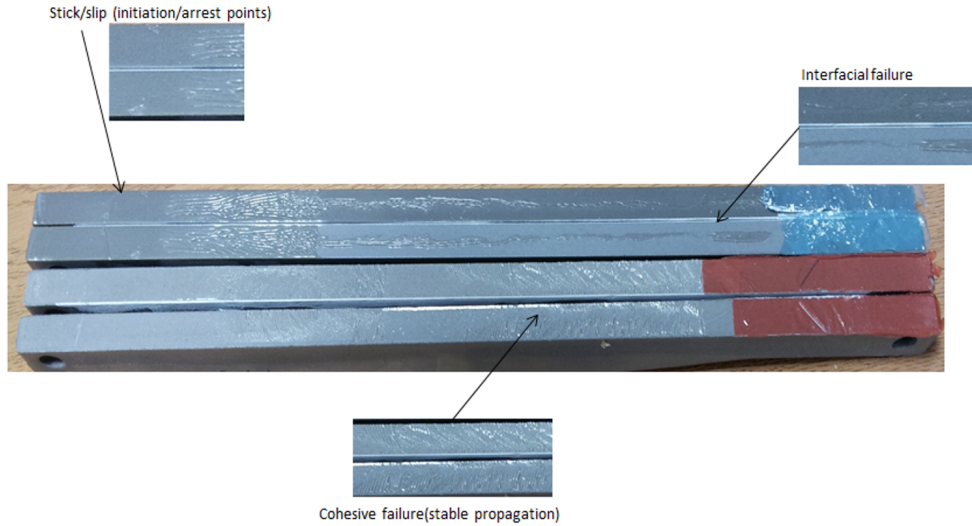


Figure 4.8: Fracture surfaces of TDCB specimens (crack propagation from right to left)

4.3 High rate testing

4.3.1 Introduction

High rate testing was performed with TDCB and SENB samples. The effects of high test rate on the fracture behaviour were investigated, such as if there is any fracture type transition when test rate is increased. SENB high rate results provided additional information to clarify the results found from TDCB tests, as SENB does not have interfacial failure like TDCB. However, TDCB provided information for the propagation of crack, not just initiation as for SENB. After testing, the fracture surfaces were analysed by field emission gun scanning electron microscopy (FEGSEM) (more details in Section 3.2.8), to identify the toughening mechanisms and the percentage of silica nanoparticles which undergo debonding and void growth. The measured fracture energies will be compared with predictions from analytical models, such as those by Hsieh et al. [2, 3].

4.3.2 TDCB high test rate set up

The experimental set up for high rate testing was similar to that at low rate, but instead of a travelling microscope used to measure crack length, a high-speed video camera was used to improve the accuracy of the crack length and displacement measurements. In the test set up, the upper side of the loading shackle was connected to a titanium lost motion device (LMD), which was then attached to the hydraulic ram. A linear variable displacement transformer (LVDT) was used to measure the position, and hence to calculate the velocity, of the hydraulic ram, see Figure 21. The lower side of the loading shackle was the stationary part of the set up; it was connected to a piezo-electric load cell (PCB 221B04, range of 4.48 kN, Sensitivity: 1124.1 mV/kN, rise time of 10 μ s). A Phantom 3.1 high-speed camera (manufactured by Vision Research, New Jersey, USA) was used. High-speed video (HSV) was used to measure the local displacement without significant dynamic oscillations which affect the LVDT, and hence improves accuracy. A lost motion device (see Figure 22) was used for providing an even acceleration during high rate test; it was made up of a titanium rod with an aluminium cup and cone contact unit. The LMD has a movable extension rod, which helps to ensure constant speed before the movement reaches the specimen. The LMD was kept at its minimum weight to reduce inertial effects. Inertial effects were also minimised by attaching the components (load cell to the test specimen and to the stationary loading shackle) together as close as possible. This reduced oscillations caused by stress wave reflections and acceleration during the test. However, there might be bouncing effects and oscillations during the contact of the LMD, therefore rubber washers were used as damping between the surfaces of the cup and cone.

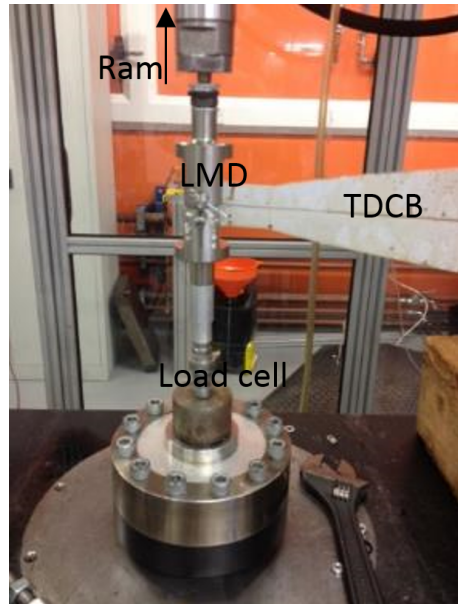


Figure 4.9: TDCB mode I high rate test setup [38]



Figure 4.10: TDCB mode I high rate test setup [38]

For the high speed video (see Figure 23), the high framing rate used would reduce the amount of data that can be stored in the camera, therefore, images were cut to only the area needed, or reduced in image size. Hence different combinations of framing rate and picture resolution were used at different test rates. Hence the frame information was different for each test. The high speed photography was used to measure crack length

to obtain the crack velocity.

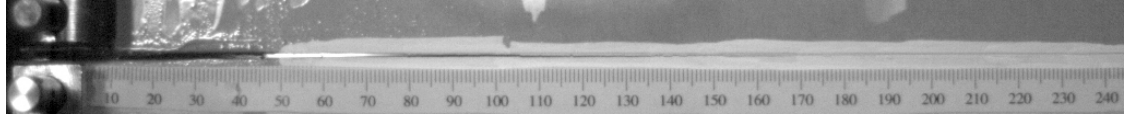


Figure 4.11: Example of high rate TDCB image. Crack propagation was from left to right

In order to see the effect of rate in fracture, test rates of 0.1 m/s, 1 m/s and 10 m/s would be used.

4.4 High rate data reduction strategy

4.4.1 Fracture types

There are four fracture types developed from the data reduction strategy in [53], for the four different types of crack growth:

Type 1: Slow, stable propagation

Type 2: Slow, unstable (stick-slip) propagation

Type 3: Fast, unstable (stick-slip) propagation

Type 4: Fast, stable propagation

There are different analysis methods required for the different types of crack growth, more about their analysis is discussed in part 3 of this section.

4.4.2 Data analysis

Video analysis

Measurements of displacement (from video), crack length (a) and time were taken from selected frames, as shown in Figure 24. Crack length (a): Crack length was measured manually from each of the video images, as there was white ink painted on the specimen, the crack was visible as a black line between the substrates of the adhesive joint. Load point displacement (δ): The displacement was measured manually from each of the video images by recording the distance between the centres of the two pins when compared to their initial positions.

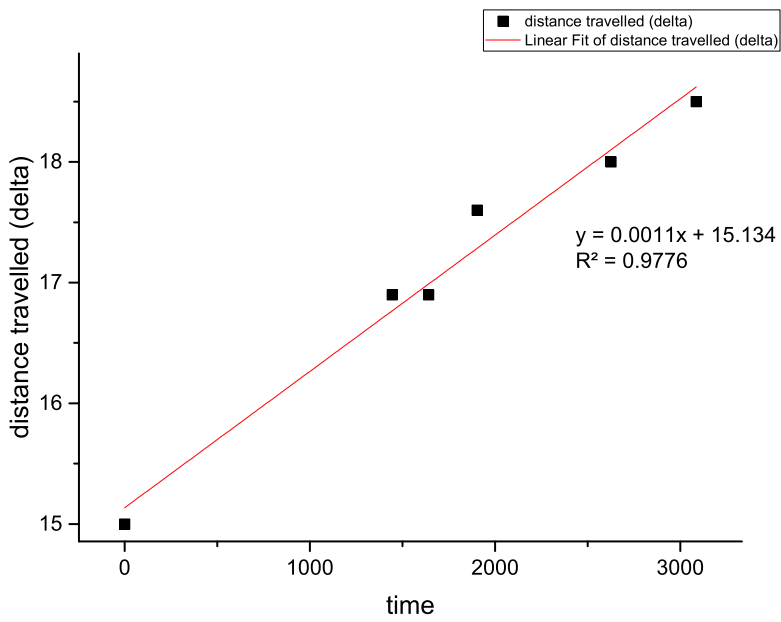


Figure 4.12: Distance between centres of pins against time graph for TDCB specimen

The numbers of pixels in the images were calibrated with the actual displacement in mm from the joint. This was performed by first finding the distance between two selected points within the white ink painted region. Then, by using the pixel information from the camera software settings, the number of pixels within the selected region could be found as a reference for calibration. It is important to use a large distance between the two points used for the calibration, as the error from one pixel would be more significant within a short distance.

Plots

There are three plots used in this method: displacement (between loading pins) against time, load against time and crack length against time (see Figure 25). Load and displacement data would be obtained from the oscilloscope or Imatek system, the Imatek system collates the readings from the machine and the oscilloscope, so that the different sets of data could be linked together, not individual data anymore. Load data at low rate are reliable, but when at high test rate there would be uncertainty in the load values due to dynamic effects (even with rubber washers there to minimise oscillations). Therefore the load values obtained from machine can only be used at low rate, or maybe

at intermediate rates. Instead, displacement and crack length obtained from the video would be used to analyse the fracture. Propagation points and initiation points were plotted separately as they should be analysed separately [38], and the arrest points are not used. When the test rate is high, it is difficult to distinguish between stable and stick-slip propagation. Hence, to distinguish whether the cracks were stable or unstable, linear regression would be performed on the crack versus time data (see Figure 25) to find out whether $R^2 > 0.95$ [52]:

If R^2 is larger than 0.95, the fracture type would be defined as stable, where propagation values would be used to plot the linear regression line. Whether it is type 1 or 4 depends on whether the kinetic energy (KE) was significant. If R^2 is smaller than 0.95, fracture type would be stick-slip fracture, where initiation values would be used to plot the linear regression line. It would be defined as a type 2 or 3 fracture depending on whether the KE was significant.

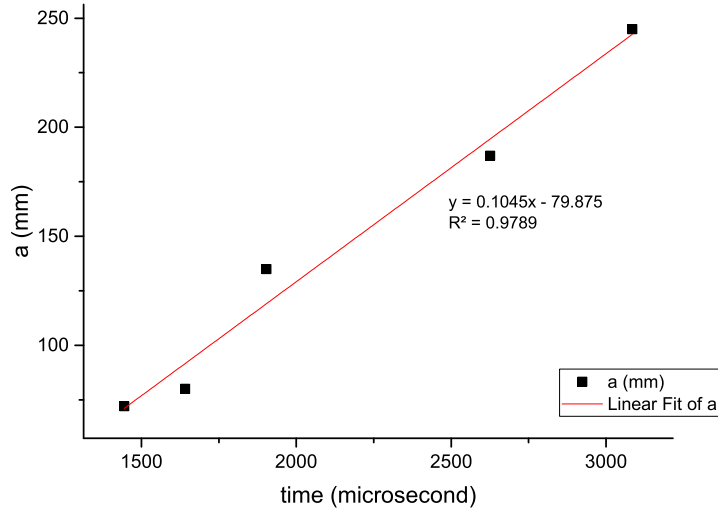


Figure 4.13: Distance between centres of pins against time graph for TDCB specimen

Analysis of G_C values

The values of G_C^s (static value of the adhesive fracture energy) and G_C^d (dynamic value of the adhesive fracture energy) are used to determine if the kinetic energy (KE) was significant. The KE would be considered significant when the fracture energy increases by more than 5% of the quasi-static value due to the increase in test rate, i.e. when:

$$(G_C^S - G_C^d)/G_C^s < 0.05 \quad (4.5)$$

then the KE would be significant, and the fracture would be analysed as type 3 or 4 (depends on whether it is stable or unstable from the crack length against time plot mentioned above). Gdc values would be reported. If

$$(G_C^s - G_C^d)/G_C^s \neq < 0.05 \quad (4.6)$$

then the KE would not be significant, and the fracture would be analysed as type 1 or 2 (depends on if it is stable or unstable from the crack against time plot mentioned above). G_C^s values would be reported. The equations used to calculate G_C^S , G_C^d for the TDCB specimens [57]:

For type 1 (it is a CBT method that uses propagation values):

$$G_C^S = \frac{4P^2m}{EB^2} \left[1 + 0.43 \left(\frac{3}{ma} \right) \right]^{1/3} \quad (4.7)$$

where G_C^S = quasi-static value of the adhesive fracture energy, P = load, E = Youngs modulus of substrate, B = width of test specimen, a = crack length and m = specimen geometry factor ($m = 2 \text{ mm}^{-1}$ for TDCB specimens):

$$m = \frac{3a^2}{h^3} + \frac{1}{h} \quad (4.8)$$

where h = height of specimen substrate

For type 2 (it is a CBT method that uses initiation values):

$$G_C^S = \frac{4P^2}{EB^2} \left[1 + 0.43 \left(\frac{3}{ma} \right)^{1/3} \right] \quad (4.9)$$

For type 3 (only uses crack initiation values):

$$G_C^S = \frac{E}{4m} \left[\frac{\delta}{2a} \right]^2 \left[1 + 0.43 \left(\frac{3}{ma} \right) \right]^{1/3} \left[1 - 3 \frac{9}{22}^3 \left(\frac{a^*}{c_L^t} \right)^2 mh(a^*) \right] \quad (4.10)$$

where δ = displacement between pins, t = time, a = crack length and CL = longitudinal wave speed:

$$C_L = \frac{\sqrt{E}}{\rho_s} \quad (4.11)$$

where E = modulus of substrate and s = density of substrate. For the aluminium alloy substrates used, these values are 70 x 109 Pa and 2700 kg/m³ respectively. For type 4 (only uses crack propagation values):

$$G_C^d = \frac{E}{4m} \left[\frac{\delta}{2\dot{a}^*} \right] \left[1 + [0.43 \left(\frac{3}{ma} \right)]^{1/3} \left[1 - 3 \frac{9}{22} \frac{{a^*}^2}{c_L t} mh(a^*) \right] \right] \quad (4.12)$$

where V = crack velocity (found using the distance between centres of pins and time from video). The equation used to find out the dynamically-corrected value of G_C (G_C^d) of TDCB specimens is:

$$G_C^S = \left[\frac{(V/2)}{a} \right]^2 \left[1 + 0.43 \left(\frac{3}{ma} \right)^{1/3} \right]^{-1} \quad (4.13)$$

where V = crack velocity (found using the distance between centres of pins and time from video). The equation used to find out the dynamically-corrected value of G_C (G_C^d) of TDCB specimens is:

$$G_C^d = \frac{E}{4m} \left[\frac{\delta}{2a^*} \right] \left[1 + 0.43 \left(\frac{3}{ma} \right)^{1/3} \right] \left[1 - 3 \left(\frac{9}{22} \right)^3 \left[\frac{{a^*}^2}{c_L t} \right]^2 mh(a^*) \right] \quad (4.14)$$

where $h(a^*)$ = height of beam at a distance a^* from load line, where a^* is the crack at a specific height, and is given by

$$a^* = a + 0.64 \left(\frac{3a^2}{m} \right)^{1/3} - \frac{2}{3}x_0 \quad (4.15)$$

where for TDCB specimens the initial crack length $x_{(0)} = 50mm$

Note that the type 3 G_S^C equation = G_d^C equation, because type 3 only uses crack initiation values as it is for a fast-rate unstable crack. Trials of the high rate set up have been ongoing and tests are expected to run smoothly once all the connections of equipment are ready. Trials with CSR 2 weight Three specimens from each of the selected formulations would be used each test rate (0.1, 1 and 10 m/s), these rates of tests would provide insights into the effect of the rate of testing on the fracture behaviours.

4.4.3 High rate TDCB results

Due to the limitations with the number of frames used, results can only be analysed when rate used was not higher than 3ms^{-1} . Test rate of 1,2 and 3ms^{-1} were preformed. Average fracture energy values were used, as the crack points found were assumed to be propagations in this method.

R were found to be smaller than 0.95, so they were stable crack with type 1 or type 4. As all the data were analysed using the video, they are considered as type 4.

Figures below shown average fracture energy when tests were performed under 1ms^{-1} , 2ms^{-1} and 3m^{-1} .

Hybrid specimens shown slightly higher fracture values for all 3 rate used, While Silica and CSR specimens shown very similar results. The higher % of particles didn't always produce a higher fracture value. 5 % was found to be the optimum in most of the results. Similar pattern is found in 1ms^{-1} specimens, all 3 particles produced the same pattern. There was an increasing trend in Silica under 2ms^{-1} , while the other 2 particles shown higher fracture values in 5 wt%. CSR specimens shown significantly lower values under 3ms^{-1} , and the other 2 specimens had almost the same behaviour. However, as there were less points available when rate is higher, results from 3m^{-1} were not as reliable.

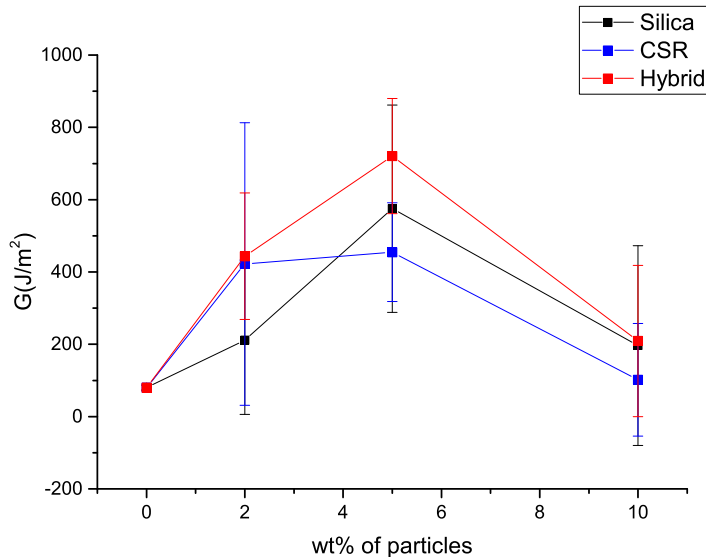


Figure 4.14: Average fracture energy figure when rate is 1ms^{-1}

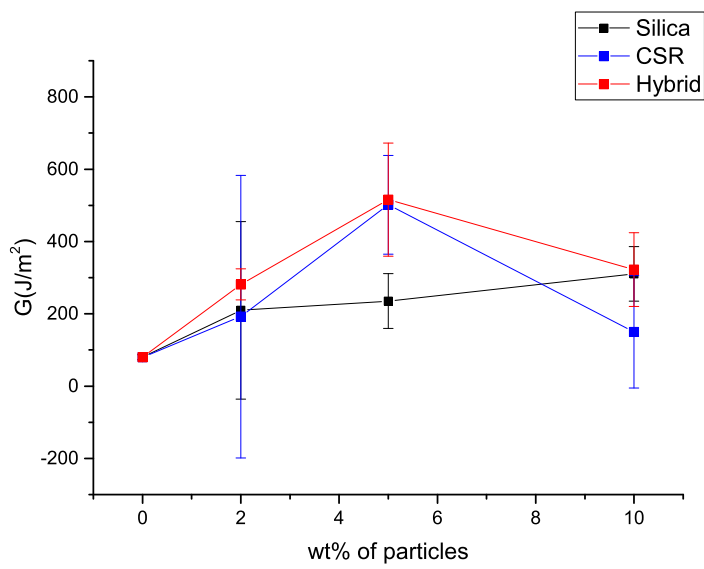


Figure 4.15: Average fracture energy figure when rate is 2ms^{-1}

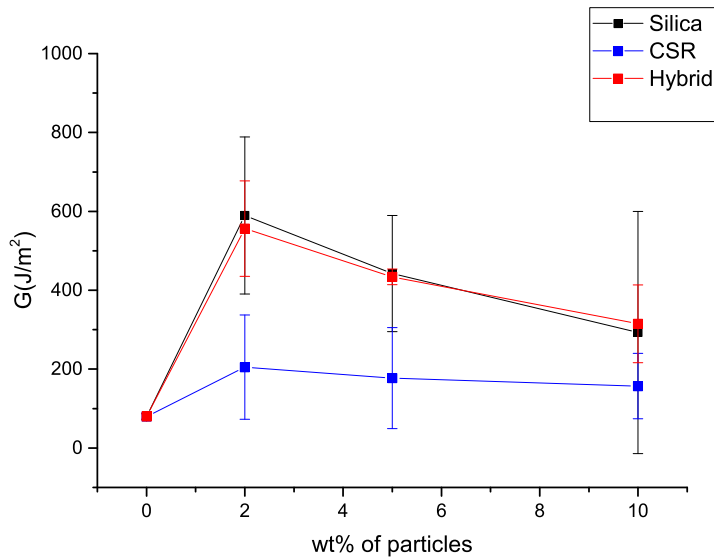


Figure 4.16: Average fracture energy figure when rate is 3ms^{-1}

4.5 Tensile testing

4.5.1 Introduction

Tensile tests on bulk samples provided the Youngs modulus, E, of the materials for the calculations of fracture toughness or critical stress intensity at the crack tip, Kc, and fracture energy, Gc, when using the linear elastic fracture mechanics (LEFM) method in the SENB test. The Youngs modulus value was found using the linear portion of the stress-strain curves. The results calculated also included values such as true yield strength and true yield strain. The tensile true stress, σ_t , was found using:

$$\sigma_t = \sigma_E(1 + \varepsilon_E) \quad (4.16)$$

Tensile true strain, ε , was found by:

$$\varepsilon_t = In(\varepsilon_E + 1) \quad (4.17)$$

Tensile tests were performed using specimens with type 1BA geometry (see Figure 26) according to ISO standard 527 [62].

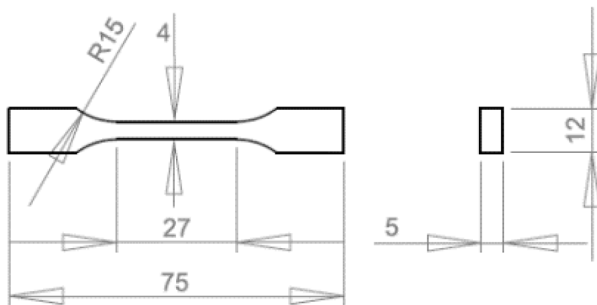


Figure 4.17: Tensile test geometry (dimensions in millimetres) [59]

The tests were performed at a test rate of 1 mm/min. Six specimens were tested for each set. An Instron 2620-601 dynamic extensometer was attached to the specimen to measure the extension for providing accurate strain values. The tensile test results were assumed not to be significantly affected by rate for the calculation of LEFM values. The mean and the standard deviation of the Youngs modulus are reported.

4.5.2 Results

The tensile modulus results are shown in Figure 27 and Table 4 below. Similar values of Youngs modulus were found in all specimens, most of the specimens have a modulus

of about 3 GPa, and within an acceptable range of standard deviations. The modulus generally increased with the increased amount of particles added in. However, there is a significant reduction in modulus value at CSR 10%, the optimum % of CSR particles used was 5%. Therefore, although most of the tests in this study have shown that the CSR-modified specimens had greater mechanical properties when compare to the silica ones, max% of silica had the highest modulus value. It is expected that the use of hybrid particles would provide a higher modulus when compare to using one particle only, but hybrid particles had not shown significant improvements in their tensile properties, which might due to particles clustering.

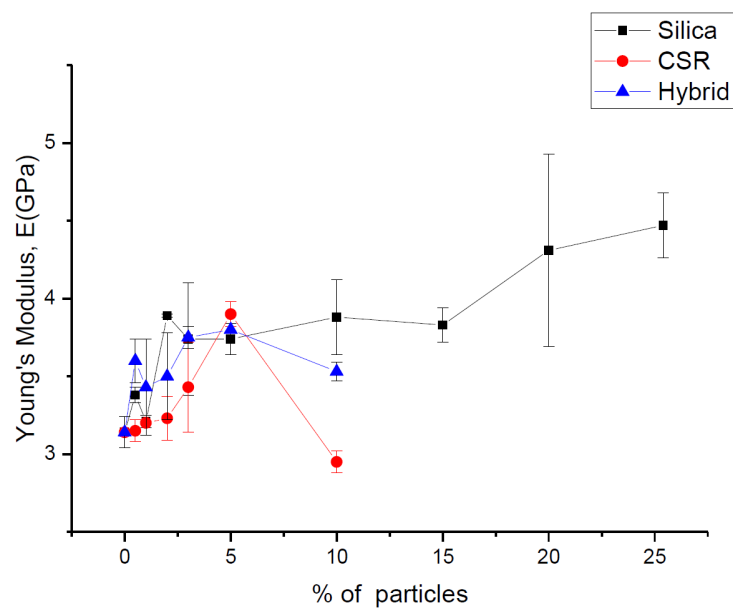


Figure 4.18: Tensile modulus results of nanoparticle-modified epoxy

Table 4.4: Tensile test results of nanoparticle-modified epoxy

particles	Silica		CSR		Hybrid	
% of particles	Young's Modulus (GPa)	SD	Young's Modulus (GPa)	SD	Young's Modulus (GPa)	SD
0	3.14	0.10	3.14	0.10	3.14	0.10
0.5	3.38	0.05	3.15	0.07	3.60	0.14
1	3.21	0.04	3.20	0.00	3.43	0.31
2	3.89	0.01	3.23	0.14	3.50	0.28
3	3.74	0.36	3.43	0.29	3.75	0.07
5	3.74	0.10	3.90	0.08	3.80	0.00
10	3.88	0.24	2.95	0.07	3.53	0.06
15	3.83	0.11				
20	4.31	0.62				
25.4	4.47	0.21				

4.6 Single-edge notch bending (SENB) tests

4.6.1 Introduction

Single-edge notch bending (SENB) tests were used to find the fracture toughness, K_c and fracture energy, G_c . These values were compared with the results from TDCB test results. In order to provide further understanding of the toughening mechanisms of the epoxy, fracture surfaces would be examined under FEG-SEM and compare with the fracture surfaces found from TDCB. The particle contents used are presented in Table 5 below.

Table 4.5: Particle content used in SENB specimens

Silica	CSR	Hybrid	
% of Silica particles	% of CSR particles	% of Silica particles	% of CSR particles
0	0	0	0
0.5	0.5	0.5	0.5
1	1	1	1
2	2	2	2
3	3	3	3
5	5	5	5
10	10	10	10
15			
20			
25.4			

SENB specimen preparation

SENB specimens were made from 6 mm thick cast plates. To cast the plates, first the steel moulds were cleaned. Pieces of residual epoxy were cleaned off the mould using a razor blade. The moulds were then wiped with acetone and release agent (Frekote 700-NC, Henkel, UK) was coated on the surfaces. The moulds were clamped firmly and preheated to 60 °C in a fan oven before the epoxy resin was poured in. The epoxy resin, modifiers and hardener were stirred with an overhead mixer at 90 rpm and degassed at 60 °C. The curing cycle used was: Starting temperature at 60 °C, ramp at 1 °C/min to 95 °C, dwell for 1 hours, ramp at 1 °C /min to 165 °C for and dwell for 2 hours, ramp 2 °/min to room temperature (20 °C). Two bulk plates were made for each formulation, and specimens were cut and polished into SENB specimens of 6 mm thick, 12 mm in width and 60 mm in length according to the ISO 13586 standard [39]. Six specimens were made for each formulation for low rate testing, and three specimens for high rate testing. For each specimen, a 4 mm notch was machined and a natural crack was made by tapping the notch with a liquid nitrogen-chilled razor blade. The cracks produced need to be at least four times the length of the notch tip radius. Tests would be rejected if crack length is 10% more than 6 mm. The specimen (see Figure 28) dimensions are

specified to ensure plane strain conditions. The criteria are indicated below according to the standard [39]:

thickness, $h > 2.5r$

crack length, $a > 2.5r$

ligament width, $(w - a) > 2.5r$

where $r = K_C^2 / \sigma_y^2$

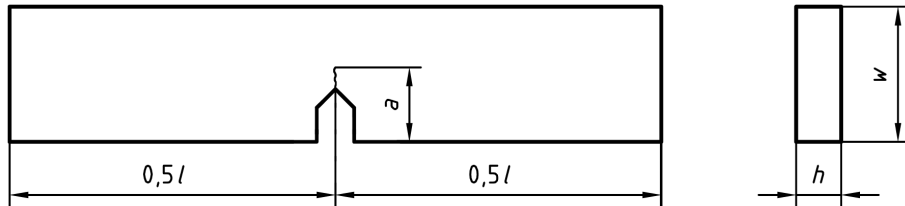


Figure 4.19: SENB specimen geometry according to standard [39], where w is width, l is overall length, h is thickness and a is crack length.

4.6.2 Testing

Quasi-static SENB tests

SENB tests were performed at a constant displacement rate of 10 mm/min using an Instron 3369 universal testing machine. The setup is shown in Figure 29, and an extensometer is not needed to measure the displacement as only the maximum load (not the energy method) is used.



Figure 4.20: SENB specimen geometry according to standard [39], where w is width, l is overall length, h is thickness and a is crack length.

High rate SENB tests

High rate SENB tests (see Figure 31) were performed with the same high rate Instron as used for the high rate TDCB tests, using a piezoelectric loadcell type PCB 208 A03, which has a sensitivity of 10.19 mV/lb (or 10.10 mv/4.482 N). The test rates used initially were 0.1 ms^{-1} and 1 ms^{-1} , with 100 mm of travel (80 mm for acceleration before hitting the sample and 20 mm for deceleration). At high test rates, damping is often required to reduce the dynamic effects to ensure that the measured load is reliable; either grease or Blu-tak is typically used. The Standard specifies that these oscillations must be within $\pm 5\%$ of the maximum load when the load is above half of the maximum value (see Figure 30). There was no need to apply grease at the rate of 0.1 ms^{-1} as the data showed that dynamic effects were within the $\pm 5\%$ region. A layer of 0.05 mm thick Blu-tak is applied as damping at a rate of 1 ms^{-1} , this damping was sufficient for test rates up to and including 1 ms^{-1} .

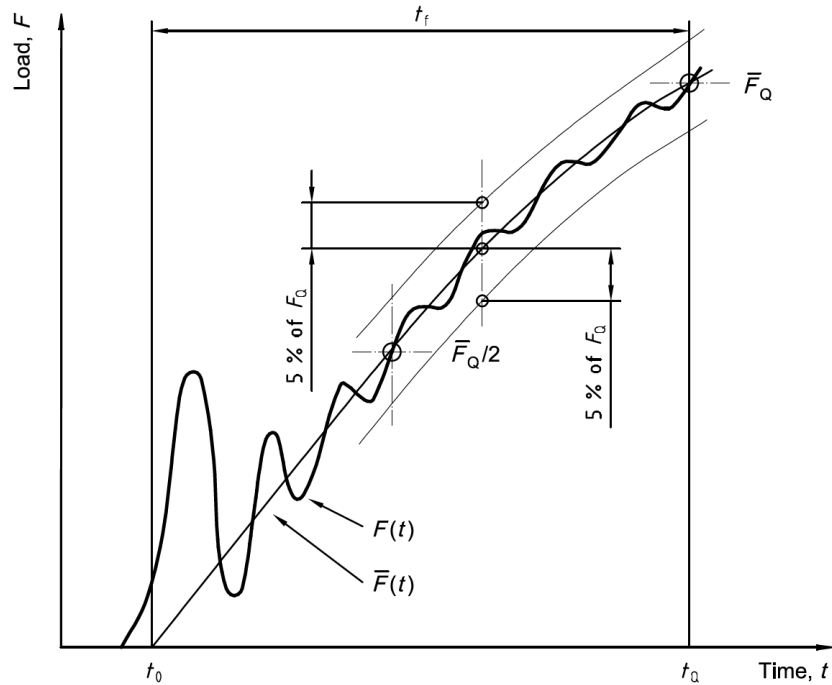


Figure 4.21: Force fluctuations in fracture tests [63]

When the rate was greater than 1 ms^{-1} , such as at 5 ms^{-1} , there were a large amount of oscillations even with significant damping applied to the specimen (Blu-tak of 0.1 mm thickness). Therefore, test results from rate higher than 1 ms^{-1} were not reliable. To improve the reliability of the results, investigations on using the displacement method

rather than the load (focus on the displacement only by the use of high-speed camera) or testing specimens under lower temperature will be performed (more about the method is described in Section 9).



Figure 4.22: High rate SENB test setup

4.6.3 Results

Quasi static test rate SENB tests

For the control epoxy a fracture energy of $G_C = 68J/m^2$ was measured. The fracture energy values of the silica-modified specimens were found to be significantly larger than the CSR-modified ones, which did not agree with the quasi-static TDCB results. As expected, there was an increasing trend of toughness when the % of particles added is increased. The addition of particles highly increased the mechanical properties of epoxy. This is especially significant in silica-modified specimens, there was a 1 time increase in fracture toughness when the % of silica added was the maximum of 25.4 weight % (see Figure 32 and Table 6). There was also a notable plateau when the % of CSR particles added was high, above 5% of CSR. The hybrid showed intermediate results. The quasi static test rate results are compared to high test rate results in the following section.

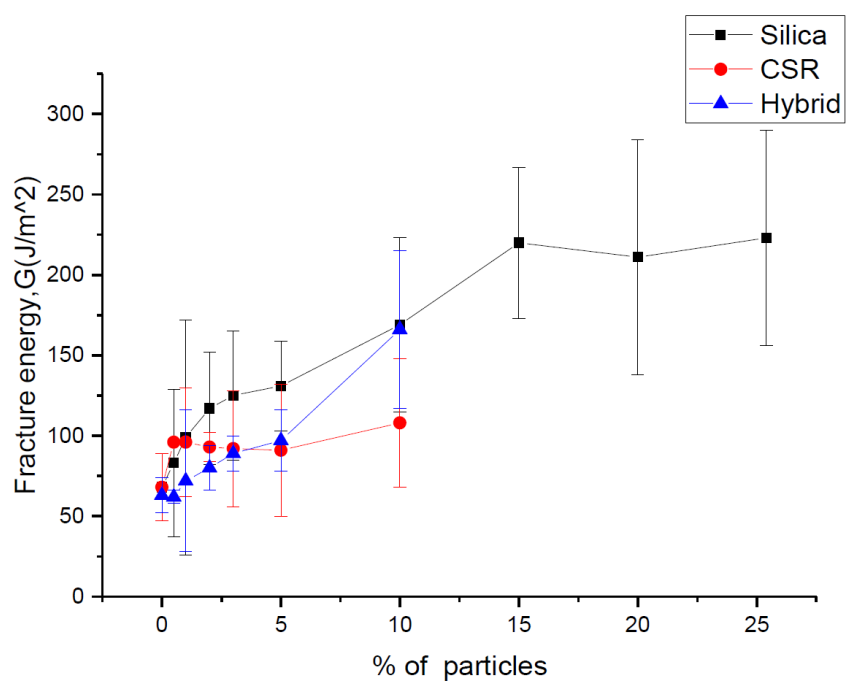


Figure 4.23: Fracture energy of modified epoxy under quasi static test rate

Table 4.6: Fracture energy of modified epoxy under quasi static test rate

particles Wt % of particles	Silica		CSR		Hybrid	
	G _c (J/m ²)	SD	G _c (J/m ²)	SD	G _c (J/m ²)	SD
0	68	21	68	21	63	11
0.5	83	46	96	1	62	4
1	99	73	96	34	72	44
2	117	35	93	9	80	14
3	125	40	92	36	89	11
5	131	28	91	41	97	19
10	169	54	108	40	166	49
15	220	47				
20	211	73				
25.4	223	67				

High rate SENB

Silica-modified epoxy

Figure 33 and Table 7 show the fracture energy for SENB specimens of silica-modified epoxy tested under different rates. There were some significant increases in the toughness for all % of silica when the rate of test was increased. Tests under quasi-static rate and 1 m/s showed similar results, the toughness values were not affected when the rate was relatively low. The highest values at 1 m/s were for 15 weight % of silica, which might be due the fact that the higher % of particles added increased the energy needed for debonding and shear mechanisms, and hence could not increase the amount of fracture mechanisms there, 14.3% was the highest % of debonding found among similar studies [29] at quasi-static rates.

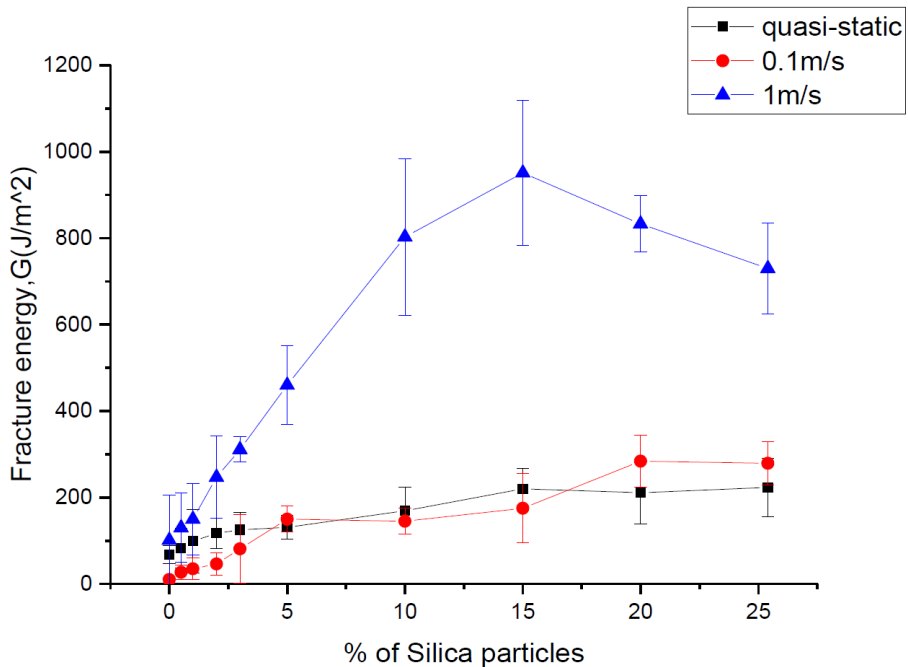


Figure 4.24: Fracture energy of silica-modified epoxy at different rate

Table 4.7: Fracture energy of silica-modified epoxy at different rate

Rate	quasi-static		0.1 m/s		1 m/s	
	Wt% of Silica particles	G _c (J/m ²)	SD	G _c (J/m ²)	SD	G _c (J/m ²)
0	68	21	10	0	101	105
0.5	83	46	27	17	130	80
1	99	73	35	25	150	83
2	117	35	46	26	247	95
3	125	40	81	80	311	29
5	131	28	150	30	460	91
10	169	54	145	30	803	181
15	220	47	175	80	951	168
20	211	73	284	60	833	65
25.4	223	67	279	50	730	105

CSR-modified epoxy

Figure 34 and Table 8 show the fracture energy for SENB specimens of CSR modified epoxy tested under different rates. The CSR specimens tested under high test rate had very high fracture energy values when compare to quasi-static ones. The increases

in toughness were particularly significant when the % of CSR was high, however the standard deviations were higher as well, this was believed to be due to the very unstable fracture causes higher variations in results. Therefore, the values from 5% onwards were considered to be unreliable as there were significant increases found, and the increase is likely to be due to the dynamic effects. As large standard deviations (1500J/m^2) in fracture energy were found at 1m/s , the results were not reliable, therefore low temperature SENB tests were used to provide clarifications to the high test rate results.

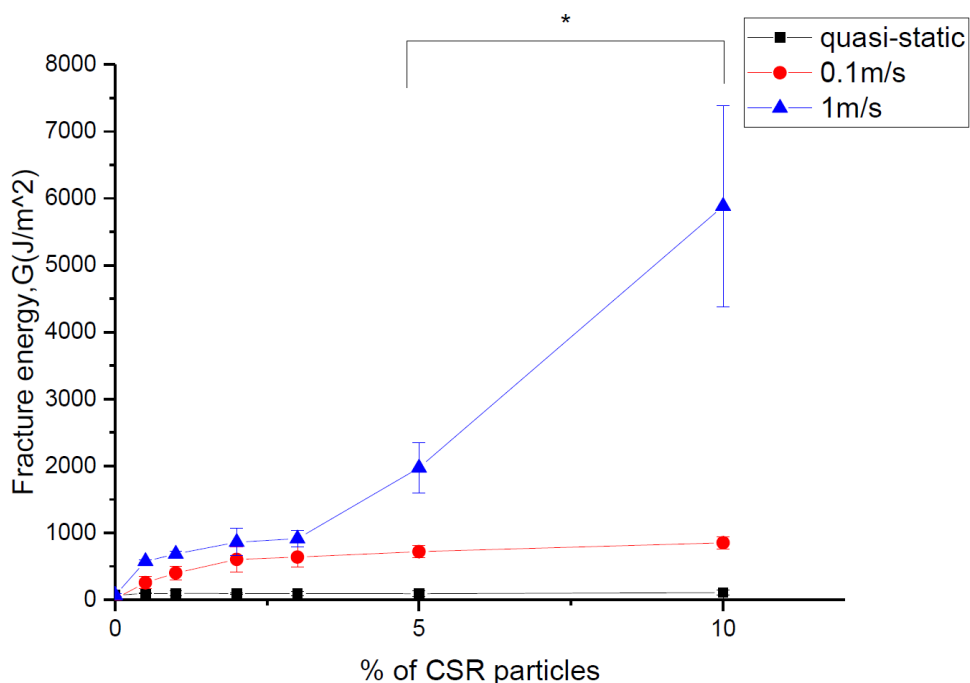


Figure 4.25: Fracture energy of CSR-modified epoxy at different rate
 * Dynamic effects are significant and hence the data are unreliable

Table 4.8: Fracture energy of CSR-modified epoxy at different rate

Rate	quasi-static		0.1 m/s		1 m/s	
Wt % of CSR particles	G_c (J/m ²)	SD	G_c (J/m ²)	SD	G_c (J/m ²)	SD
0	68	21	13	2	67	21
0.5	96	1	257	94	576	21
1	96	34	401	100	685	46
2	93	9	602	188	862	206
3	92	36	638	150	912	123
5	91	41	720	90	1972	380
10	108	40	852	90	5883	1500

Hybrid-modified epoxy

Figure 35 and Table 9 show the fracture energy for SENB specimens of hybrid-modified epoxy tested under different rates. There was an increase in fracture properties when both the % of hybrid particles increased and the test rate increased. However, large standard deviations were also found when 10 weight % of particles were added. There were very large fracture energy values found when the rate is at 1m/s (the highest rate), the large values with the large standard deviations could be not be considered as reliable. These higher variations were due to the increase in oscillations in data that affected the accuracy of results as the dynamic effects were significant. The dynamic effects are significant when the rate is at 1m/s and hence those data are unreliable.

Hybrid-modified specimens showed higher fracture properties when compared to the CSR and silica specimens. It is due to the different particle sizes which increased the plastic zone size and the amount of plastic deformation. There could be a higher shear when rubber cavitation occurs. The synergy effect was more remarkable when the rate was higher, so this effect is expected to be significant when specimens were tested under low temperature, as low temperature has a similar effect to high test rate. The significance of the synergy effect would be revealed further under low temperature testing.

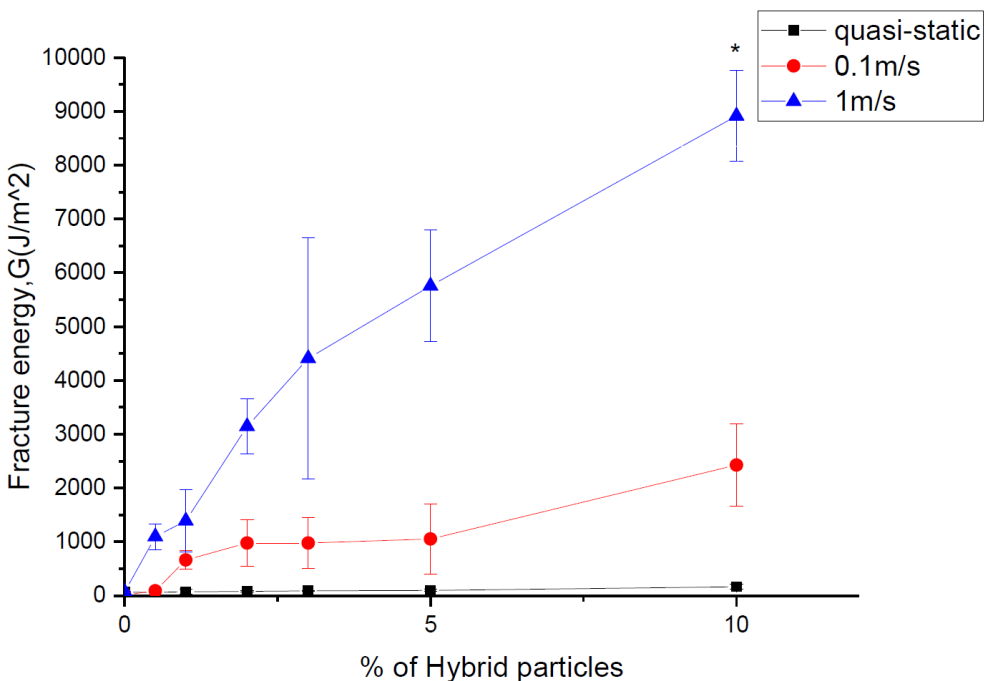


Figure 4.26: Fracture energy of Hybrid-modified epoxy at different rate
 * Dynamic effects are significant and hence the data are unreliable

Table 4.9: Fracture energy of Hybrid-modified epoxy at different rate

Rate	quasi-static		0.1m/s		1m/s	
	Wt % of hybrid particles	G (J/m^2)	SD	G (J/m^2)	SD	G (J/m^2)
0	63	11	13	4	67	21
0.5	62	4	91	5	1096	239
1	72	44	664	170	1392	573
2	80	14	977	436	3146	515
3	89	11	977	477	4409	2239
5	97	19	1054	653	5757	1038
10	166	49	2428	760	8918	847

4.6.4 Quasi-static fracture energy (from TDCB and SENB)

Silica-modified epoxy

Figure 36 compares the fracture energy found from both SENB and TDCB silica-modified specimens. The fracture energy values found from SENB from all % were higher than all the TDCB values, this is due to the interfacial failure in the TDCB tests. The fracture energy values found from the SENB tests were very close to the model predictions, these are more reliable values when compared to those found from TDCB. However due to the differences in nature of the propagation points and the stick-slip points found in TDCB, direct comparisons were not applicable.

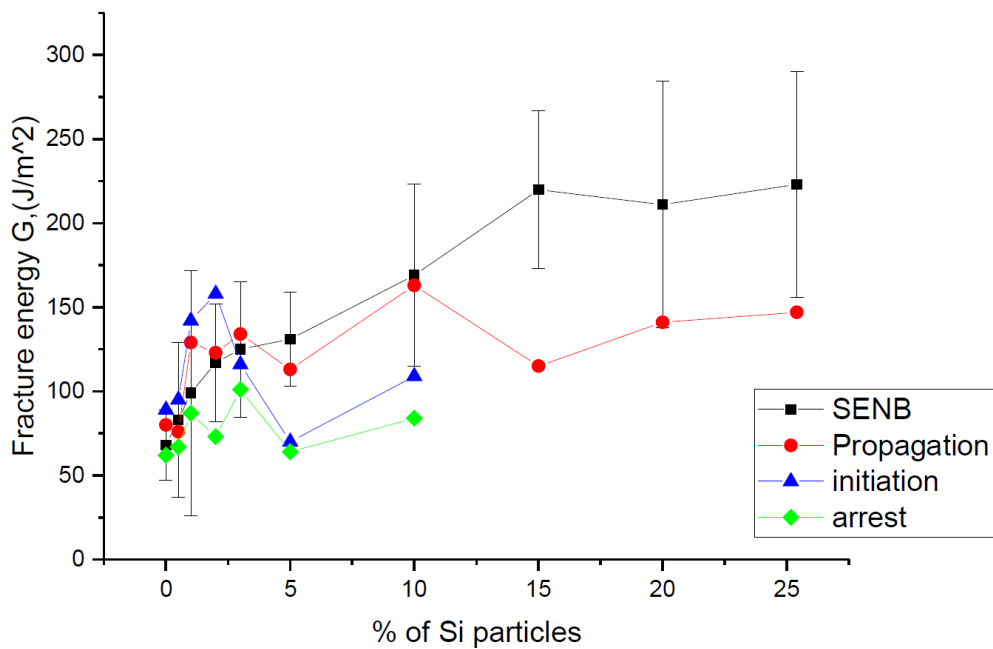


Figure 4.27: Fracture energy of silica-modified epoxy (SENB, TDCB)

CSR-modified epoxy

Figures 37 and 38 compare the fracture energy found from both SENB and TDCB tests on CSR-modified specimens. Fracture energies from TDCB tests were found larger than those found from SENB, as the model predictions were lower than TDCB experimental values, it is suggested that the TDCB joints were performing better due to the presence of stick-slip and cohesive failure. This concluded that TDCB joints performance can be

slightly varied and highly affected by the conditions of testing and preparations. The greater mechanical performance when the % of particles increased can also due to the increase in viscosity of the mixture. When % of particles added in were low, very low viscosity mixture were produced and epoxy run down from the joint easily. This did not happen when the % of CSR added in were high, therefore caused variations in results.

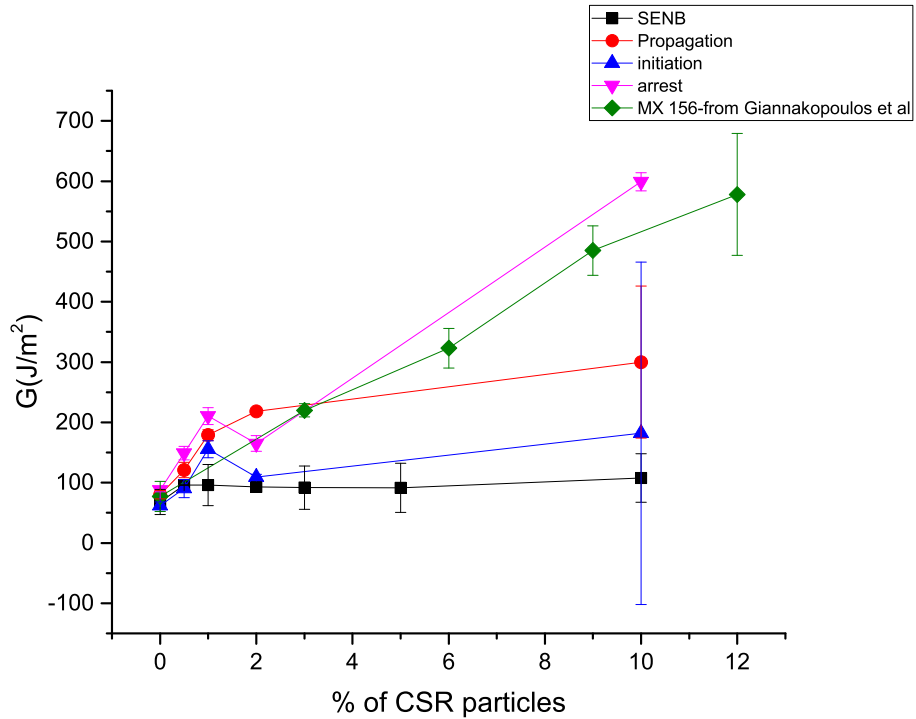


Figure 4.28: Fracture energy of quasi-static CSR (SENB, TDCB) and CSR-MX-156

The fracture energy values of CSR were also compared with the CSR study from Giannakopoulos et al. [64], as the epoxy and hardener used were the same, this would provide a good comparison for the performance of the CSR used. MX 156 from Giannakopoulos et al. [64] was chosen to compare with the CSR used. This is a smaller size of CSR, but Giannakopoulos et al. had shown no effect of particle size. It was found that the fracture energy in MX 156 was higher than Paraloid EXL-2300G for all %. There was a clear improvement in fracture properties when the % of MX 156 added in was increased, while this improvement was not obvious in Paraloid EXL-2300G. However, some large standard deviations values were also present in the MX 156 data, hence some of the values may not be as reliable. The fracture energy values of MX 156 was generated from SENB tests, therefore SENB results were compared here, but the frac-

ture energies found from TDCB were significantly higher than those from SENB, and the initiation values were very similar to MX 156, but slightly higher. To conclude, the fracture energy values from the SENB tests generally showed a more stable increase among all % of particles, and due to the presence of stick-slips, it is not possible to compare these fracture energy values with non-stick-slip situations. However, these data were also compared with the model predictions, and hence, correct estimations of fracture energy values were possible. In terms of the two particles, the silica nanoparticles have a size smaller than the plastic zone size and the crack opening displacement, therefore there would be debonding and void growth. A higher % of void growth expected when a small % of them is added. The micro-size rubber particles toughen the epoxy by shear yielding and this caused larger deformation zones and absorbed strain energy [65]. Rubber particles that cavitated at a relatively lower stress caused localised shear yielding (cavitation will occur before shear banding), followed by plastic void growth. For silica-modified epoxy, the SENB results were more reliable and therefore can reflect the performance of the material, while in CSR-modified epoxy, TDCB shows the possible higher mechanical performance that the material can perform but it would highly depend on the condition of the joints. Consequently, in most of the cases, the fracture energy values would lie in-between the values found in TDCB and SENB.

4.7 Analytical models

Analytical models were used to predict the modulus and fracture properties of the modified epoxies. Common analytical models for the modulus are such as the Nielsen [2] and Halpin-Tsai [2] models. For the fracture energy, the Huang and Kinloch model has commonly been used [2, 24, 66].

4.7.1 Halpin-Tsai model

In the Halpin-Tsai model, the particles are assumed to be well-bonded to the matrix and homogenously dispersed in the epoxy [40]. The Halpin-Tsai model predicts the modulus (E) of a material with particles, and the equations are shown below [2, 24, 66]:

$$E = \frac{(1 + \xi \eta v_f)}{(1 - \eta v_f)} E_u \quad (4.18)$$

where E_u = Youngs modulus of the matrix, v_f = volume fraction of particles and ξ = shape or geometry factor, which is equal to $2w/t$ (where w = particle length and t = particle thickness) and can be expressed as:

$$\eta = \frac{E_p}{E_u} - 1/\frac{E_p}{E_u} + \xi \quad (4.19)$$

where E_p = modulus of particles and E_u = modulus of unmodified epoxy. The E used for the unmodified epoxy = 3.14 GPa, as measured in the present work. The E values used for the CSR and hybrid-modified epoxy are shown in Table 10 below.

Table 4.10: Modulus used for CSR and hybrid modified epoxy

Particles	CSR	Hybrid
% of particles	Young's Modulus (GPa)	Young's Modulus (GPa)
0	3.14	3.14
0.5	3.15	3.17
1	3.20	3.19
2	3.23	3.23
3	3.43	3.28
5	3.90	3.38
10	2.95	3.64

4.7.2 Huang & Kinloch fracture model

The fracture energy (G_C) model from Huang and Kinloch [8, 48, 66] can be used to find the toughening contribution of the particles:

$$G_c = G_u + \psi \quad (4.20)$$

where G_u = fracture energy of unmodified epoxy and ψ = overall toughening contributions of the particle phase. This is generally $G_s + G_v$, where G_s represents the increase in fracture energy due to shear-banding, G_v represents plastic void-growth and G_{db} represents the debonding (or cavitation) of particles. Hence:

$$\psi = \Delta_s + \Delta G_{db} + \Delta G_v \quad (4.21)$$

Debonding occurs for hard particles while cavitation occurs for soft particles [2, 24, 66], but both processes create a void which is then able to grow. Debonding or cavitation

do not contribute significantly to the energy absorption [2, 24, 66] and hence can be ignored. Therefore:

$$\psi = \Delta G_s + \Delta G_v \quad (4.22)$$

The contributions of shear band yielding and void growth can be represented in the equations [2, 24, 66] below.

4.7.3 Shear band yielding

The energy contribution of shear band yielding (ΔG_s) is derived by:

$$\Delta G_s = 0.5v_f\sigma_{ycu}\gamma_{fu}F'r_y \quad (4.23)$$

where vf = volume fraction of particles, ycu = yield stress, fu = failure strain of unmodified polymer (measured from plane-strain compression tests) and

$$F'(r_y) = r_y \left[\left(\frac{4\pi}{3v_f} \right)^{1/3} \left(1 - \frac{r_p}{r_y} \right)^3 - \frac{40}{35} \left(\frac{r_p}{r_y} - 1 \right)^{3/2} \left(\frac{r_p}{r_y} \right) \left(\frac{7}{5} - \frac{r_p}{r_y} \right) - 2 \left(1 - \frac{r_p}{r_y} \right)^2 + \frac{16}{35} \right] \quad (4.24)$$

where rp = radius of particles and

$$r_y = K_{sp}^2 \left(1 + \frac{m}{3} \right) r_{pzu} \quad (4.25)$$

where K_{sp} = maximum stress concentration around a particle, m = 0.2 is a material constant, and r_{pzu} = radius of plastic deformation zone of unmodified epoxy, as discussed below. The value of K_{sp} is a function of the volume fraction of particles (vf) and can be expressed as:

$$K_{sp} = 0.59v_f + 1.65 \quad (4.26)$$

Plastic void growth

The energy contribution from plastic void growth (ΔG_v) can be expressed as:

$$\Delta G_v = \left(\frac{1 - \mu_m^2}{3} \right) (v_{fv} - v_{fp}) \sigma_{ycu} r_{pzu} K_v^2 \quad (4.27)$$

Where v_{fv} = volume fraction of voids, v_{fp} = volume fraction of particles, they are different things, μ_m = material constant, y_{cu} = compressive yield stress of unmodi-

fied polymer, r_{pzu} = radius of plastic zone at fracture (more is shown in the Section below), K_v = stress concentration factor for voids, depends on the volume fraction of reinforcement and can be expressed as:

$$\Delta G_v = \left(\frac{1 - \mu_m^2}{3} \right) (v_{fv} - v_{pv}) \sigma_{ycu} r_{pzu} K_v^2 \quad (4.28)$$

Where v_{fv} = volume fraction of voids, v_{fp} = volume fraction of particles, they are different things, μ_m = material constant, σ_{ycu} = compressive yield stress of unmodified polymer, r_{pzu} = radius of plastic zone at fracture (more is shown in the Section below), K_v = stress concentration factor for voids, depends on the volume fraction of reinforcement and can be expressed as:

$$K_v = 0.918v_f + 2.11 \quad (4.29)$$

There are two assumptions in void growth:

1. Assume $v_{pv} = v_p$ (100% of particles show debonding and void growth)
2. Assume $v_{pv} = 0.143 v_p$ (14.3% of particles show debonding and void growth)

The 14.3% is the amount of debonding and void growth for silica particles found in most studies such as Hsieh et al.[29] and Bray et al.[67], there is a theoretical prediction that there is a 1/7 chance that a randomly dispersed nanoparticle would be debonded, which makes a 14.3% chance that a nanoparticle will be debonded [67]. For silica-modified epoxy in the present work, similar toughening mechanisms, of shear band yielding between particles and plastic void growth are expected to result from interfacial debonding and plastic deformation of the polymer [29].

4.7.4 Plastic zone size consideration

Plastic deformation is often the main energy dissipation mechanism in brittle materials. With the use of linear elastic fracture mechanics (LEFM) method, the radius of the plane-strain plastic deformation zone (r_{pz}) can be found from the equations below [26]: For unmodified epoxy:

$$r_{pzu} = \frac{1}{6} \left(\frac{K_C}{\sigma_{yt}} \right)^2 \text{ or } \frac{1}{6} \left(\frac{EG_c}{(1 - v^2)\sigma_y^2} \right) \quad (4.30)$$

For nanoparticle-modified epoxy:

$$r_y = K_v m^2 \left(1 + \frac{m}{3^{1/2}} \right)^2 r_{pzu} \quad (4.31)$$

where r_{pzu} = radius of plastic deformation zone of unmodified epoxy, μ_m = coefficient of increase of shear yield stress with hydrostatic pressure, for epoxy this is between 0.175 to 0.225 [26]. K_{vm} depends on the volume fraction of particles (V_{fp}), and can be expressed as [29]:

$$K_{vm} = 3.9337V_{fp} + 2.1126 \quad (4.32)$$

The parameters used in the equations are listed in Table below.

Table 4.11: Values of parameters used for toughening predictions.

Parameter	Symbol	Unit	Value	Source
Fracture energy of unmodified epoxy	G_{cu}	J/m ²	133	[29]
Compressive yield stress of unmodified epoxy	σ_{ycu}	MPa	123	[29]
Young's modulus of unmodified epoxy	E_u	GPa	2.9	[29]
Compressive failure strain of unmodified epoxy	γ_{fu}	/	0.62	[29]
Poisson's ratio of unmodified epoxy	ν	/	0.35	[29]
Maximum stress concentration around a particle	K_{sp}	/	1.65-1.709	Present study
Maximum stress concentration around a void	K_v	/	2.12 (case 1)	Present study
Volume fraction of particles	V_f	/	0-0.22	Present study

4.7.5 Predicted results

Modulus predictions from Halpin-Tsai model

Silica-modified epoxy:

The predicted modulus values of the silica-modified epoxy are shown below. An overall comparison of all three cases of predictions is shown in Figure 39. Predicted modulus values were very close to measured, there was a linear increase in modulus in the predictions when the % of silica particles increased. It is expected as there were larger variations when producing materials of similar %. Predictions agreed well with the experimental results.

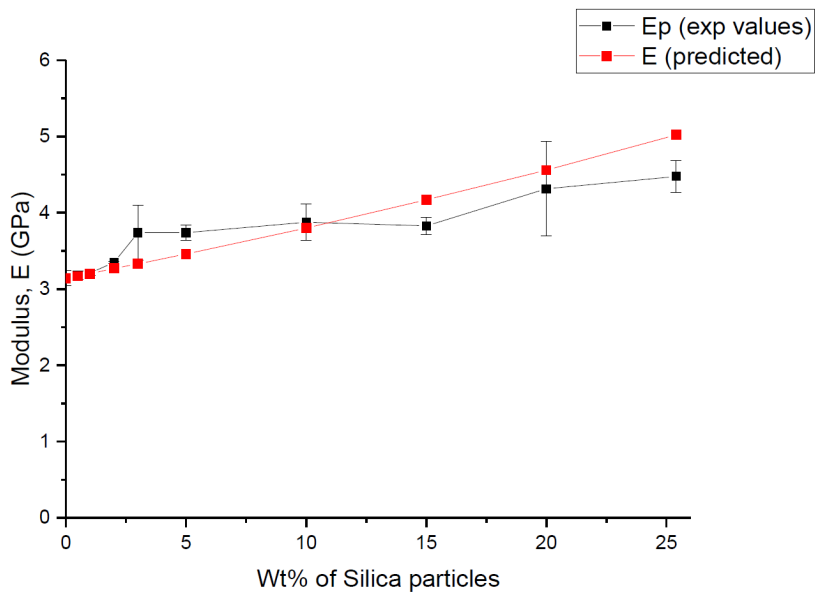


Figure 4.29: Predicted modulus from Halpin-Tsai model of silica-modified epoxy

Table 4.12: Predicted modulus from Halpin-Tsai model of silica-modified epoxy

Particles	Silica		
	% of particles	Measured Young's Modulus (GPa)	E (predicted) (GPa)
0	0	3.14	3.14
0.5	0.5	3.18	3.17
1	1	3.21	3.20
2	2	3.35	3.27
3	3	3.74	3.33
5	5	3.74	3.46
10	10	3.88	3.80
15	15	3.83	4.17
20	20	4.31	4.56
25.4	25.4	4.47	5.02

CSR-modified epoxy:

The predicted modulus values of the CSR-modified epoxy are shown below. The predicted modulus values were almost identical to measured ones, except for the highest %. There was an unexpected reduction at CSR 10%, it could be due to clustering of particles when the % was high (10% was the highest possible % of CSR that can be

added into the resin). The predicted value suggested that higher modulus could be obtained with a better distribution of particles.

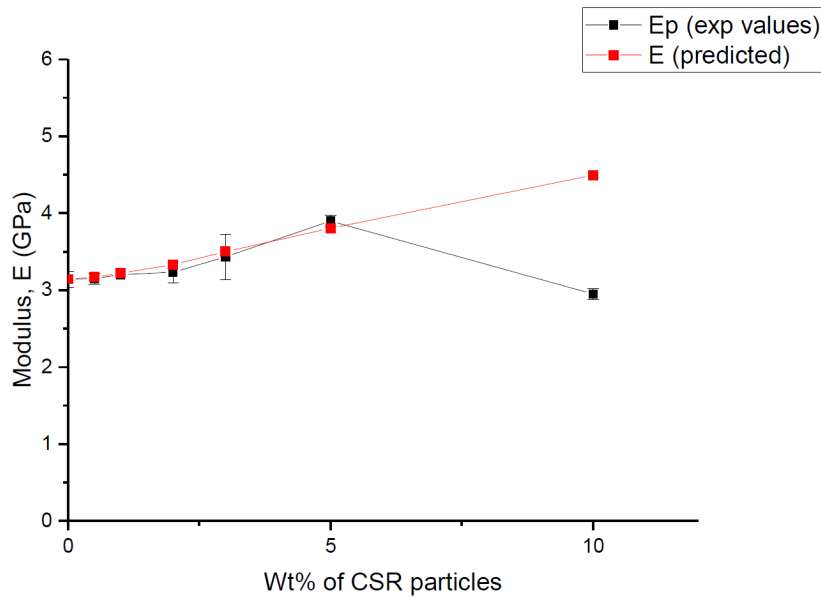


Figure 4.30: Predicted modulus from Halpin-Tsai model of CSR-modified epoxy

Table 4.13: Predicted modulus from Halpin-Tsai model of CSR-modified epoxy

Wt % of CSR particles	E (measured)	E (prediction)
0	3.14	3.14
0.5	3.15	3.17
1	3.20	3.22
2	3.23	3.33
3	3.43	3.50
5	3.90	3.80
10	2.95	4.49

Hybrid-modified epoxy:

The predicted modulus values for the hybrid-modified epoxy are shown below. A similar pattern of results was found in the hybrid-modified epoxy, but experimental values were slightly higher than prediction. These suggest that the synergy effect was higher

than expected, investigation on their fracture surface would reveal more about the mechanisms involved.

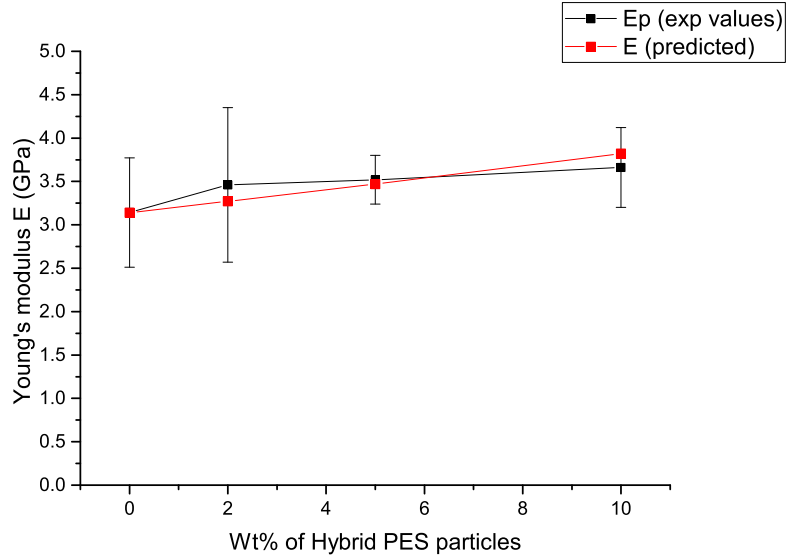


Figure 4.31: Predicted modulus from Halpin-Tsai model of hybrid-modified epoxy

Table 4.14: Predicted modulus from Halpin-Tsai model of Hybrid-modified epoxy

Wt % of hybrid particles	E (measured) (GPa)	E (predicted) (GPa)
0	3.1	3.14
0.5	3.6	3.17
1	3.4	3.19
2	3.5	3.24
3	3.8	3.28
5	3.8	3.38
10	3.5	3.64

Fracture energy predictions from Huang & Kinloch model

There are three cases in the assumptions of fracture energy predictions using the Huang and Kinloch [48] model:

1. Assume $V_{pv} = V_p$ (100% of particles show void growth).
2. Assume $V_{pv} = 0.143 V_p$ (14.3% of particles show void growth).
3. Shear only.

All three cases were used in comparing fracture energies values found in experiments. The predictions from assuming 100% void growth are shown in Table 14, predictions from assuming 14.3% void growth are shown in Table 15, and predictions from assuming there was only shear are shown in Table 16. The fracture energy predictions of silica-modified epoxy are shown in Table 17 and Figure 42. Results obtained from experiments were found to be very similar to the results found from Hsieh et al. [2], except for one of the percentages (15% of silica). The prediction of 14.3% of void growth results agreed with the experimental findings. This finding is reliable as about 14.3% of debonding and void growth was also found in existing studies, e.g. Bray et al. [67].

Table 4.15: Table showing fracture energy predictions from assuming 100% void growth

Particles	Silica	CSR	Hybrid (Si+CSR)
Wt % of particles	$G_u + \Delta G_v$ (J/m ²)	$G_u + \Delta G_v$ (J/m ²)	$G_u + \Delta G_v$ (J/m ²)
0	68	68	68
0.5	83	87	89
1	92	99	103
2	109	120	130
3	123	139	154
5	151	174	202
10	216	258	318
15	280		
20	346		
25.4	418.2		

Table 4.16: Table showing fracture energy predictions from assuming 14.3% void growth

particles	Si	CSR	Hybrid
Wt % of particles	$G_u + 0.143\Delta G_v$ (J/m ²)	$G_u + 0.143\Delta G_v$ (J/m ²)	$G_u + 0.143\Delta G_v$ (J/m ²)
0	68	68	68
0.5	80	83	82
1	87	92	90
2	97	105	103
3	106	116	114
5	121	136	134
10	154	178	177
15	185		
20	215		
25.4	246.9		

Table 4.17: Table showing fracture energy predictions from assuming there was only shear

Particles	Silica	CSR	Hybrid
Wt % of particles	$G_u + \Delta G_s$ (J/m ²)	$G_u + \Delta G_s$ (J/m ²)	$G_u + \Delta G_s$ (J/m ²)
0	68	68	68
0.5	79	83	81
1	86	90	88
2	95	102	98
3	103	112	107
5	116	129	122
10	144	164	153
15	169		
20	192		
25.4	217		

Table 4.18: Table showing fracture energy predictions of silica-modified epoxy

Wt % of silica particles	$G_u + \Delta G_v$ (J/m ²)	$G_u + 0.143\Delta G_v$ (J/m ²)	$G_u + \Delta G_s$ (J/m ²)
0	68	68	68
0.5	83	80	79
1	93	87	86
2	109	97	95
3	123	106	103
5	151	121	116
10	216	154	144
15	280	185	169
20	346	215	192
25.4	418	247	217

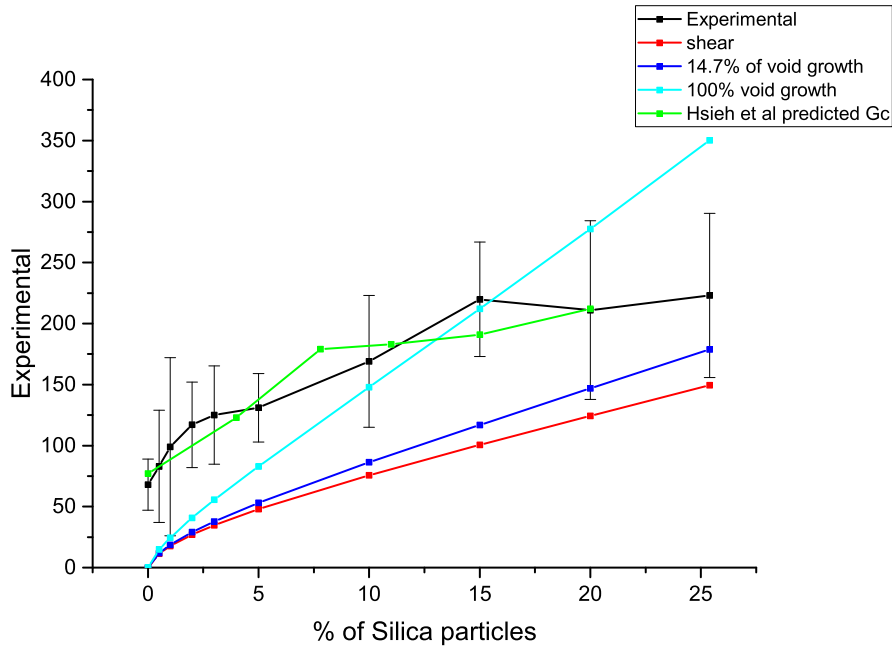


Figure 4.32: Fracture energy prediction of silica-modified epoxy

All three modifications (silica, CSR and hybrid) had similar fracture energies predictions under low % of particles. But when there were high concentrations of particles, the modification using silica particles was the most efficient in toughening effect. The

fracture energy predictions of CSR-modified epoxy are shown in Table 18 and Figure 43. CSR-modified epoxies had the lowest fracture energy values, all three cases of predictions had higher values when compared with experimental results, predictions did not agree with experimental findings. However, the different sizes of CSR found in SEM images could explain the lower values. As particles were assumed to be of the same size in predictions, an average of the size range was used in the calculation, but it may not represent the average size of particles there. There was a large range of particle sizes so using one average value was not applicable, hence the average value of the range provided the best possible estimation.

Table 4.19: Table showing fracture energy predictions of CSR-modified epoxy

Wt % of CSR particles	$G_u + \Delta G_v$ (J/m ²)	$G_u + 0.143\Delta G_v$ (J/m ²)	$G_u + \Delta G_s$ (J/m ²)
0	68	68	68
0.5	87	83	83
1	99	92	90
2	120	105	102
3	139	116	112
5	174	136	129
10	258	178	164

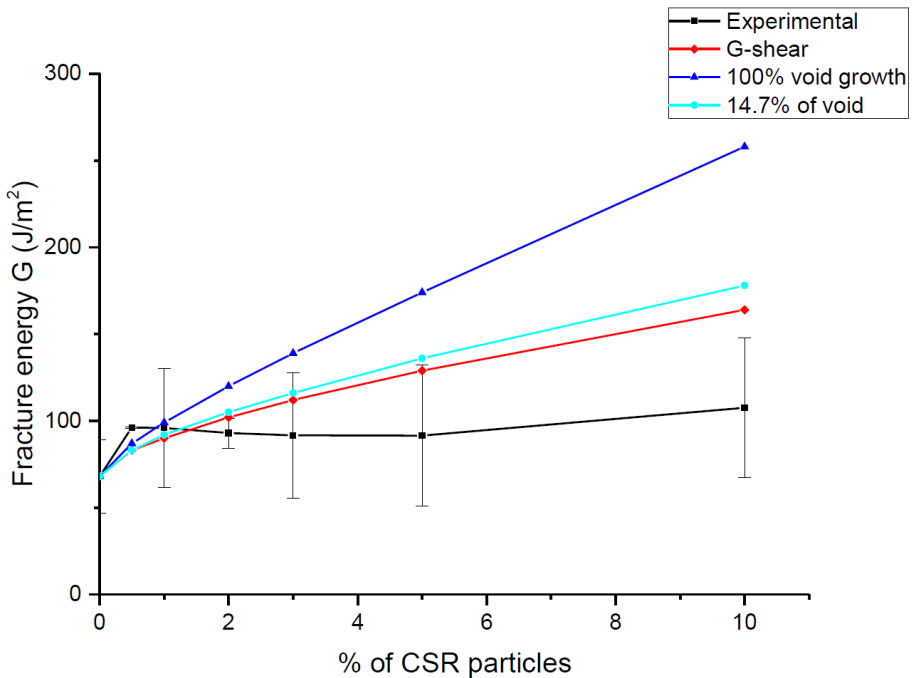


Figure 4.33: Fracture energy prediction of CSR-modified epoxy

The fracture energy predictions of the hybrid-modified epoxy are shown in Table 19 and Figure 44. The use of hybrid particles did not show a clear synergy effect, the predicted values were similar to the silica-modified epoxies at low % of particles while lower values were predicted when there was a high % of particles. The prediction with shear only case had very similar results when compare to the assumption of 14.3% of void growth, these values were also very similar to experimental results but with slightly higher values. Overall, 100% of void growth would always provide the highest fracture energy, and with shear only, a relatively lower fracture energy would be expected according to predictions. The assumption of 14.3% of void growth agreed with most of the experimental results, the cause of disagreement in some specimens with higher % of particles were justified by their fracture surfaces. Hence, it can be concluded that experimental findings were according to the predictions.

Table 4.20: Fracture energy predictions of hybrid-modified epoxy

Wt % of Hybrid particles	$G_u + \Delta G_v$ (J/m ²)	$G_u + 0.143\Delta G_v$ (J/m ²)	$G_u + \Delta G_s$ (J/m ²)
0	68	68	68
0.5	89	82	81
1	103	90	88
2	130	103	98
3	154	114	107
5	202	133	122
10	318	177	153

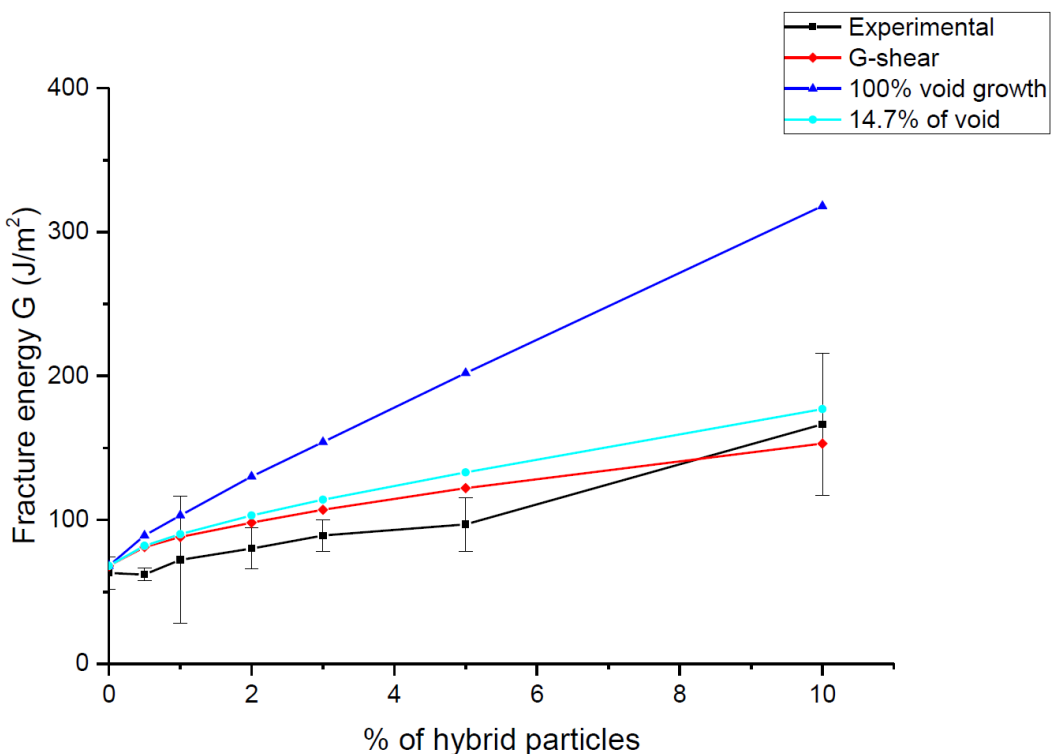


Figure 4.34: Fracture energy prediction of hybrid-modified epoxy

4.8 Scanning electron microscopy

4.8.1 Introduction

Scanning electron microscopy (SEM) gives images of the fracture surfaces, and provides supporting evidence (for example the presence of river lines) to the failure mechanisms. Fracture surface specimens were cut as thin as possible, specimens were about 2 mm thick to reduce charging, and the surface of specimen was protected when it was being cut. CNC machine was used in cutting the TDCB specimens.

4.8.2 SEM results

CSR

1. Rate effect

Figures 45 to 47 show SEM images of CSR-modified epoxy under different rates of test. There were some particles fractured but the major toughening mechanism in CSR was

local deformations instead of debonding, the river lines on the surface indicated that crack was travelling very quickly, and it then split into several paths. The effect of rate did not make any significant changes in the appearance of the fracture surfaces and the toughening effect. The same conclusion was found in both TDCB and SENB specimens.

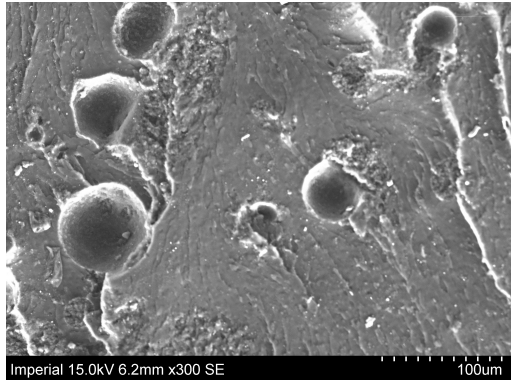


Figure 4.35: CSR-modified epoxy specimen tested under quasi-static rate

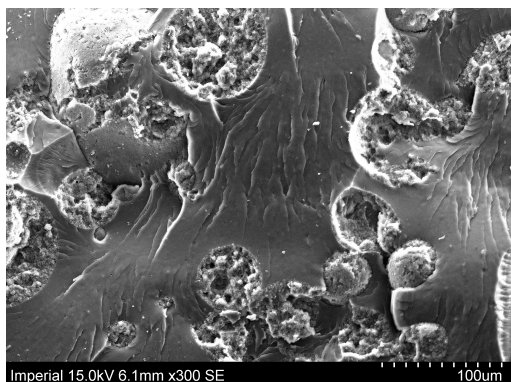


Figure 4.36: CSR-modified epoxy specimen tested under quasi-static rate

Voids in TDCB and SENB specimens

Figure 49 and 50 show SEM images of voids in CSR-modified epoxy TDCB and SENB specimens. More voids were found in TDCB specimens when compared to SENB specimens, and would be due to the air bubbles induced during preparation of joints. The voids in SENB specimens were also found smaller than voids in TDCB specimens. The void diameters were estimated with the use of software ImageJ, Figure 48 shown below. After times the ratio of the scale, average void size was found to be $2.26 \times 10^{-4} \mu\text{m}$ (with standard deviation of $7.75 \times 10^{-5} \mu\text{m}$).

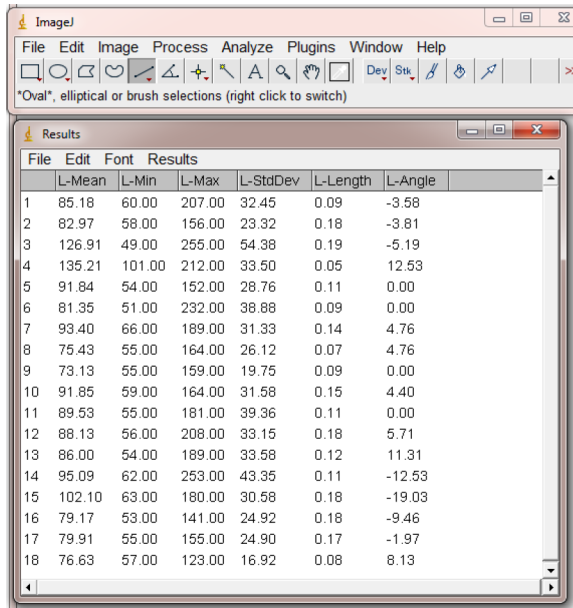


Figure 4.37: Estimation of void diameters

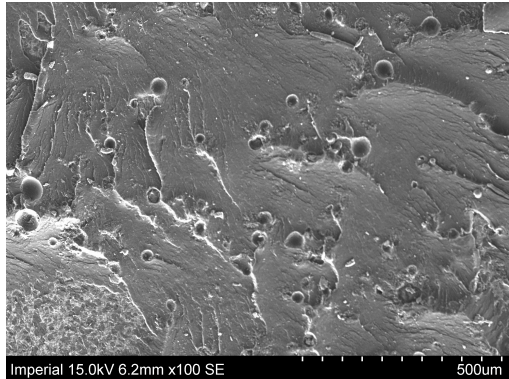


Figure 4.38: Area with voids in CSR-modified epoxy SENB specimen

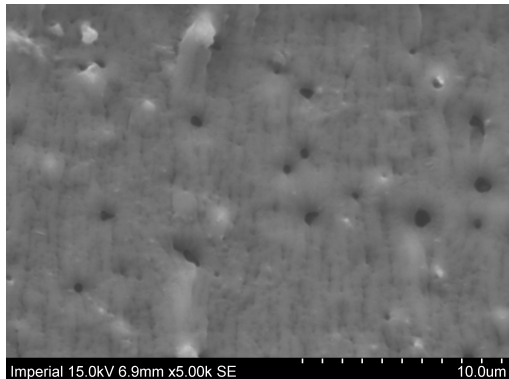


Figure 4.39: Area with voids in CSR-modified epoxy SENB specimen

Deformation of particles

The shape and appearance of the original CSR particles are shown in Figure 51. The size of particles were more varied than expected. The fracture surfaces of the CSR-modified epoxy showed some fractured CSR particles, see Figure 53. Figures 52 and 53 show examples of CSR particles under a sharp cut and damaged after testing. It is believed that rubber bridging had occurred as there were no cavitations could be found after looking at the individual deformations of the particles under high magnifications. In order to investigate if the damages in particles were there before testing or not, particles were viewed under SEM before and after cutting them with a razor blade. By comparing the shape and structure of the sharply cut particles to the deformed ones, it is clear that the damages were produced naturally under testing. There were a large amount of damage particles found in epoxy with high % of particles, and especially when they were undergo more brittle failure when temperature was lower.

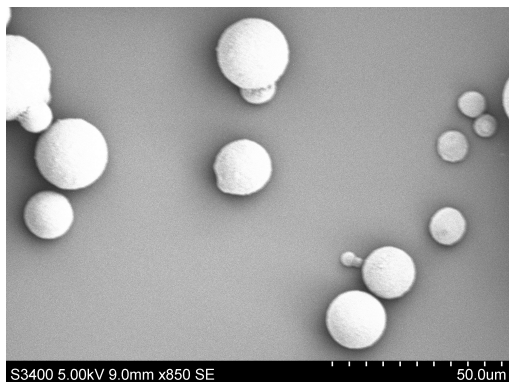


Figure 4.40: Original CSR particles

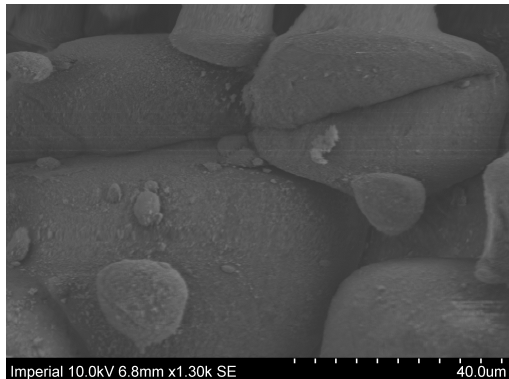


Figure 4.41: Cut CSR particles

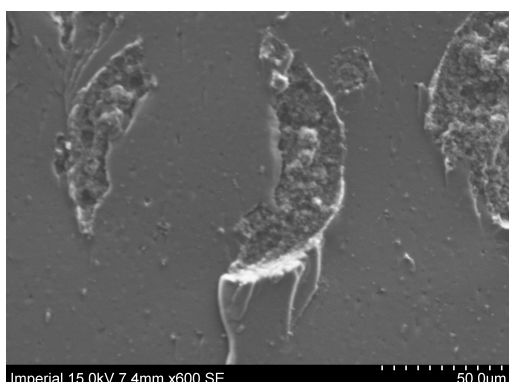


Figure 4.42: Example of damaged CSR particles

Effect of concentration of particles

Figures 54 to 57 show different % of CSR modified epoxy under SEM imaging. There were different fracture surfaces when the % of particles were different. When the % of particles was low, brittle surfaces were found, where particles were very distinct from the bulk epoxy. However, when the % of particles were high, rough surfaces were found, as the particles provided the roughness of the surface, the high amount of them increased roughness. Due to the high roughness, the particles cannot be recognised as easily, but they were not dissolved into the resins and there no phase inversion occurred. The high fracture energies values found in high % of CSR could be explained by their fracture surfaces, as localised deformations were found in more than 90% of the particles, toughening effect was significant, particles were highly deformed from their original shape, but were not stretched. There were about a quarter of the particle cores

completely removed from the particle, leaving an entry space inside (cavitation). The SEM images shown that particles were mixed evenly but most of the particles did not have the same sizes. The average size of particles was found to be $1.57 \times 10^{-5}\mu\text{m}$ with standard deviation of $1.13 \times 10^{-5}\mu\text{m}$. Hence the particle sizes from the SEM images were found to be in-between 2.7 to $0.44 \times 10^{-5}\mu\text{m}$. This could explain why some of the tests shown higher fracture energies values than the others, hence the high standard deviations.

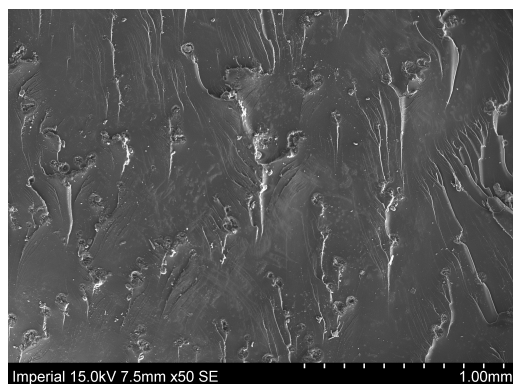


Figure 4.43: CSR 0.5% specimen

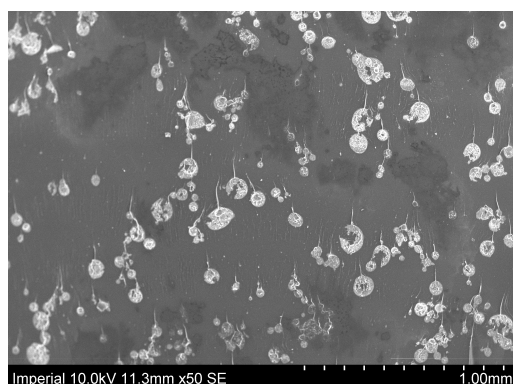


Figure 4.44: CSR 3% specimen

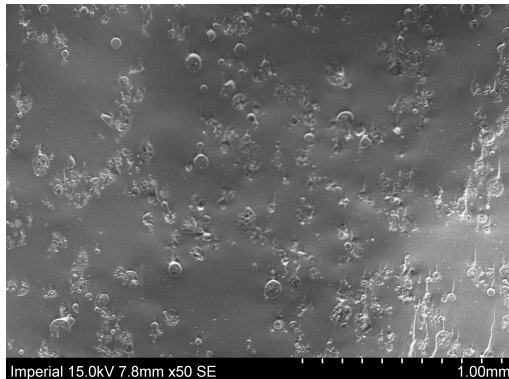


Figure 4.45: CSR 5% specimen

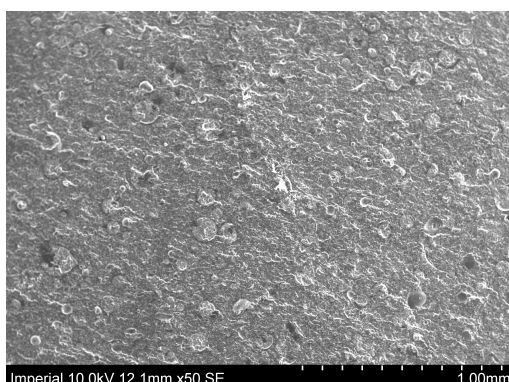


Figure 4.46: CSR 10% specimen

Examples of localised deformations in the particles are shown below in Figures 58 to 61. The particle size was smaller than the size of void, therefore there was a large amount of deformation. Most of the particles were highly damaged, either by crack propagated through the whole particle or cavitation, all the damaged particles were highly deformed from its original shape. There were many small voids inside a deformed area of a particle (Figure 60), rough surfaces were observed especially with high % of CSR particles (10 wt%). Rough surfaces were produced due to the presence of high amount of deformation when toughness is high, a smooth plane is formed as a result of each particle interacts with the crack tip [68]. The surfaces of the fractured particles were very similar to the epoxy matrix, which suggested that particles were undergoing a similar failure process as the epoxy matrix (deformation and void growth). But this similarity was not expected, further investigations regarding their failure mechanism would be performed by DMA, which would provide more information about the failure

properties of CSR specimens, more about DMA study is described in section 11.

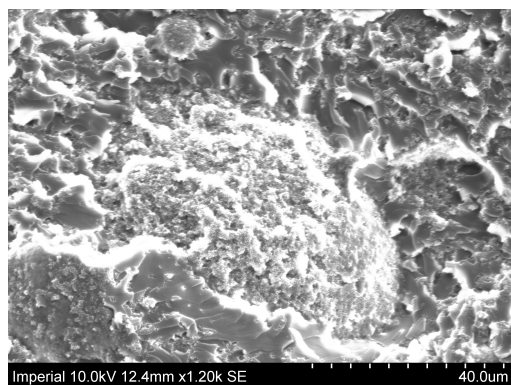


Figure 4.47: Deformed CSR particles for high % of CSR specimen

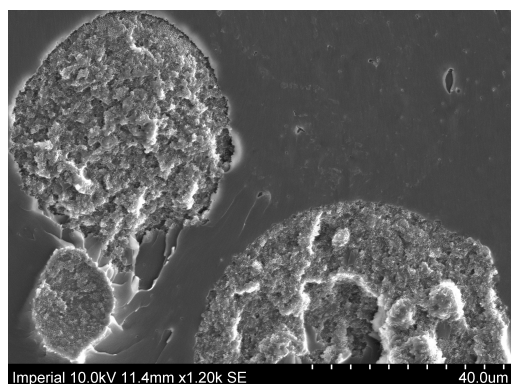


Figure 4.48: Deformed CSR particles for low % of CSR specimen

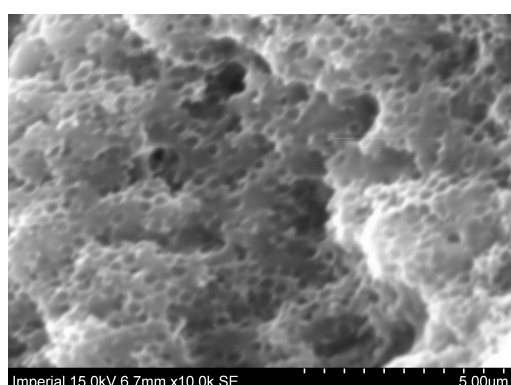


Figure 4.49: Small voids inside a particle

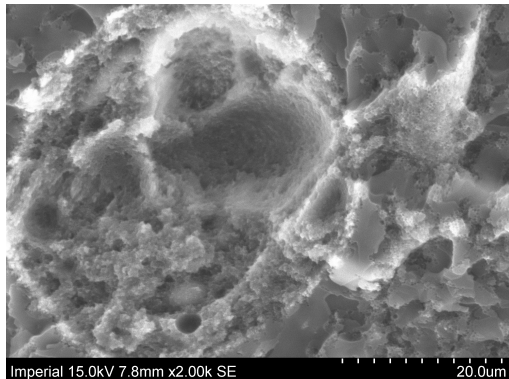


Figure 4.50: Example of CSR particle deformation at high magnification

Effect of low temperature

Figures 61 to 63 show SEM images of CSR modified epoxy specimens tested at different temperatures. There was no significant difference between the fracture surfaces of the epoxy tested at low temperature and normal room temperature. There were more river lines in some specimens as the fracture were more brittle, and sharper edges can be observed. There were higher fracture energy values when specimens were tested under low temperature. The low temperature environment produced a more brittle failure, higher fracture toughness and fracture energy values were found. The increased in brittleness had significantly enhance toughening of particles reinforced epoxy. Similar behaviours were expected to be found in high rate TDCB testing that will be performed in the next stage.

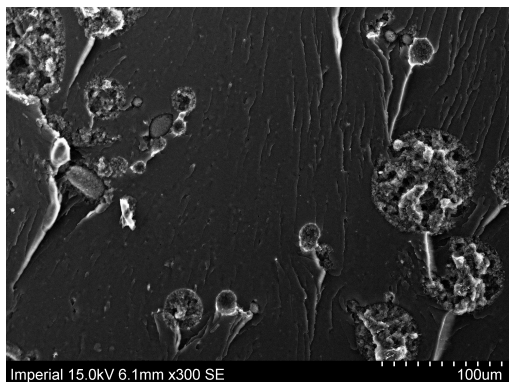


Figure 4.51: CSR-modified epoxy specimen tested at room temperature

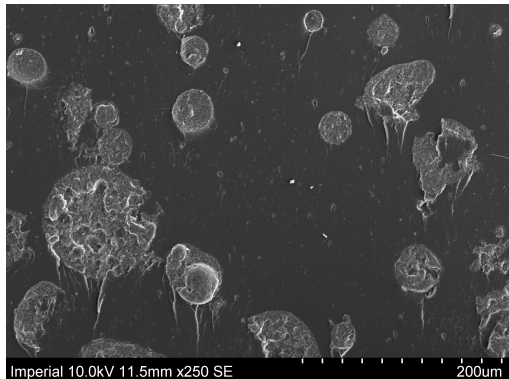


Figure 4.52: CSR-modified epoxy specimen tested at $40^{\circ}C$

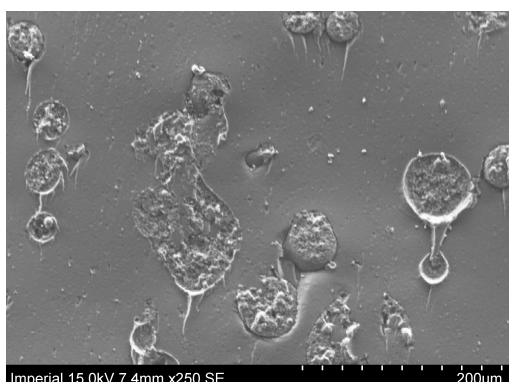


Figure 4.53: CSR-modified epoxy specimen tested at $80^{\circ}C$

4.9 Finite element analysis (FEA)

4.9.1 Finite element analysis introduction

The experimental results found would be compared with the results of a modelling study using Abaqus. The amount of debonding of particles would be calculated with the use of 2D plane-strain cohesive surface elements, where only mode I would be considered. The boundary conditions would be at the front of the beams, and Figure 65 shows the movements in the beams. For the lower beam, as there would be a small rotation in the beam during the mode I test, rotation would be allowed. No movement in any direction other than y would be allowed. For the front of the upper beam, only the mode I opening (y-direction) would be allowed to move.

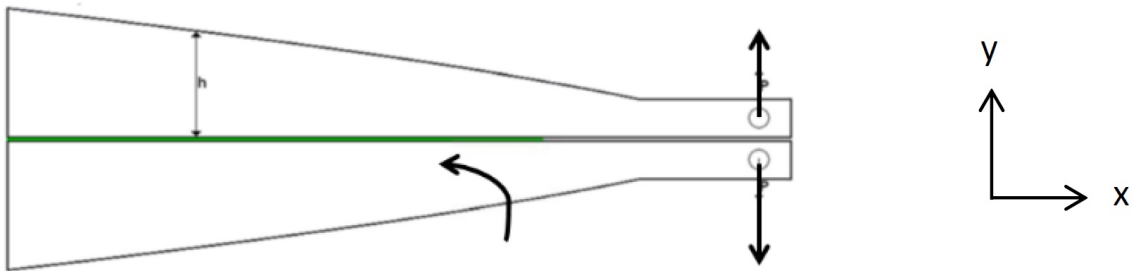


Figure 4.54: Forces in TDCB (modified from [69])

Table 20 below shows the material properties information in the study. The properties of the epoxy were obtained from calibration of the stress-strain data from other studies in the group.

Table 4.21: Properties of aluminium alloy (EN AW 2014-A) [69] and epoxy [38] for the FE model

Property	Al alloy	Epoxy
E (GPa)	72.4	2.9
σ_y (MPa)	430	-
UTS (MPa)	485	-
ρ_s (kg/m ³)	2700	1200
v_s	0.33	0.35

The initial values of the fracture energies used were taken from the average initial value from experimental results. Cohesive traction-separation would be used as parameters in the simulation. When only mode I is under consideration, the parameters for describing cohesive law are stiffness K_I , the separation at damage initiation, $\delta_n 0$ and critical energy release rate (fracture energy), G_C [69]. Figure 66 shows the traction-separation curve.

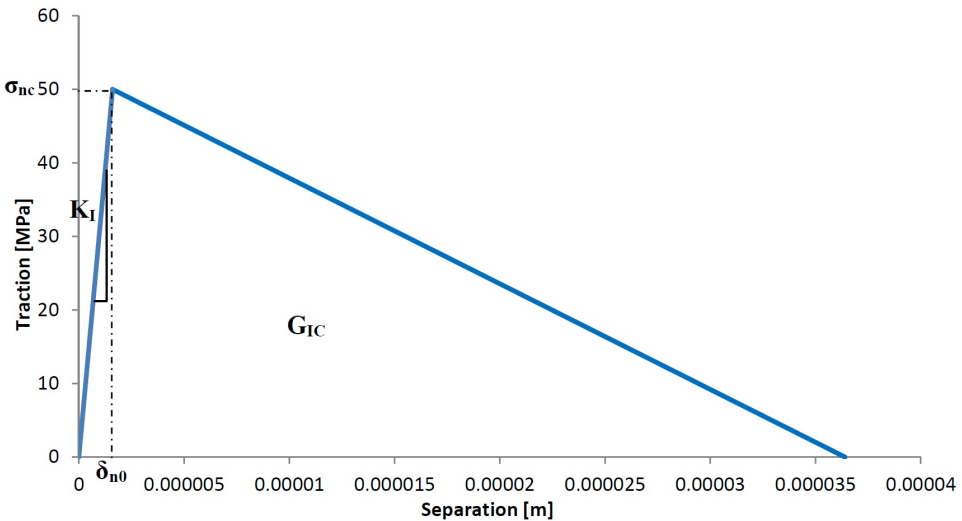


Figure 4.55: Traction-separation curve [69]

The values for the traction-separation curve are calculated using [69]

$$K_I = \frac{E}{t_a} \quad (4.33)$$

$$\delta n_0 = \frac{\sigma_y}{Et_a} \quad (4.34)$$

$$\delta_n c = \sigma_{n0} K_I \quad (4.35)$$

where t_a is the thickness of the adhesive layer.

4.9.2 Finite element analysis results

As initial values from experimental results were used, the failure predictions were assumed to have the same failure pattern as experimental ones, so when there were only stick-slip events found from experimental results, there would only be initiation and arrest points predicted in the model. Most of the prediction of fracture energy values were found to be similar to the experimental values, however, there was no very clear trend shown regarding relationship between fracture type and % of particles used.

Silica-modified epoxy

The FEA prediction results for the silica-modified epoxy are shown in Figure 67. The FEA model predictions had a very similar pattern of curves in silica, most of the results agree with the experimental data, but predicted model had slightly higher values than experimental data. The shape of the prediction curve for propagations was exactly the same as the experimental one, while some of the stick-slips values were predicted to an about 1 time higher values. There had been interfacial failure for the silica-modified epoxy TDCB specimens, which would reduce the fracture energy measurements, it is therefore expected to have higher predicted values. There were no stick-slips for specimens with 20 and 25.4% of silica particles added, therefore they were indicated as zero for the initiation and arrest points predictions.

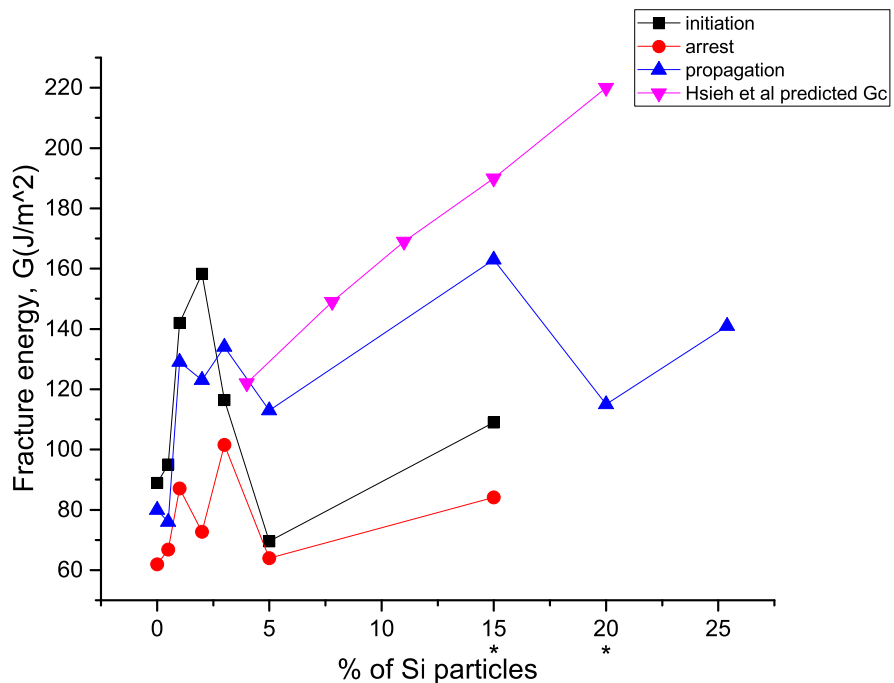


Figure 4.56: FEA predictions and experimental data of silica-modified epoxy

CSR-modified epoxy

FEA predictions results of CSR-modified epoxy were shown in Figure 68. The predicted results were very similar to the experimental data with slightly lower values, predicted

results agreed well with the experimental findings. There were mostly cohesive failure in the CSR modified epoxy TDCB specimens and hence results were reliable.

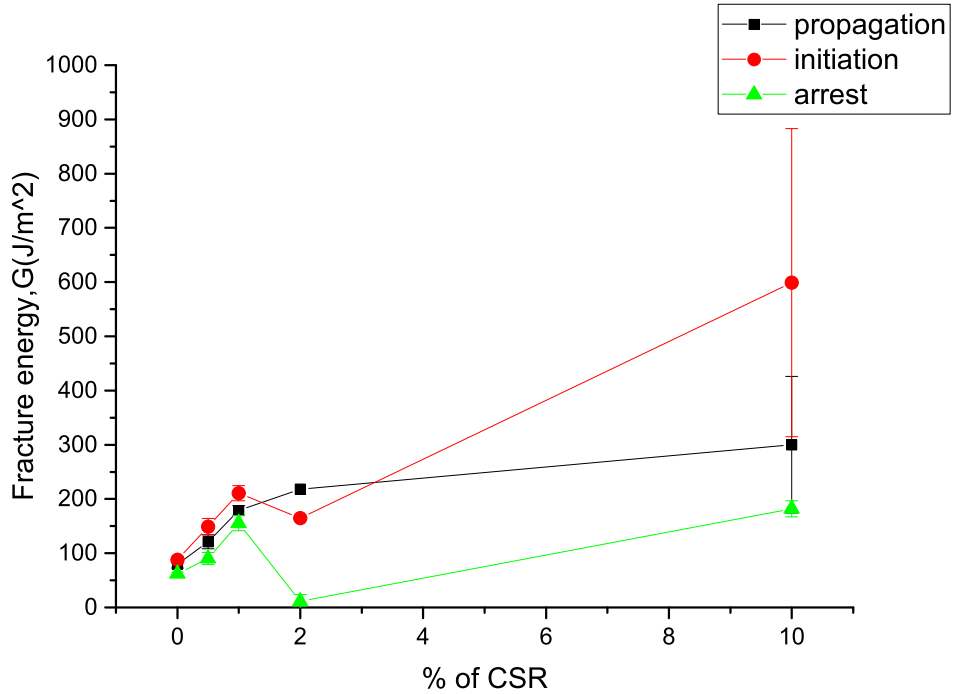


Figure 4.57: FEA predictions and experimental data of CSR-modified epoxy

4.9.3 Progress

To solve the problem of interfacial failure in the TDCB specimens, SENB tests were performed to provide comparisons of toughness values to those found from TDCB specimens. Progress has been made in investigation of the effect of nanoparticles added in epoxy, the study is now focusing on the effect of test rate. To account for the dynamic effect in high rate SENB, low temperature SENB tests were performed but not included in this report. It was found that fracture of rubber-modified-epoxy was highly affected by temperature and test rate; the compressive modulus reduced with increasing temperature and lowering of test rate; fracture toughness increased when temperature increased and with decreasing test rate [70]. The use of DMA study (which is in progress now) would also provide insight of rate-controlled mechanical testing without dynamic effects. There have been experiments done with a large range of temperature, temper-

ature between -40 °C and 80 °C in 20 °C steps, a master curve (a curve with shifted results under different temperatures) against time was found [70]. Time-temperature relationship was investigated further in studies from Huang and Kinloch [71], both time-to-failure and time-temperature shift factor graphs were obtained with temperature of -80 to 40 °C, very fine superimposed graphs were found in all results in their study. It is expected that the DMA results would explain more regarding the rough surfaces and other fracture behaviours found in SEM images. The overall properties of the current materials will be compared with ceramic and PES particle modified epoxy. Further progress in the study of rate effect to the fracture behaviour of materials and finalising of the finite element model is expected in the next stage of the study.

4.10 W210 and PES materials

4.10.1 Materials information

In order to provide an all-rounded comparison of particles modified epoxies, PES (Polyether-sulphone), PES hybrid (PES+Silica), ceramic microspheres and ceramic hybrid (ceramic+CSR) were also used in this study and results were compared with previous results [the Silica, CSR and hybrid (Silica+CSR)]. SUMIKAEXCEL PES (Polyether-sulphone) Polyethersulphone is a thermoplastic, it is available as a heat resistant amorphous resin or in powder form. It has a high Tg of 225°C, often powder form is used for modifying epoxy to improve impact strength. The powder form used is the 5003P grade, which has the reduced viscosity of 0.5, it has good adhesion properties because of the presence of terminal hydroxyl group, range from 0.6–1.4% polymer repeating units [73]. Due to the properties of the blend, it is expected to have 3 phases when different % of particles were added:

At low %: particles of PES

At medium %: Co-continuous (CC) structure

Co-continuous phase: One phase inside the other, usually formed when the viscosities are equal, 50:50.

At high %: Phase inversion (PI)

Co-continuous phase and phase inversion were often observed in thermoplastic modified epoxies, such as study from J.Chen et al [12]. The bicontinuous phase can in some cases have a better fracture resistance than phase-inversed structure, due to the lack of adhesion between both phases.

% of PES particles added in were: 0, 2, 5, 10, 15, 20% and Hybrid (*PES + SiO₂*)

with 2 and 5% were also made. When the % of hybrid particles were higher than 5%, specimens could not be manufactured, as the saturation of particles makes mixing and curing impossible. Mixing of PES: PES particles were first dissolved in epoxy before mixing with silica and hardener. After a few trials, it is found that the particles would be dissolved at about 145°C overnight. Electric mixer was used throughout the whole process to ensure particles were evenly distributed. 3M ceramic microspheres W210 3M ceramic microspheres W210 are white-coloured high-strength microspheres that composed of Alkali Alumino Silicate Ceramic, and with size $13\mu\text{m}$ by volumes, surface area of $5 \text{ m}^2/\text{cc}$ and true density of $2.4\text{g}/\text{cc}$. They are often used to reduce VOC levels, increase filler loadings, and improve hardness and abrasion resistance [74]. % of W210 particles added in:

-W210: 2,5 and 10%

-Hybrid W210+CSR: 2,5 and 10%

Ceramic microspheres are more commonly used as an additives in paint and coating, to provide resistance to high temperature. Ceramic modified epoxy is also used as floor coating for factory or warehouse to improve abrasion resistance.

4.10.2 Tensile results of PES and W210

Tensile results of PES and Hybrid PES (PES+Silica) were shown below (table and figure), they shown similar values as those found in CSR and hybrid (Silica and CSR) specimens. However, curve was more stable with small standard deviations, hence, the trends observed were more reliable. There was a gradual increase in Modulus when the wt% of particles increased, but the amount of improvement was small, there was only a 17% of increase in modulus when maximum amount of particles were added. The trend for PES and Hybrid PES were found very similar. Hybrid PES shown a higher modulus when wt% of particles added in was moderate, but similar values were found with maximum wt%. To conclude, since the modulus values were similar to those from CSR and hybrid specimens, it is expected that they would show similar SENB results as those from CSR and hybrid specimens, but not for their fracture behaviour. PES is expected to have a different fracture behaviour than other particles compared here, due the nature of PES particles; for example the increase in crosslinking density of epoxy would increase toughness for PES, which is opposite the rubber particles; the 3 phases of the PES blend is expected produced a greater different in their fracture behaviour, more regarding their fracture and toughening mechanisms would be reveal from SEM imaging.

Table 4.22: Tensile modulus results of W210 ceramics modified epoxy

particles	PES		Hybrid PES	
% of particles	Young's Modulus (GPa)	SD	Young's Modulus (GPa)	SD
0	3.14	0.83	3.14	0.63
2	3.28	0.074	3.46	0.89
5	3.33	0.092	3.52	0.28
10	3.62	0.089	3.66	0.46

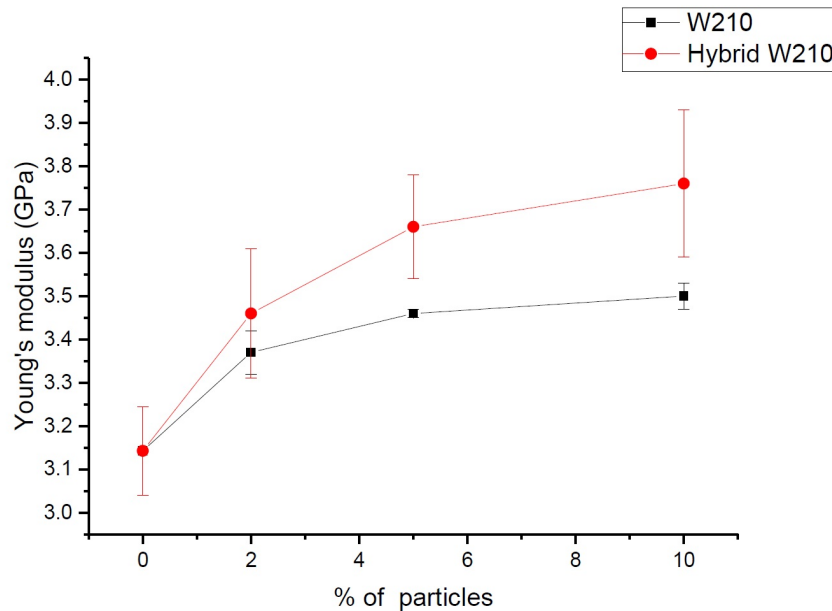


Figure 4.58: Tensile modulus results of W210 ceramics modified epoxy

4.11 Low temperature SENB

SENB testing was performed under -40 and -80°C to investigate fracture behaviour under brittle conditions, which was equivalent to testing under high rate. The whole setup was placed in a temperature chamber, specimens were placed inside the chamber for five minutes for reaching the same temperature as the environment. After one test had finished, next test was performed only after temperature reached back to the level, this could ensure all the tests were performed under the same conditions. However, the machine could become frozen after a while, this is also related to the amount of

liquid nitrogen supply (more at the beginning). This affect the temperature control, which is maintained by the fan. The large differences in temperature in between inside and outside of the chamber produced large and quick changes in the temperature, the system and the fan may not be able to maintain a constant temperature under these conditions, hence could affect the accuracy of temperature reading. Therefore, small differences in testing temperatures were not suggested, as that would produce a larger variation in the test.



Figure 4.59: Low temperature SENB setup 1



Figure 4.60: Low temperature SENB setup 2

4.11.1 Low temperature SENB results (Silica, CSR and Hybrid of both)

All SENB tested under low temperature had higher Fracture toughness and fracture energy values, values were higher when temperature was lower. The results were more reliable with smaller standard deviations for all formulas. There was a clearer increase trend in fracture properties when % of particles increased, which shown that the effect of toughening was more significant when materials were under more brittle failure.

Silica specimens

There was a significant increase in fracture energy found in all % of Silica tested under -80°C. The increase was more significant with high % of silica particles, more than 1 time of increase was measured. However, specimens that were tested under -40 °C were found to have lower fracture energy values than those tested at room temperature for 10 or higher wt% of particles. Although it was not significantly lower, these results were not expected. This could be due to the variations of readings during the starting of the experiment with the temperature chamber. When the load cell get moist (due to water condense when it is cooling down), reading of load cell can be affected and hence affected the results.

Table 4.23: Fracture energy of Silica modified epoxy under low temperature

Temperature	Room temperature (20°C)		-40 °C		-80 °C	
	% of Si particles	G (J/m ²)	SD	G (J/m ²)	SD	G (J/m ²)
0	68	21	93.5	9.2	126.4	15.1
0.5	83	46	100.7	30.3	129.9	0.0
1	99	73	111.8	0.1	157.7	1.6
2	117	35	116.8	14.1	161.2	16.1
3	125	40.3	132.3	0.0	179.4	2.0
5	131	28	132.1	14.6	213.2	30.0
10	169	54	143.9	6.3	305.1	8.8
15	219.8	46.9	192.1	18.4	311.7	12.5
20	211.0	73.2	196.9	26.8	332.0	5.7
25.4	223.0	67.4	200.4	16.7	349.4	18.9

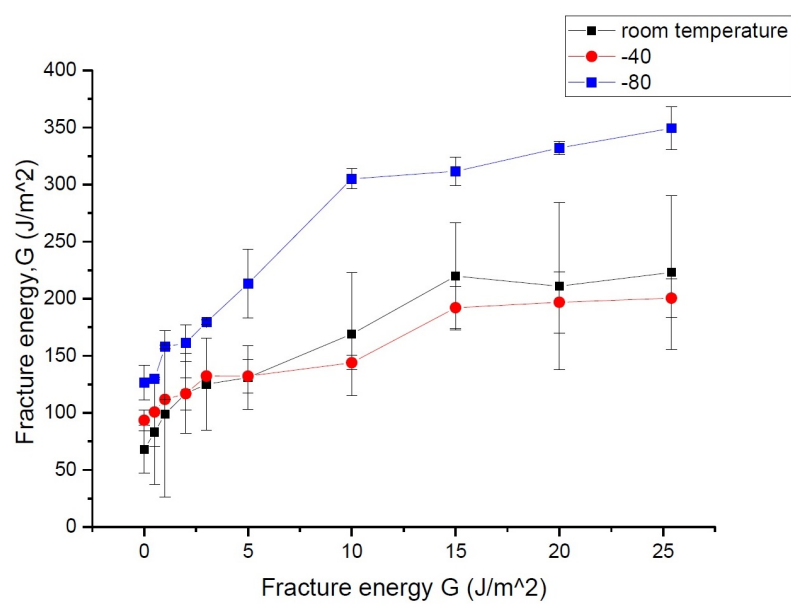


Figure 4.61: Fracture energy of Silica modified epoxy under low temperature

CSR specimens

There were weighty higher fracture energy values found in tests performed under low temperature for all wt% of CSR. The lower the temperature, the more significant is the increase in fracture energy. There was 1 time higher fracture energy found in specimens performed under -80°C when compare to room temperature tests. There was a trend of increase in fracture energy when wt% of particles increased, however, this trend was not found in tests performed under -40°C . The specimens with low particle wt% of CSR particles were found to have higher fracture energy than high wt% of particles. There was a plateau when wt% of CSR particles added in was high. This suggested that the high wt% use of CSR is not the optimum % for toughening, medium to toward lower wt% (5 to 2 wt%) would provide a great toughening effect.

Table 4.24: Fracture energy of CSR modified epoxy under low temperature

Temperature	Room temperature (20 °C)		-40°C		-80°C		
	% of CSR particles	G (J/m ²)	SD	G (J/m ²)	SD	G (J/m ²)	SD
0	68.0	21.0		93.5	9.2	126.4	15.1
0.5	96.1	0.6		140.3	36.8	141.4	8.3
1	96.0	34.2		120.2	24.4	147.8	9.4
2	93.0	8.6		153.8	14.7	149.8	17.6
3	91.7	36.1		110.3	14.9	155.4	14.5
5	91.5	40.8		125.6	6.9	162.7	18.1
10	107.6	40.2		130.5	11.7	187.6	15.7

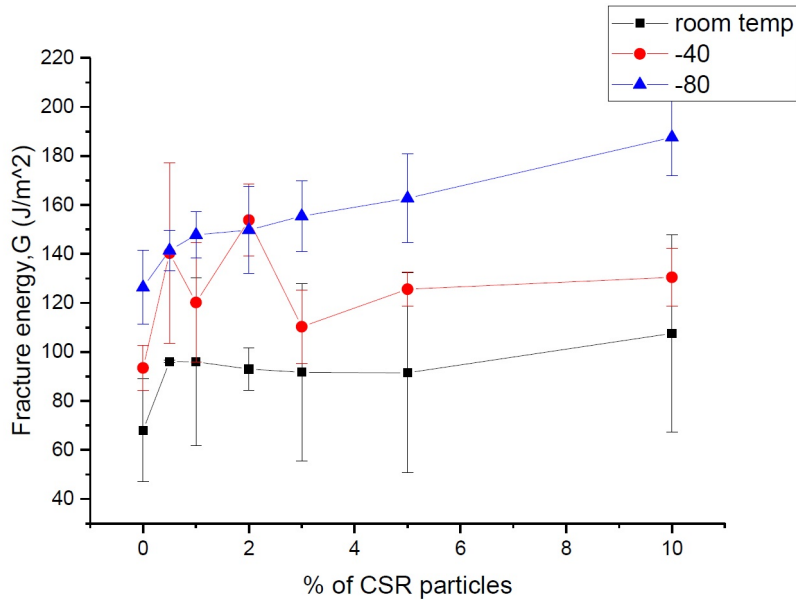


Figure 4.62: Fracture energy of CSR modified epoxy under low temperature

Hybrid specimens

The increase trend for increase in fracture energy when there is an increase in wt% of particles was even more notable with the use of hybrid particles for all temperature conditions, but the trend is smoother, without any outliers. The lower the temperature, the higher the fracture energy. However, the increase in fracture energy under low temperature test was not as significant as with the use of only one type of particles. For 10 wt% of hybrid specimens tested under $-40^{\circ}C$, same average fracture energy was found when compare to the tests performed under room temperature. All the fracture energy values under all temperature were similar to CSR ones, which were smaller than Silica ones. Hybrid particles were expected to produce higher toughening effect, but when particle concentration is too high, it reduces the distance between particles and hence reduce debonding or particles pull out. The values were similar for all temperature, therefore, this would not be cause an error during the test. The optimum amount of hybrid particles used is 5wt% for all temperature.

Table 4.25: Fracture energy of Hybrid modified epoxy under low temperature

Temperature	Room temperature (20 °C)		-40 °C		-80 °C		
	% of Hybrid particles	G (J/m ²)	SD	G (J/m ²)	SD	G (J/m ²)	SD
0	62.9	11.2		93.5	9.2	126.4	15.1
0.5	61.9	4.4		97.8	14.1	130.5	11.6
1	72.2	44.0		96.7	29.2	134.0	13.4
2	80.0	14.3		104.8	8.2	134.2	19.5
3	89.1	11.0		107.3	4.2	135.7	5.9
5	96.9	18.8		116.9	5.0	138.3	16.2
10	166.4	49.5		168.9	6.4	192.4	17.3

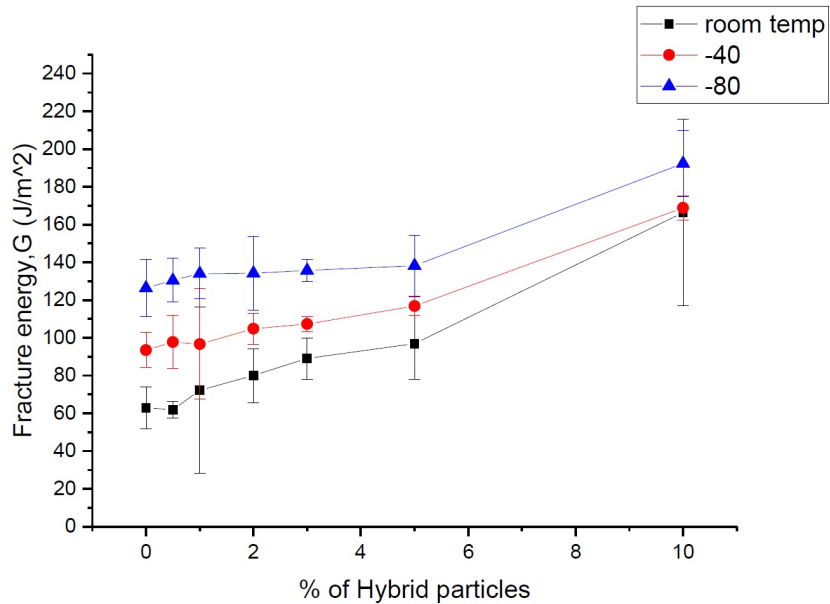


Figure 4.63: Fracture energy of Hybrid modified epoxy under low temperature

W210 ceramics, PES, hybrid W210 (W210 and CSR), Hybrid PES (PES and Silica)

This is shown that there were similar trends in PES and W210 specimens when compare to Silica and CSR specimens, fracture energy was higher when test was performed at a lower temperature as well as when wt% of particles increased. All of them had lower fracture energy values when compare to Silica and CSR. However, these results have smaller Standard Deviations and smoother graphs when compare to results with Silica and CSR. There is a higher reliability in these results, as they are more consistent. SEM imaging would reveal more information regarding their fracture behaviour. Overall, Silica shown to have the greatest toughening effect when compare to all these different types of particles.

PES:

Specimens tested under $-40^{\circ}C$ had the same trend of fracture energy values when compare to room temperature specimens other than the maximum wt%. While a significant increase is shown from specimens tested under $-80^{\circ}C$. The toughening effect was small when PES specimens were tested under room temperature and $-40^{\circ}C$. A large increase (1 time increase when compare to unmodified specimens) was shown in 10wt% PES specimens tested under $-80^{\circ}C$.

Table 4.26: Fracture energy of PES modified epoxy under low temperature

Temperature	Room temperature		-40		-80		
	% of PES particles	G (J/m ²)	SD	G (J/m ²)	SD	G (J/m ²)	SD
0	65.0	21.0		63.0	9.2	73.4	15.1
2	70.0	1.3		75.1	11.5	93.6	2.4
5	77.0	4.2		82.5	5.7	105.6	4.9
10	80.0	5.1		109.3	7.6	148.9	5.8

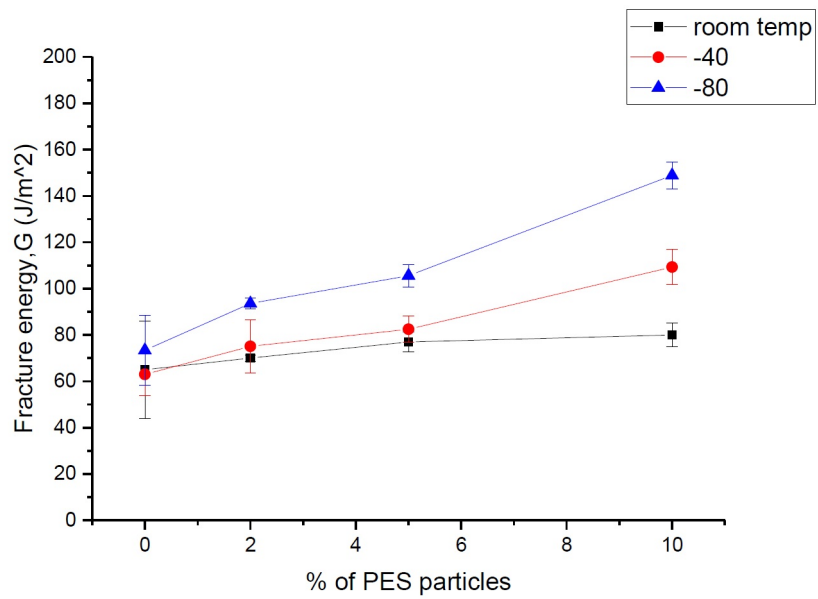


Figure 4.64: Fracture energy of PES modified epoxy under low temperature

Hybrid PES(PES + CSR):

The same trend of increase in fracture energy when temperature reduced and especially when wt% used was high was found in hybrid PES specimens. The fracture energy values were also found to be similar to PES specimens, with small standard deviations (10% or less). Therefore, results were reliable but toughening effect of Hybrid PES is not clear. It is assumed that significantly higher fracture properties would be produced when hybrid particles were used. It could be due to the % of the particles that could undergoes toughening mechanism (debonding, void growth) is limited. With the high concentration of particles added in, small amount of clusters were found. Dissolving the particles increased the viscosity of the mixture, hence, hybrid particles was not well mixed when wt% used was high. This also explain why the hybrid specimens had slightly lower fracture energy values when compare to CSR specimens.

Table 4.27: Fracture energy of Hybrid PES modified epoxy under low temperature

Temperature	Room temperature (20 °C)		-40 °C		-80 °C		
	% of Hybrid particles	G (J/m ²)	SD	G (J/m ²)	SD	G (J/m ²)	SD
0	62.9	11.2		93.5	9.2	126.4	15.1
0.5	61.9	4.4		97.8	14.1	130.5	11.6
1	72.2	44.0		96.7	29.2	134.0	13.4
2	80.0	14.3		104.8	8.2	134.2	19.5
3	89.1	11.0		107.3	4.2	135.7	5.9
5	96.9	18.8		116.9	5.0	138.3	16.2
10	166.4	49.5		168.9	6.4	192.4	17.3

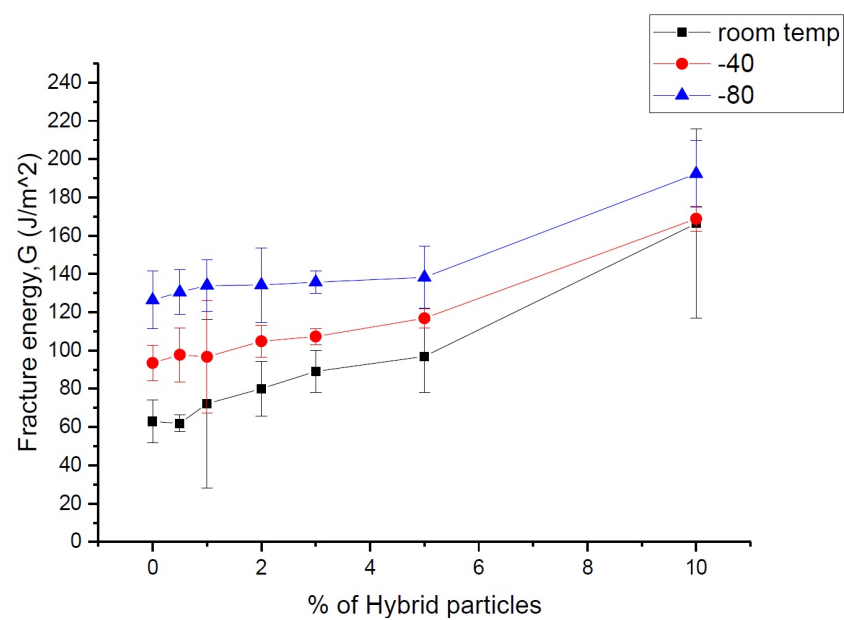


Figure 4.65: Fracture energy of Hybrid PES modified epoxy under low temperature

The increasing trend in W210 was not as clear as PES, curves were not as stable. Specimens tested under low temperature generally produced an increased in fracture energy, but this was not clear in W210 specimens. Highest fracture energy was found at 10wt% tested under room temperature. There were also slightly bigger standard deviations found in these results when compare, but still within an acceptable range.

4.11.2 Fracture energy predictions

Fracture energy predictions of W210 and PES were shown in tables to and figures to below. There was a range of sizes found in PES particles (350-500 micrometer), therefore, an average size was used in the predictions. Average size was also used in Hybrid materials, and predictions were reasonable. Hybrid materials were found to have higher fracture energy predictions similar to modulus predictions, but there were significantly higher values in Hybrid W210 than Silica, and Hybrid PES shown higher predictions than CSR predictions. Synergy effect was found. 100% void growth shown the highest fracture energy values for all % of all particles when compare to 14.3% void growth and shear. Experimental results were found smaller than 14.3% void growth prediction, this suggested that specimens could perform better with improvement in preparation method, but experimental values were reasonable, so it could be a normal variation in results, and that was not at the highest performance range. Shear was found to have the lowest values, as it was assuming shear only, same case was found here for all % in all particles except for high % of hybrid W210 and hybrid PES.

Table 4.28: Table showing fracture energy predictions of W210 and PES from assuming 100% void growth

particles	W210	PES	Hybrid W210	Hybrid PES
% of particles	$Gu + \Delta Gv$ (J/m ²)			
0	68.0	68.0	68.0	68.0
2	91.2	98.2	90.3	72.3
5	256.1	198.2	251.3	169.9
10	443.6	431.1	529.5	491.9

Table 4.29: Table showing fracture energy predictions from assuming 14.3% void growth

particles	W210	PES	Hybrid W210	Hybrid PES
% of particles	$G_u + 0.143\Delta G_v$ (J/m ²)			
0	68	68	68	68
2	82.7	91.2	71.7	69.2
5	140.0	104.3	128.5	104.4
10	381.7	136.6	185.3	192.8

Table 4.30: Table showing fracture energy predictions from assuming there was only shear

particles	W210	PES	Hybrid W210	Hybrid PES
% of particles	G_s (J/m ²)			
0	68	68	68	68
2	76.4	75.0	86.6	71.1
5	160.8	131.7	168.5	129.2
10	241.9	232.2	328.9	265.3

Table and figure shown the fracture energy predictions and experimental fracture energy values. In W210 specimens, the predictions were according to expected, 100% void growth had the highest fracture energy, followed by 14.7% of void and shear only shown the least value. But the experimental results were similar to 14.7% void growth except for 10wt %, this could be due to the saturation of mixture when % was high, 10wt% was found to be the highest % possible % for with W210 particle used.

Table 4.31: Table showing fracture energy predictions of ceramics W210-modified epoxy

particles	W210				
% of particles	14.7% of void (J/m^2)	100% void growth (J/m^2)	G-shear (J/m^2)	Experimental G (J/m^2)	SD
0	68	68.0	68	68.0	21.0
2	82.7	91.2	76.4	82.2	6.0
5	140.0	256.1	160.8	101.2	23.2
10	381.7	443.6	241.9	147.4	24.5

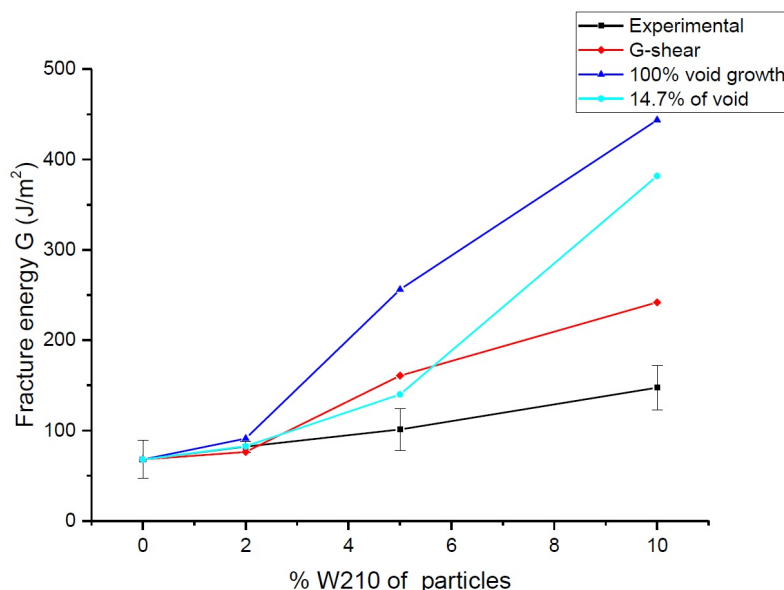


Figure 4.66: Figure showing fracture energy predictions of ceramics W210-modified epoxy

Table and figure shown the fracture energy predictions of hybrid W210 specimens when compare to experimental results. This is shown that the shear values were higher than 14.7% of void growth, they were slightly higher under low % and about 1 time higher for high %. Experimental values were very similar to 14.7% of void growth, same as expected.

Table 4.32: Table showing fracture energy predictions of Hybrid ceramics W210-modified epoxy

particles	Hybrid W210				
% of particles	14.7% of void (J/m^2)	100% void growth (J/m^2)	G-shear (J/m^2)	Experimental G (J/m^2)	SD
0	68	68.0	68	68.0	21.0
2	71.7	90.3	86.6	94.6	9.5
5	128.5	251.3	168.5	111.6	0.9
10	185.3	529.5	328.9	155.4	15.0

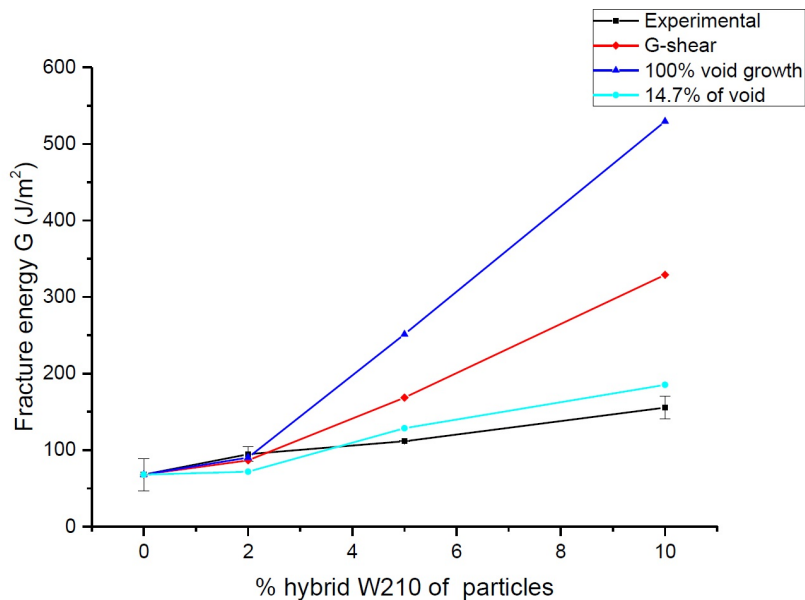


Figure 4.67: Figure showing fracture energy predictions of Hybrid ceramics W210-modified epoxy

Table and figure shown the fracture energy predictions of PES specimens when compare to experimental results. The 14.7% of void growth were also found smaller than shear in PES results as well, with a similar ratio in difference. The experimental results were found slightly smaller than 14.7% of void growth, but their values were similar. 100% void growth shown the highest fracture energy values as expected.

Table 4.33: Table showing fracture energy predictions of PES-modified epoxy

particles	PES				
% of particles	14.7% of void (J/m^2)	100% void growth (J/m^2)	G-shear (J/m^2)	Experimental G (J/m^2)	SD
0	68	68.0	68	65	21.0
2	91.2	98.2	75.0	70	1.3
5	104.3	198.2	131.7	77	4.2
10	136.6	431.1	232.2	80	5.1

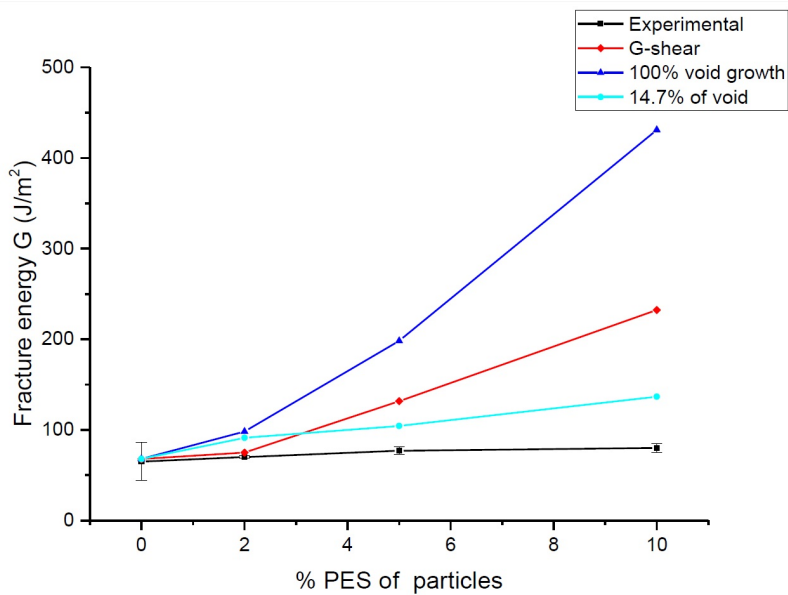


Figure 4.68: Figure showing fracture energy predictions of PES-modified epoxy

Table and figure shown the fracture energy predictions of hybrid PES specimens when compare to experimental results. Experimental data were found smaller than 14.7% of void growth, but they were still similar to 14.7% void growth when compare to other data. 100% void growth shown the highest fracture energy values as expected.

Table 4.34: Table showing fracture energy predictions of Hybrid PES-modified epoxy

particles	Hybrid PES				
% of particles	14.7% of void (J/m^2)	100% void growth (J/m^2)	G-shear (J/m^2)	Experimental G (J/m^2)	SD
0	68	68	68.0	62.9	9.2
2	69.2	71.1	72.3	70.0	11.5
5	104.4	129.2	169.9	77.0	5.7
10	192.8	265.3	491.9	80.0	7.6

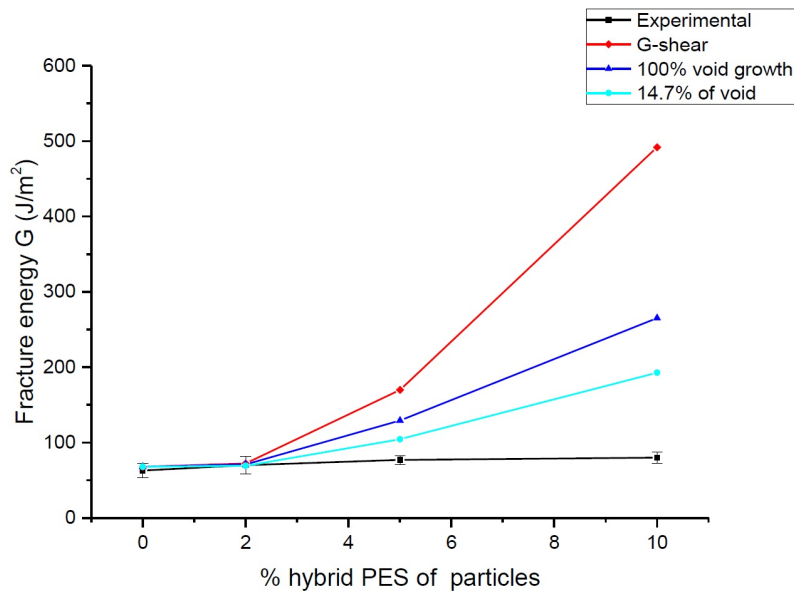


Figure 4.69: Figure showing fracture energy predictions of Hybrid PES-modified epoxy

To conclude, results shown similar behaviour for both W210 and PES materials. Overall results agree with experimental results, the effect of saturation in the mixture was large, this was the reason why experimental results were significantly lower than predictions, therefore, optimum toughening effect lies in medium range of particles used.

4.11.3 Analytical model modulus predictions

The predicted modulus of W210 and PES modified epoxy were shown in figures to and table to below. Overall results were similar for all particles, high % of particles used shown a higher improvement as expected and most of the predictions were similar to experimental results. It is shown that the experimental results from hybrid W210 was

very close to predictions, while experimental results were slightly higher than predictions in W210. There were slightly higher predictions for hybrid W210 specimens, but overall, they were predicted to have similar behaviour. Hybrid W210 contains both W210 and Silica particles, but their predicted modulus were slightly smaller Silica predictions for all %. It is believed that due to small size of Silica particles, toughening were enhanced more than W210 can do, therefore producing higher prediction values.

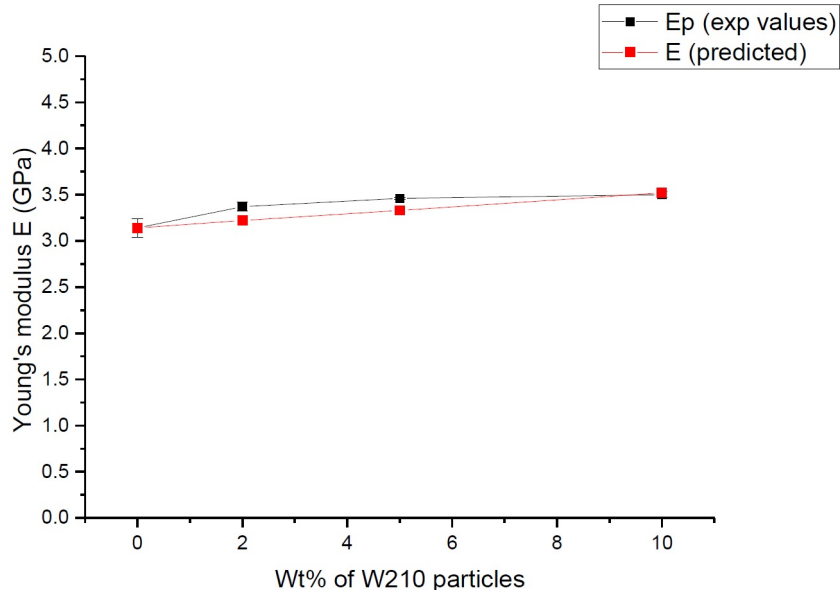


Figure 4.70: Predicted modulus of W210-modified epoxy

Table 4.35: Predicted modulus of W210-modified epoxy

Wt% of W210 particles	Ep (exp values)	E (predicted)
0	3.14	3.14
2	3.37	3.22
5	3.46	3.33
10	3.50	3.52

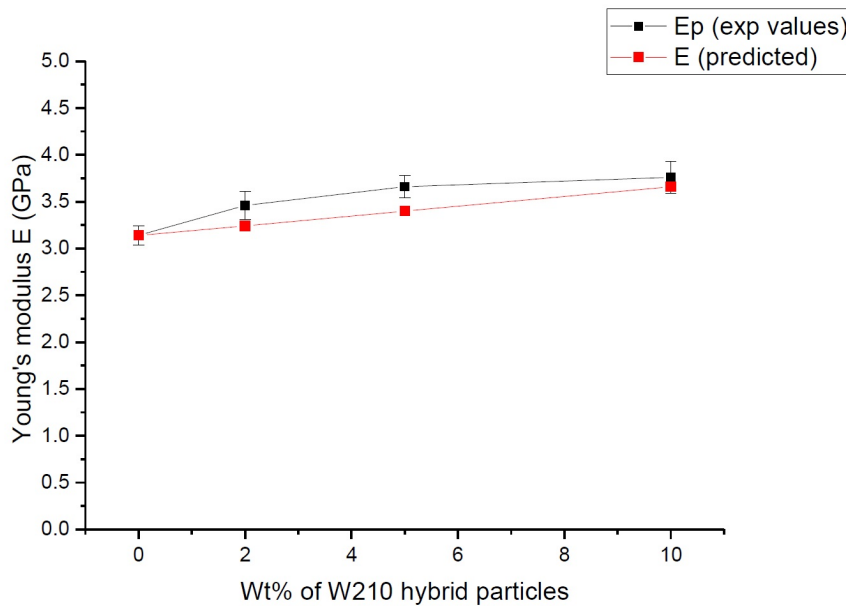


Figure 4.71: Predicted modulus of W210 hybrid-modified epoxy

Table 4.36: Predicted modulus of W210 hybrid-modified epoxy

Wt% of W210 hybrid particles	Ep (exp values)	E (predicted)
0	3.14	3.14
2	3.46	3.24
5	3.66	3.40
10	3.76	3.66

PES results were very similar to W210, similar patterns were found in those results. However, in CSR predictions, 10% of CSR shown the highest prediction of 4.49GPa, higher than any specimens here, therefore it is expected that results would not be as high as CSR, as it is the only case. Predictions were found higher than experimental results for 10% of particles, this could be due to particles were not as even in the mixture as it was saturated.

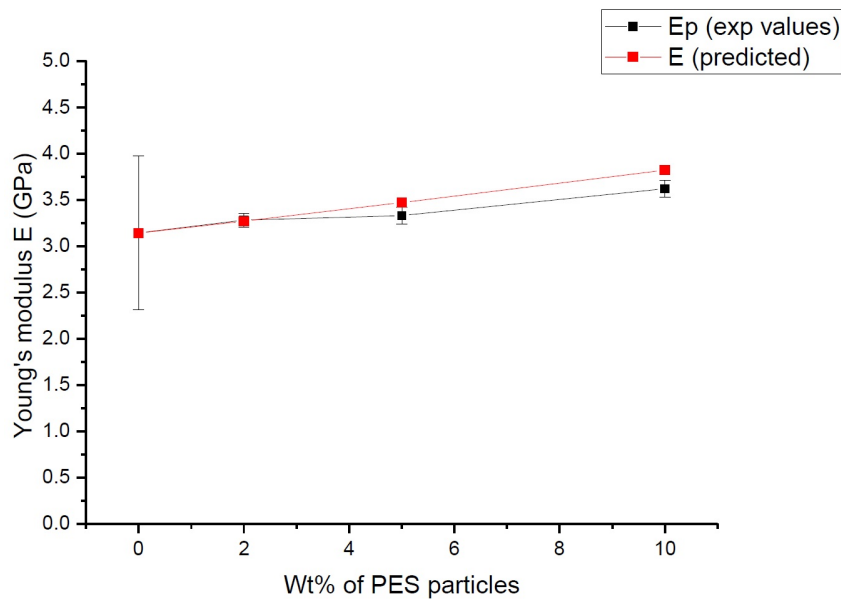


Figure 4.72: Predicted modulus of PES-modified epoxy

Table 4.37: Predicted modulus of PES-modified epoxy

Wt% of PES particles	Ep (exp values)	E (predicted)
0	3.14	3.14
2	3.28	3.27
5	3.33	3.47
10	3.62	3.82

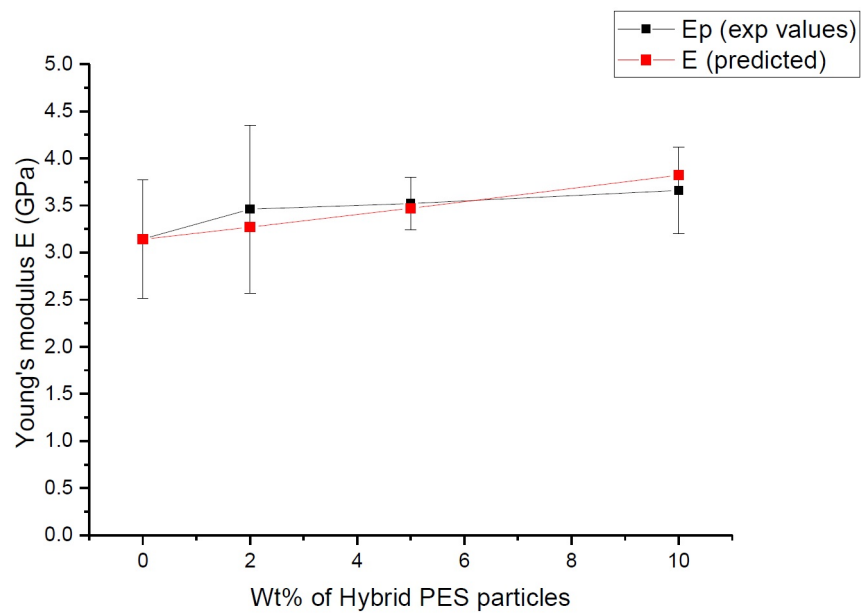


Figure 4.73: Predicted modulus of PES hybrid-modified epoxy

Table 4.38: Predicted modulus of PES hybrid-modified epoxy

Wt% of PES hybrid particles	Ep (lab values)	E (predicted)
0	3.14	3.14
2	3.46	3.28
5	3.52	3.51
10	3.66	3.90

4.12 Conclusions

This work aimed to provide insight to the fracture mechanics profile of modified epoxies using the established fracture mechanics approach. The first stage of the work has been comparing the different weight % of silica, CSR and hybrid particles added into epoxy, studying their surface characteristics by imaging using field emission gun scanning electron microscopy, and compare their mechanical properties with modelling predictions using software Abaqus. The next step of the project is to investigate the effect of test rate to the fracture behaviour, it is expected that high rate would enhance brittle failure, and toughening mechanism would be reduced, due to the lower energy dissipation at crack tip. High rate analysis can be challenging, therefore, trials of different setting conditions would be needed. There have been a few trials ongoing and more progress on high rate testing would be coming up in a short period of time.

This is a reference example [?].

References

1. Mohammed, R.D., et al., Toughening mechanisms of nanoparticle-modified epoxy polymers. Nsti Nanotech 2008, Vol 1, Technical Proceedings, ed. M. Laudon and B. Romanowicz. 2008, Boca Raton: CRC Press-Taylor & Francis Group. p.798-801.
2. Hsieh, T.H., et al., The mechanisms and mechanics of the toughening of epoxy polymers modified with silica nanoparticles. Polymer, 2010. 51(26): p. 6284-6294.
3. Hsieh, T.H., et al., The toughness of epoxy polymers and fibre composites modified with rubber microparticles and silica nanoparticles. Journal of Materials Science, 2010. 45(5): p. 1193-1210.
4. Mohammed, R.D., et al., Toughening mechanisms of nanoparticle-modified epoxy polymers. Nsti Nanotech 2008, Vol 1, Technical Proceedings, ed. M. Laudon and B.

- Romanowicz. 2008, Boca Raton: Crc Press-Taylor & Francis Group. 798-801.
5. Kinloch, A.J., Adhesives in engineering. Proceedings of the Institution of Mechanical Engineers Part G-Journal of Aerospace Engineering, 1997. 211(G5): p. 307-335.
 6. Dittanet, P. and R.A. Pearson, Effect of silica nanoparticle size on toughening mechanisms of filled epoxy. Polymer, 2012. 53(9): p. 1890-1905.
 7. Imanaka, M., et al., Fracture toughness of spherical silica-filled epoxy adhesives. International Journal of Adhesion and Adhesives, 2001. 21(5): p. 389-396.
 8. Huang, Y. and A.J. Kinloch, Modelling of the toughening mechanisms in rubber-modified epoxy polymers - Part I Finite element analysis studies. Journal of Materials Science, 1992. 27(10): p. 2753-2762.
 9. Kinloch, A.J., et al., Deformation and fracture behaviour of a rubber-toughened epoxy: 1. Microstructure and fracture studies. Polymer, 1983. 24(10): p. 1341-1354.
 10. Giannakopoulos, G., K. Masania, and A.C. Taylor, Toughening of epoxy using core-shell particles. Journal of Materials Science, 2011. 46(2): p. 327-338.
 11. Bagheri, R., B.T. Marouf, and R.A. Pearson, Rubber-Toughened Epoxies: A Critical Review. Polymer Reviews, 2009. 49(3): p. 201-225.
 12. Chen, J. and A.C. Taylor, Epoxy modified with triblock copolymers: morphology, mechanical properties and fracture mechanisms. Journal of Materials Science, 2012. 47(11): p. 4546-4560.
 13. Garg, A.C. and Y.-W. Mai, Failure mechanisms in toughened epoxy resinsA review. Composites Science and Technology, 1988. 31(3): p. 179-223.
 14. Garg, A.C., Failure Prediction in Toughened Epoxy Resins. Composites Science and Technology (1988) 225-242. 31.
 15. Pan, J. and S.-H. Lin, 6 - Fracture Mechanics and Fatigue Crack Propagation, in Fatigue Testing and Analysis, Y.-L. Lee, et al., Editors. 2005, Butterworth-Heinemann: Burlington. p. 237-284.
 16. Lee, J.H., PhD thesis, The fracture behaviour of nano-particle toughened epoxy adhesives, in Mechanical Engineering Department. 2006, Imperial College London.
 17. Bandyopadhyay, S., Review of the microscopic and macroscopic aspects of fracture of unmodified and modified epoxy-resins. Materials Science and Engineering A-Structural Materials Properties Microstructure and Processing, 1990. 125(2): p. 157-184.
 18. Wise, C.W., W.D. Cook, and A.A. Goodwin, CTBN rubber phase precipitation in model epoxy resins. Polymer, 2000. 41(12): p. 4625-4633.
 19. Tadaharu Adachi, et al., Fracture toughness of nano- and micro-spherical silica-particle-filled epoxy composites. Acta Materialia, 2008. 56(9): p. 2101-2109.
 20. Dittanet, P. and R.A. Pearson, Effect of bimodal particle size distributions on the

- toughening mechanisms in silica nanoparticle filled epoxy resin. *Polymer*, 2013. 54(7): p. 1832-1845.
21. Johnsen, B.B., A.J. Kinloch, and A.C. Taylor, Toughness of syndiotactic polystyrene/epoxy polymer blends: microstructure and toughening mechanisms. *Polymer*, 2005. 46(18): p. 7352-7369.
22. Manjunatha, C.M., et al., The Fatigue and Fracture Behavior of Micron-Rubber and Nano-Silica Particles Modified Epoxy Polymer. *International Journal of Nanoscience*, 2012. 11(03): p. 1240002.
23. Liu, H.-Y., et al., On fracture toughness of nano-particle modified epoxy. *Composites Part B: Engineering*, 2011. 42(8): p. 21702175.
24. Hsieh, T.H., et al., The toughness of epoxy polymers and fibre composites modified with rubber microparticles and silica nanoparticles. *Journal of Materials Science*, 2010. 45(5): p. 1193-1210.
25. Chen, J., et al., The mechanical properties and toughening mechanisms of an epoxy polymer modified with polysiloxane-based core-shell particles. *Polymer*, 2013. 54(16): p. 4276-4289.
26. Chen, J., PhD thesis, Toughening Epoxy Polymers and Carbon Fibre Composites with Core-Shell Particles, Block Copolymers and Silica Nanoparticles, in Mechanical Engineering Department. 2013, Imperial College London.
27. Mohammed, R.D., PhD thesis, Material properties and fracture mechanisms of epoxy nano-composites, in Mechanical Engineering department. 2007, Imperial College London.
28. D5023, A., Standard Test Method for Plastics: Dynamic Mechanical Properties: In Flexure (Three-Point Bending). 2007, ASTM.
29. Hsieh, T.-H., PhD thesis, Properties and toughening of Silica nanoparticle-and Carbon Nanotube-modified epoxy polymers, in Mechanical Engineering Department. 2011, Imperial College London: Imperial College London.
30. Kinloch, A.J., M.L. Yuen, and S.D. Jenkins, Thermoplastic-toughened epoxy polymers. *Journal of Materials Science*, 1994. 29(14): p. 3781-3790.
31. Kinloch, A.J., S.J. Shaw, and D.L. Hunston, Deformation and fracture behaviour of a rubber-toughened epoxy: 2. Failure criteria. *Polymer*, 1983. 24(10): p. 1355-1363.
32. Kinloch, A.J., Adhesion and Adhesives Science and Technology. 1990, London: Chapman and Hall.
33. Blackman, B.R.K. and A.J. Kinloch, Protocol for the determination of the mode I adhesive fracture energy, GIC, of structural adhesives using the double cantilever beam (DCB) and tapered double cantilever beam. ESIS, 2008.

34. BS7991, Determination of the mode I adhesive fracture energy, GIC, of structural adhesives using the double cantilever beam (DCB) and tapered double cantilever beam (TDCB) specimens. BS 7991:2001, BSI.
35. Blackman, B.R.K., et al., Measuring the mode I adhesive fracture energy, GIC, of structural adhesive joints: the results of an international round-robin. International Journal of Adhesion and Adhesives, 2003. 23(4): p. 293-305.
36. Adnan, A. and C.T. Sun, Effect of adhesive thickness on joint strength: A molecular dynamics perspective. Journal of Adhesion, 2008. 84(5): p. 401-420.
37. Matinlinna, J., Biomaterials I Lecture 3. 2012, The University of Hong Kong.
38. Karac, A., et al., Modelling the fracture behaviour of adhesively-bonded joints as a function of test rate. Engineering Fracture Mechanics, 2011. 78(6): p. 973-989.
39. ISO13586, Plastics. Determination of fracture toughness (GIC and KIC). Linear elastic fracture mechanics (LEFM) approach. 15 June 2000, BSI.
40. Babu, J.B., PhD thesis, Predicting the fatigue behaviour of matrices and fibre-composites based upon modified epoxy polymers, in Mechanical Engineering Department. 2012, Imperial College London.
41. Kinloch, A.J., D. Maxwell, and R.J. Young, Micromechanisms of crack-propagation in hybrid-particulate composites. Journal of Materials Science Letters, 1985. 4(10): p. 1276-1279.
42. Moloney, A.C., et al., Parameters determining the strength and toughness of particulate filled epoxide resins. Journal of Materials Science, 1987. 22(2): p. 381-393.
43. Bucknall, C.B., Quantitative approaches to particle cavitation, shear yielding, and crazing in rubber-toughened polymers. Journal of Polymer Science Part B-Polymer Physics, 2007. 45(12): p. 1399-1409.
44. Huang, Y. and A.J. Kinloch, The sequence of initiation of the toughening micromechanisms in rubber-modified epoxy polymers. Polymer, 1992. 33(24): p. 5338-5340.
45. Guild, F.J., A.J. Kinloch, and A.C. Taylor, Particle cavitation in rubber toughened epoxies: the role of particle size. Journal of Materials Science, 2010. 45(14): p. 3882-3894.
46. Kawaguchi, T. and R.A. Pearson, The effect of particle-matrix adhesion on the mechanical behavior of glass filled epoxies. Part 2. A study on fracture toughness. Polymer, 2003. 44(15): p. 4239-4247.
47. Kunz-Douglass, S., P.W.R. Beaumont, and M.F. Ashby, A model for the toughness of epoxy-rubber particulate composites. Journal of Materials Science, 1980. 15(5): p. 1109-1123.

48. Huang, Y. and A.J. Kinloch, The role of plastic void growth in the fracture of rubber-toughened epoxy polymers. *Journal of Materials Science Letters*, 1992. 11(8): p. 484-487.
49. Bagheri, R. and R.A. Pearson, Role of particle cavitation in rubber-toughened epoxies: II. Inter-particle distance. *Polymer*, 2000. 41(1): p. 269-276.
50. Huang, Y. and A.J. Kinloch, Modelling of the toughening mechanisms in rubber-modified epoxy polymers - Part II A quantitative description of the microstructure-fracture property relationships. *Journal of Materials Science*, 1992. 27(10): p. 2763-2769.
51. Blackman, B.R.K., et al., The fracture behaviour of structural adhesives under high rates of testing. *Engineering Fracture Mechanics*, 2009. 76(18): p. 2868-2889.
52. Blackman, B.R.K., et al., The fracture behaviour of adhesively-bonded composite joints: Effects of rate of test and mode of loading. *International Journal of Solids and Structures*, 2012. 49(13): p. 1434-1452.
53. Rodriguez Sanchez, F.S., PhD thesis, Fracture Behaviour of Automotive Adhesive Joints, in Mechanical Engineering Department. 2008, Imperial College London.
54. Blackman, B.R.K., et al., The failure of fibre composites and adhesively bonded fibre composites under high rates of test .2. Mode I loading - Dynamic effects. *Journal of Materials Science*, 1996. 31(17): p. 4451-4466.
55. Blackman, B.R.K., et al., The failure of fibre composites and adhesively bonded fibre composites under high rates of test .1. Mode I loading - Experimental studies. *Journal of Materials Science*, 1995. 30(23): p. 5885-5900.
56. Blackman, B.R.K., et al., The failure of fibre composites and adhesively bonded fibre composites under high rates of test .3. Mixed-mode I/II and mode II loadings. *Journal of Materials Science*, 1996. 31(17): p. 4467-4477.
57. Blackman B. R. K., et al., The fracture behaviour of structural adhesives under high rates of testing. *Engineering Fracture Mechanics*, 2009. 76(18): p. 2868-2889.
58. Feito, D.A., PhD thesis, Fracture mechanics of carbon fibre reinforced plastic to Ti-alloy adhesive joints, in Mechanical Engineering Department 2012, Imperial College London.
59. Masania, K., Taylor, A.C., Kinloch, A.J. and Sprenger, S. , The fracture of nanosilica and rubber toughened epoxy fibre composites, in Proceedings of American Composites Manufacturing Association (ACMA) Composites and POLYCON 09. Tampa, USA. 2009, ACMA, Arlington, USA.
60. Blackman, B.R.K., et al., The calculation of adhesive fracture energies in mode I: revisiting the tapered double cantilever beam (TDCB) test. *Engineering Fracture*

- Mechanics, 2003. 70(2): p. 233-248.
61. Blackman, B.R.K., Personal Communication. 2015.
 62. ISO, B.E., BS EN ISO 527-1:2012, Plastics. Determination of tensile properties. General principles.
 63. 17281:2002, I., Plastics. Determination of fracture toughness (GIC and KIC) at moderately high loading rates (1 m/s). 2002, BSI.
 64. Giannakopoulos, G., K. Masania, and A.C. Taylor, Toughening of epoxy using core-shell particles. *Journal of Materials Science*, 2011. 46(2): p. 327-338.
 65. Masania, K., PhD thesis, Toughening mechanisms of silica nanoparticle-modified epoxy polymers, in Mechanical Engineering Department. 2010, Imperial College London.
 66. Chong, H.M., PhD thesis, Toughening mechanisms of block copolymer and graphene nanoplatelet modified epoxy polymers, in Mechanical Engineering Department. 2015, Imperial College London.
 67. Bray, D.J., et al., The modelling of the toughening of epoxy polymers via silica nanoparticles: The effects of volume fraction and particle size. *Polymer*, 2013. 54(26): p. 7022-7032.
 68. Taylor, A.C., Personal Communication. 2016.
 69. Brett, M., PhD thesis, Prediction of the performance of adhesively-bonded composite joints, in Mechanical Engineering Department. 2011, Imperial College London.
 70. Meschut, G., Estimation of the temperature influence on adhesively bonded joints with time-temperature-superposition. Laboratory of Material Science and Joining Technology: Paderborn, Airbus Operations GmbH, Bremen, 2013.
 71. Huang, Y. and A.J. Kinloch, The Use of Time-Temperature Superpositioning in Studying the Fracture Properties of Rubber-Toughened Epoxy Polymers. *The Journal of Adhesion*, 1993. 41(1-4): p. 5-22.

Appendix A

Appendices

A.1 Input file-TDCB model

```
*Heading  
** Job name: BC=30 Model name: CopyOfload=600X  
** Generated by: Abaqus/CAE 6.13-2  
*Preprint, echo=NO, model=NO, history=NO, contact=NO  
**  
** PARTS  
**  
*Part, name=BOTTOMPART  
*Node  
1, 10.019454, 0.  
2, 10., -0.400000006  
...  
4274, 4275, 4276, 4277, 4278, 4279, 4280, 4281, 4282, 4283  
*Nset, nset=BOTTOMLOAD  
23,  
** Section: Section-2-ADHESIVE1  
*Solid Section, elset=ADHESIVE1, material=ADHESIVE(STANDARD)  
,  
** Section: Section-3-ADHESIVE3  
*Solid Section, elset=ADHESIVE3, material=ADHESIVE(STANDARD)  
,  
** Section: Section-4-BOTTOMBEAM  
*Solid Section, elset=BOTTOMBEAM, material=ALUMINIUM  
,  
** Section: Section-5-ADHESIVE2  
*Solid Section, elset=ADHESIVE2, material=ADHESIVE(STANDARD)  
,  
*End Part  
**  
*Part, name=COHESIVE-MESH-1  
*Node
```

1, -310., 0.

*Nset, nset=ADHESIVE1

1, 2, 3, 4, 33, 34, 35, 36, 37, 38, 39, 40, 41, 42, 43, 44
45, 46, 1017, 1018, 1019, 1020, 1021, 1022, 1023, 1024, 1025, 1026, 1027, 1028

*Elset, elset=ADHESIVE1

1, 2, 3, 4, 5, 6, 7, 4324, 4325, 4326, 4327, 4328, 4329, 4330

*Elset, elset=ADHESIVE2, generate

4284, 4323, 1

*Nset, nset=ADHESIVE3

...

*Nset, nset=TOPPARTTIE

5, 8, 10, 11, 13, 117, 118, 119, 120, 121, 122, 123, 124, 125, 126, 127

...

6449, 6450, 6451, 6452

*Nset, nset=TOPLOAD

22,

** Section: Section-6-ADHESIVE1

*Solid Section, elset=ADHESIVE1, material=ADHESIVE(STANDARD)

,

** Section: Section-7-ADHESIVE3

*Solid Section, elset=ADHESIVE3, material=ADHESIVE(STANDARD)

,

** Section: Section-8-TOPBEAM

*Solid Section, elset=TOPBEAM, material=ALUMINIUM

,

** Section: Section-9-ADHESIVE2

*Solid Section, elset=ADHESIVE2, material=ADHESIVE(STANDARD)

,

*End Part

**

```
**  
** ASSEMBLY  
**  
*Assembly, name=Assembly  
**  
*Instance, name=COHESIVE-MESH-1-1, part=COHESIVE-MESH-1  
370., 0., 0.  
*End Instance  
**  
*Instance, name=BOTTOMPART-1, part=BOTTOMPART  
*End Instance  
**  
*Instance, name=TOPPART-1, part=TOPPART  
*End Instance  
**  
*Nset, nset=Set-3, instance=TOPPART-1  
21, 22, 25, 26, 28, 29, 31, 32, 696, 697, 698, 699, 700, 701, 722, 723  
724, 725, 737, 738, 739, 740, 741, 742, 752, 753, 754, 755, 770, 771, 772, 773  
774, 775, 776, 777, 778, 784, 785, 786, 787, 788, 789, 804, 805, 806, 807, 808  
809, 810, 811, 812, 1029, 1030, 1031, 1032, 1033, 1034  
*Nset, nset=Set-4, instance=BOTTOMPART-1  
20, 23, 24, 27, 28, 31, 32, 33, 770, 771, 772, 773, 774, 775, 776, 777  
778, 779, 794, 795, 796, 797, 798, 799, 806, 807, 808, 809, 824, 825, 826, 827  
828, 829, 830, 831, 832, 842, 843, 844, 845, 846, 847, 864, 865, 866, 867, 868  
869, 870, 871, 872, 1029, 1030, 1031, 1032, 1033, 1034  
*Nset, nset=BOTTOMPART-1_BOTTOMPARTTIE_CNS_, internal, instance=BOTTOMPART-1  
5, 8, 10, 11, 13, 97, 98, 99, 100, 101, 102, 103, 104, 105, 106, 107  
...  
934, 935, 936, 937, 938, 939, 940, 941, 942, 943, 944  
*Nset, nset=TOPPART-1_TOPPARTTIE_CNS_, internal, instance=TOPPART-1  
5, 8, 10, 11, 13, 117, 118, 119, 120, 121, 122, 123, 124, 125, 126, 127
```

...

849, 850, 851, 852, 853, 854, 855, 856, 857, 858, 859, 860, 861, 862, 863, 864

865, 866, 867, 868, 869, 870, 871, 872, 873, 874, 875

*Surface, type=NODE, name=BOTTOMPART-1_BOTTOMPARTTIE_CNS__CNS_, internal
BOTTOMPART-1_BOTTOMPARTTIE_CNS_, 1.

*Surface, type=NODE, name=TOPPART-1_TOPPARTTIE_CNS__CNS_, internal
TOPPART-1_TOPPARTTIE_CNS_, 1.

** Constraint: BOTTOMCOHESIVE-1

*Tie, name=BOTTOMCOHESIVE-1, adjust=yes

COHESIVE-MESH-1-1.Surf-2, BOTTOMPART-1_BOTTOMPARTTIE_CNS__CNS_

** Constraint: TOPCOHESIVE-1

*Tie, name=TOPCOHESIVE-1, adjust=yes

COHESIVE-MESH-1-1.Surf-1, TOPPART-1_TOPPARTTIE_CNS__CNS_

*End Assembly

**

** ELEMENT CONTROLS

**

*Section Controls, name=EC-1, ELEMENT DELETION=YES

1., 1., 1.

*Amplitude, name=Amp-1

0., 0., 1., 1.

**

** MATERIALS

**

*Material, name=ADHESIVE(STANDARD)

*Elastic

2900., 0.35

*Material, name=ALUMINIUM

*Elastic

70000., 0.3

```
*Material, name=COHESIVE
*Damage Initiation, criterion=QUADS
60.,60.,60.
*Damage Evolution, type=ENERGY
20.,
*Elastic, type=TRACTION
1e+06, 1e+06, 1e+06
** -----
**
** STEP: Step-1
**
*Step, name=Step-1, nlgeom=YES, inc=1000000
*Static, stabilize=0.0002, allsdtol=0.05, continue=NO
0.0001, 1., 1e-08, 0.01
**
** BOUNDARY CONDITIONS
**
** Name: BC-1 Type: Displacement/Rotation
*Boundary, amplitude=Amp-1
Set-3, 1, 1
Set-3, 2, 2, 25.
Set-3, 6, 6
** Name: BC-2 Type: Displacement/Rotation
*Boundary, amplitude=Amp-1
Set-4, 1, 1
Set-4, 2, 2, -25.
Set-4, 6, 6
**
** OUTPUT REQUESTS
**
*Restart, write, frequency=0
```

```
**  
** FIELD OUTPUT: F-Output-1  
**  
*Output, field  
*Node Output  
CF, RF, U  
*Element Output, directions=YES  
LE, PE, PEEQ, PEMAG, S, STATUS  
*Contact Output  
CDISP, CSTRESS  
**  
** HISTORY OUTPUT: H-Output-3  
**  
*Output, history  
*Node Output, nset=Set-4  
RF1, RF2, RF3, RM1, RM2, RM3  
**  
** HISTORY OUTPUT: H-Output-1  
**  
*Output, history, frequency=1000  
*Node Output, nset=BOTTOMPART-1.BOTTOMLOAD  
RF1, RF2, RF3, RM1, RM2, RM3, U1, U2  
U3, UR1, UR2, UR3  
**  
** HISTORY OUTPUT: H-Output-2  
**  
*Node Output, nset=TOPPART-1.TOPLOAD  
RF1, RF2, RF3, RM1, RM2, RM3, U1, U2  
U3, UR1, UR2, UR3  
*End Step
```